

VORTEX-INDUCED TRANSVERSE LOADING ON AN ARTICULATED  
TOWER

By

AHMED FAHMY OMAR

A DISSERTATION PRESENTED TO THE GRADUATE SCHOOL  
OF THE UNIVERSITY OF FLORIDA IN  
PARTIAL FULFILLMENT OF THE REQUIREMENTS  
FOR THE DEGREE OF DOCTOR OF PHILOSOPHY

UNIVERSITY OF FLORIDA

1992

To my parents

## ACKNOWLEDGEMENTS

The author wishes to express his sincere appreciation and gratitude to the supervisory committee chairman, Prof. D. Max Sheppard, for his continuous support, guidance and friendship in and out of the academic framework. It was a real joy working under his patient leadership. His input and encouragement in this long endeavor proved invaluable.

A special debt of gratitude is owed to Profs. Marc I. Hoit, Hsiang Wang and David C. Zimmerman for serving as members of his Ph.D. supervisory committee. In particular Prof. David C. Zimmerman was most helpful during the early stages of this work. Appreciation is also extended to Prof. Robert G. Dean for many helpful discussions during the course of this study.

Many thanks go to Sidney Schofield, Subarana Malakar, Vernon Sparkman, Chuck Broward and the other members of the Coastal and Oceanographic Engineering Department and Laboratory for their help, friendship and cooperation. The author would also like to take this opportunity to express gratitude to all his past teachers who contributed in one way or another to his achievement of this educational goal.

This work could not have been accomplished without the support of the University of Florida and the US Army Corps of Engineers Coastal Engineering Research Center. The contribution of the water tank and other facilities by the Crom Corporation is gratefully acknowledged.

Finally, the author is very grateful to his parents and brothers, for their patience, love and sacrifice during the course of his life.

## TABLE OF CONTENTS

ACKNOWLEDGEMENTS . . . . .	iii
LIST OF FIGURES . . . . .	vi
LIST OF TABLES . . . . .	xi
LIST OF SYMBOLS . . . . .	xii
ABSTRACT . . . . .	xvii
CHAPTERS	
1 INTRODUCTION . . . . .	1
1.1 Problem Statement . . . . .	1
1.2 Research Objectives . . . . .	3
2 LITERATURE REVIEW . . . . .	5
2.1 Overview . . . . .	5
2.2 Steady, Planar Flow . . . . .	10
2.2.1 Transversely Constrained Cylinder in Steady, Planar Flow . .	10
2.2.2 Transversely Unconstrained Cylinder in Steady, Planar Flow .	15
2.3 Oscillatory, Planar Flow . . . . .	17
2.3.1 Transversely Constrained Cylinder in Oscillatory, Planar Flow	17
2.3.2 Transversely Unconstrained Cylinder in Oscillatory, Planar Flow	22
2.4 Oscillatory, Nonplanar Flow . . . . .	24
2.5 Wave Flows . . . . .	26
3 EXPERIMENTAL INVESTIGATIONS . . . . .	31
3.1 Scaling Parameters and Model Selection . . . . .	31
3.2 Experimental Set-up . . . . .	34
3.3 Instrumentation and Calibration . . . . .	37
3.3.1 Frequency Generator . . . . .	37
3.3.2 Force Transducers . . . . .	41
3.3.3 Linear Displacement Transducers . . . . .	42
3.3.4 Thermistors . . . . .	42
3.3.5 Lowpass Filters . . . . .	43
3.4 Data Reduction . . . . .	44

4	MATHEMATICAL MODELS . . . . .	47
4.1	In-line Force . . . . .	47
4.2	Transverse Force . . . . .	54
4.2.1	Steady Flow Model . . . . .	55
4.2.2	Quasi-Steady Model . . . . .	56
4.2.3	Series Model . . . . .	57
4.2.4	Proposed Model . . . . .	58
4.2.5	Fixed Tower . . . . .	59
4.2.6	Complaint Tower . . . . .	60
5	EXPERIMENTAL DATA ANALYSIS . . . . .	63
5.1	In-line Forces . . . . .	63
5.2	Transverse Forces . . . . .	69
5.2.1	Constrained Transverse Motion . . . . .	69
5.2.2	Unconstrained Transverse Motion . . . . .	89
5.3	Sources of Uncertainty and Inaccuracy . . . . .	116
6	SUMMARY AND CONCLUSIONS . . . . .	118
6.1	Summary of the Results . . . . .	118
6.2	Conclusions . . . . .	120
6.3	Recommendations for Further Work . . . . .	123
APPENDICES		
A	ANALYSIS TECHNIQUES . . . . .	125
B	INSTRUMENTATIONS AND CALIBRATION DATA . . . . .	129
C	FLOW CHARTS OF THE VARIOUS COMPUTER PROGRAMS . . . . .	142
	BIOGRAPHICAL SKETCH . . . . .	154

## LIST OF FIGURES

2.1	Flow chart for cylinder-loading response. . . . .	7
2.2	Lift coefficient versus Reynolds number for steady, planar flow around a smooth, fixed cylinder. . . . .	12
2.3	Regimes of steady, planar flow across a smooth, fixed circular cylinder, (Ref. 14). . . . .	13
2.4	Strouhal-Reynolds numbers relationship with transverse force spectra for steady, planar flows around a smooth, fixed cylinder (Refs. 14, 67). . . . .	14
2.5	Span-wise coherence length versus Reynolds number for steady, planar flow around a smooth, fixed cylinder (Ref. 68). . . . .	15
2.6	Schematic transverse force and corresponding response power spectra for steady, planar flow around a smooth, transversely unconstrained cylinder (Ref. 74). . . . .	16
2.7	Lift coefficient versus Keulegan-Carpenter number for oscillatory, planar flow around a smooth, transversely constrained cylinder (for constant Reynolds number, $Re$ ). . . . .	18
2.8	Lift coefficient versus Keulegan-Carpenter number for oscillatory, planar flow around a smooth, transversely constrained cylinder (for constant frequency parameter, $\beta$ ). . . . .	19
2.9	Schematic transverse force power spectra for oscillatory, planar flow around a smooth, transversely constrained cylinder for various Keulegan-Carpenter number, $KC$ (Refs. 2, 32, 47). . . . .	21
2.10	Span-wise coherence length for transversely constrained cylinder in oscillatory, planar flow (Ref. 50). . . . .	21
2.11	Schematic transverse force and corresponding response power spectra for oscillatory, planar flow around a smooth, transversely unconstrained cylinder for various reduced velocities, $V_r$ (Ref. 47). . . . .	23
2.12	Span-wise coherence length for transversely unconstrained cylinder near a wall in oscillatory, planar flow (Ref. 39). . . . .	24

2.13	Lift coefficient harmonics versus Keulegan-Carpenter number, $KC$ , — curve fit of data from harmonically oscillated articulated cylinder in still water, • data from waves impinging on a smooth, fixed vertical cylinder (Refs. 12, 13). . . . .	26
2.14	Lift coefficient versus Keulegan-Carpenter number for regular waves around a smooth, fixed vertical cylinder. . . . .	28
2.15	Schematic transverse force power spectra for regular waves around a smooth, fixed vertical cylinder for various Keulegan-Carpenter numbers, $KC$ (Refs. 12, 73). . . . .	30
2.16	Maximum transverse response for various flow configurations ( $\square$ steady, planar flow), ( $\circ$ oscillatory, planar flow), ( $\bullet$ wave flows). . . .	30
3.1	Schematic diagram of transversely constrained experiment set-up. . . . .	38
3.2	Schematic diagram of transversely unconstrained experiment set-up. . . . .	39
3.3	Photographs of experimental set-up. . . . .	40
3.4	Block diagram of measurement system. . . . .	41
4.1	Definition sketch for the articulated tower showing in-line motion. . . . .	48
4.2	Contour lines defining Error surfaces for the in-line force (Ref. 15). . . . .	51
4.3	Definition sketch showing tower elements and idealized flow. . . . .	58
4.4	Definition sketch for the articulated tower showing transverse motion. . . . .	62
5.1	$C_m$ versus $R_e$ for harmonically oscillated articulated tower (transversely unconstrained). . . . .	64
5.2	$C_D$ versus $R_e$ for harmonically oscillated articulated tower (transversely unconstrained). . . . .	65
5.3	Contour lines defining error surfaces of the in-line force ( $KC = 8.4$ and $R_e = 8.4 \times 10^4$ ). . . . .	66
5.4	Phase comparison between measured and predicted in-line forces (a) $KC = 6.6$ and $R_e = 9.4 \times 10^4$ (b) $KC = 8.4$ and $R_e = 8.4 \times 10^4$ (— measured, .... predicted). . . . .	67
5.5	Comparison of $C_m$ for different flow types. . . . .	68
5.6	Comparison of $C_D$ for different flow types. . . . .	68
5.7	Lift coefficient harmonics for harmonically oscillated articulated tower (transversely constrained), $C_{L(1)}$ to $C_{L(4)}$ . . . . .	71

5.8	Lift coefficient harmonics for harmonically oscillated articulated tower (transversely constrained), $C_{L(5)}$ to $C_{L(8)}$ . . . . .	72
5.9	Lift coefficient harmonics versus beta, $C_{L(1)}$ and $C_{L(2)}$ . . . . .	73
5.10	Lift coefficient harmonics versus beta, $C_{L(3)}$ and $C_{L(4)}$ . . . . .	74
5.11	Phase angle associated with the lift coefficients harmonics, $\phi_{(1)}$ to $\phi_{(4)}$ . . . . .	75
5.12	Phase angle associated with the lift coefficients harmonics, $\phi_{(5)}$ to $\phi_{(8)}$ . . . . .	76
5.13	Comparison between measured and predicted transverse forces ( $R_e = 10^4$ and $KC = 5.45$ ). . . . .	77
5.14	Comparison between measured and predicted transverse forces ( $R_e = 2 \times 10^4$ and $KC = 5.9$ ). . . . .	78
5.15	RMS lift coefficient versus KC. . . . .	79
5.16	Comparison of $C_{Lrms}$ data with those from waves. . . . .	80
5.17	Range of data from wave forces hydrodynamic experiments (Ref. 27). . . . .	81
5.18	Transverse force power spectra for constant $R_e$ ( $R_e = 1.15 \times 10^4$ ). . . . .	83
5.19	Transverse force power spectra for constant $\beta$ ( $\beta = 2, 800$ ). . . . .	83
5.20	Thermistor power spectra for $\beta = 1, 834$ . . . . .	84
5.21	Thermistor power spectra for $\beta = 2, 161$ . . . . .	84
5.22	Schematic illustration of thermistors locations. . . . .	85
5.23	Schematic illustration of the visualization of the vortex-shedding process. . . . .	86
5.24	Definition sketch of span-wise coherence length. . . . .	87
5.25	Span-wise coherence length for transversely constrained articulated tower. . . . .	88
5.26	Span-wise coherence length for transversely constrained articulated tower. . . . .	88
5.27	Comparison between measured and predicted transverse responses (a) $R_e = 2.7 \times 10^4$ and $KC = 5.0$ (b) $R_e = 5.8 \times 10^4$ and $KC = 5.9$ (— measured, .... predicted). . . . .	92



5.28	Comparison of measured and predicted transverse responses ( $R_e = 8.3 \times 10^4$ and $KC = 6.7$ ). . . . .	93
5.29	Comparison of measured and predicted spectra of transverse responses ( $R_e = 8.3 \times 10^4$ and $KC = 6.7$ ). . . . .	93
5.30	Comparison of measured and predicted transverse responses ( $R_e = 10^5$ and $KC = 8.4$ ). . . . .	94
5.31	Comparison of measured and predicted spectra of transverse responses ( $R_e = 10^5$ and $KC = 8.4$ ). . . . .	94
5.32	Thermistor power spectra at $\beta = 14,265$ and $y_{rms}/D = 29.5\%$ . . .	96
5.33	Thermistor power spectra at $\beta = 14,265$ and $y_{rms}/D = 20.9\%$ . . .	96
5.34	Thermistor power spectra at $\beta = 14,265$ and $y_{rms}/D = 8.2\%$ . . .	97
5.35	Thermistor power spectra at $\beta = 16,260$ and $y_{rms}/D = 16.8\%$ . . .	97
5.36	Thermistor power spectra at $\beta = 16,260$ and $y_{rms}/D = 8.8\%$ . . .	98
5.37	Schematic of the effect of transverse motion on the behavior of vortex-shedding frequency. . . . .	99
5.38	Thermistor power spectra at $\beta = 5,400$ and $y_{rms}/D = 56\%$ . . . .	101
5.39	Thermistor power spectra at $\beta = 6,500$ and $y_{rms}/D = 50\%$ . . . .	101
5.40	Thermistor power spectra at $\beta = 9,900$ and $y_{rms}/D = 16\%$ . . . .	102
5.41	Thermistor power spectra at $\beta = 9,900$ and $y_{rms}/D = 28\%$ . . . .	102
5.42	Thermistor power spectra at $\beta = 9,900$ and $y_{rms}/D = 35\%$ . . . .	103
5.43	Thermistor power spectra at $\beta = 9,900$ and $y_{rms}/D = 40\%$ . . . .	103
5.44	Thermistor power spectra at $\beta = 12,500$ and $y_{rms}/D = 33.5\%$ . . .	104
5.45	Schematic of vortex-shedding frequency behavior ( $\beta = 9,900$ ). . . .	104
5.46	Span-wise coherence length for transversely unconstrained articulated tower. . . . .	105
5.47	Transverse motion power spectra for $\beta = 5,400$ . . . . .	107
5.48	Transverse motion power spectra for $\beta = 6,500$ . . . . .	107
5.49	Transverse motion power spectra for $\beta = 9,900$ . . . . .	108
5.50	Transverse motion power spectra for $\beta = 12,500$ . . . . .	108

5.51	Transverse motion power spectra for $\beta = 14, 265$ . . . . .	109
5.52	Tower measured free oscillation in still water. . . . .	110
5.53	RMS transverse motion versus frequency ratio. . . . .	113
5.54	RMS transverse response versus reduced velocity. . . . .	114
5.55	Average highest 1/3 transverse response versus reduced velocity. .	115
5.56	RMS transverse response versus Kuelegan-Carpenter number. . .	115
B.1	X-Y force transducer and wheatstone bridge circuit. . . . .	130
B.2	Schematic of strain gauge amplifier/signal conditioning module. .	131
B.3	Calibration curve for in-line force (for test runs at $0.4 \geq f_d \leq 0.8 \text{ Hz}$ ). . . . .	132
B.4	Calibration curve for in-line force (for test runs at $0.15 \geq f_d \leq 0.3 \text{ Hz}$ ). . . . .	132
B.5	Calibration curve for transverse force. . . . .	133
B.6	Standard rigid linear displacement transducer. . . . .	133
B.7	Calibration curve of in-line linear displacement transducer. . .	135
B.8	Calibration curve of transverse linear displacement transducer. .	135
B.9	Schematic of thermistor signal processing circuit. . . . .	136
B.10	Schematic of thermistor testing set-up using flow visualization table.	137
B.11	Thermistor signal power spectra at various Reynolds numbers. .	138
B.12	Schematic diagram and frequency response for second order, passive, Butterworth lowpass filter circuit (designed for the feed back control signal). . . . .	139
B.13	Samples of transverse force signals and their corresponding power spectra (a) before filtering (b) after filtering. . . . .	140
C.1	Computer code flow chart for CDCM. . . . .	143
C.2	Computer code flow chart for CDCMN. . . . .	144
C.3	Computer code flow chart for CLEF. . . . .	145
C.4	Computer code flow chart for CLEUF. . . . .	146
C.5	Computer code flow chart for ATVSR. . . . .	147

## LIST OF TABLES

2.1	Categorization of flow and structural parameters influencing vortex-induced transverse loadings and response (numbers refer to references). . . . .	8
3.1	Test conditions for experiments I and II. . . . .	46
5.1	Samples of test results on in-line force data . . . . .	69
5.2	Test conditions for cases where large transverse motion were measured. . . . .	90
5.3	Results of lift coefficients when transverse motion existed. . . . .	91
B.1	Specifications of strain gage amplifier/signal conditioning module.	131
B.2	Linear displacement transducer specifications. . . . .	134
B.3	Thermistor specifications. . . . .	136
B.4	Linear drive motor specifications. . . . .	141

## LIST OF SYMBOLS

- $A$  — amplitude of transverse motion
- $A_R$  — transverse amplitude to cylinder diameter ratio
- $a$  — in-line motion amplitude at the driving mechanism
- $C_D$  — drag coefficient
- $C'_D$  — drag coefficient associated with velocity raised to power  $n$
- $C_m$  — added mass coefficient
- $C_M$  — inertia coefficient
- $C_s$  — structural damping coefficient
- $C_L$  — lift coefficient
- $C_{Ln}$  —  $n$ th harmonic lift coefficient
- $C_{Lmn}$  —  $n$ th harmonic lift coefficient of element " $m$ "
- $C_{Lmax}$  — maximum lift coefficient
- $C_{Lrms}$  — root mean square lift coefficient
- $d$  — water depth
- $d_1$  — water depth from the bottom hinge
- $dr$  — element length
- $D$  — cylinder diameter
- $E[C_L^2]$  — expected value of the square of the lift coefficient

- $f$  — frequency (  $Hz$  )
- $f_d$  — driving frequency (  $Hz$  )
- $f_n$  — system natural frequency (  $Hz$  )
- $f_r$  — cylinder response frequency (  $Hz$  )
- $f_v$  — vortex-shedding frequency (  $Hz$  )
- $f_w$  — fluid frequency of oscillation (  $Hz$  )
- $F_B$  — buoyancy force
- $F_D$  — drag force
- $F_L$  — transverse (lift) force
- $F_{rms}$  — root mean square force
- $F_{ymax}$  — maximum transverse force
- $F_{yrms}$  — root mean square of transverse force
- $g$  — acceleration of gravity
- $h$  — water depth
- $H$  — wave height
- $I_a$  — added mass moment of inertia
- $I_o$  — cylinder mass moment of inertia about bottom hinge
- $I_m$  — total cylinder mass moment of inertia about bottom hinge
- $k_s$  — restoring moment due to weight and buoyancy of the cylinder
- $k$  — wave number
- $KC$  — Keulegan-Carpenter number
- $K_s$  — stability parameter
- $\ell$  — cylinder length

- $\ell_s$  — cylinder submerged length  
 $L$  — vertical distance from bottom hinge to top hinge above the cylinder  
 $m_a$  — added mass per unit length  
 $m_s$  — cylinder mass per unit length  
 $M$  — ratio of  $f_r/f_d$   
 $M_D$  — moment about bottom hinge due to drag force  
 $M_{f_x}$  — moment about bottom hinge due to reaction "R" at the top hinge  
 $M_{f_y}$  — moment about bottom hinge due to total transverse force  
 $M_g$  — moment about bottom hinge due to weight and buoyancy of the cylinder  
 $M_L$  — measured moment due to total transverse force  
 $M_m$  — measured moment due to total in-line force  
 $M_{total}$  — total moment about bottom hinge  
 $N$  — ratio of  $f_v/f_d$   
 $r_i$  — distance of  $i$ th tower weight component from the bottom hinge  
 $r_n$  — distance of element  $n$  from the bottom hinge  
 $r$  — distance of a general tower element from the bottom hinge  
 $Re$  — Reynolds number  
 $R$  — reaction of the in-line driving force at the top hinge  
 $S(nf)$  — spectral density at frequency  $nf$   
 $S_t$  — Strouhal number  
 $S_{xx}(f)$  — auto-spectral density of signal  $x(t)$  at frequency  $f$   
 $S_{yy}(f)$  — auto-spectral density of signal  $y(t)$  at frequency  $f$   
 $S_{xy}(f)$  — cross-spectral density of signals  $x(t)$  and  $y(t)$  at frequency  $f$

- $T$  — period of flow oscillation
- $T_y$  — external generated turbulence
- $U$  — uniform flow velocity
- $U_{max}$  — maximum flow velocity
- $U_{rms}$  — rms of flow velocity
- $V_r$  — reduced velocity
- $w_i$  — weight of  $i$ th component of tower
- $X_m$  — measured in-line linear motion of the tower
- $y_m$  — measured transverse linear motion of the tower
- $\dot{y}_m$  — measured transverse linear velocity of the tower
- $\ddot{y}_m$  — measured transverse linear acceleration of the tower
- $y_p$  — predicted transverse linear motion of the tower
- $y_{rms}$  — rms of transverse linear motion of the tower
- $y_{1/3}$  — average of the largest 1/3 linear transverse motion of the tower
- $y$  — amplitude of transverse motion
- $Y_{rms}$  — maximum of rms amplitudes of transverse linear motion of the tower
- $z$  — span-wise coherence length of vortices
- $\beta_h$  — hydrodynamic damping coefficient
- $\beta$  — frequency parameter ( $= R_e/KC$ )
- $\gamma_{xy}(f)$  — correlation coefficient between signals  $x(t)$  and  $y(t)$  at frequency  $f$
- $\delta_1^2$  — average of least square errors
- $\delta$  — logarithmic decrement of free oscillation

- $\Delta_\ell$  — length of an element of the tower
- $\Delta_{r_\ell}$  — distance from in-line force reaction at top hinge to the center of in-line force transducer
- $\Delta_{r_t}$  — distance from transverse force reaction at top hinge to the center of transverse force transducer
- $\theta$  — in-line angular deflection of the tower
- $\dot{\theta}$  — in-line angular velocity of the tower
- $\ddot{\theta}$  — in-line angular acceleration of the tower
- $\nu$  — fluid kinematic viscosity
- $\xi$  — critical damping factor
- $\rho_w$  — mass density of water
- $\sigma_L^2$  — variance of transverse force
- $\sigma$  — circular frequency (*rad/sec*)
- $\phi_{(m)}$  — *mth* harmonic of the phase angle associated with lift coefficient
- $\psi_m$  — *mth* harmonic of the phase angle
- $\psi$  — transverse angular deflection of the tower
- $\dot{\psi}$  — transverse angular velocity of the tower
- $\ddot{\psi}$  — transverse angular acceleration of the tower
- $\omega$  — cylinder frequency (*rad/sec*)
- $\omega_d$  — cylinder driving frequency (*rad/sec*)
- $\omega_f$  — fluid frequency of oscillation (*rad/sec*)
- $\omega_v$  — vortex-shedding frequency (*rad/sec*)



Abstract of Dissertation Presented to the Graduate School  
of the University of Florida in Partial Fulfillment of the  
Requirements for the Degree of Doctor of Philosophy

## VORTEX-INDUCED TRANSVERSE LOADING ON AN ARTICULATED TOWER

By

AHMED FAHMY OMAR

August 1992

Chairman: Prof. D. Max Sheppard

Major Department: Coastal and Oceanographic Engineering

This research is an experimental investigation of vortex-induced transverse loading on fixed and compliant structures in nonplanar oscillatory flow. The effects of flow nonuniformity and transverse motion on the transverse force, vortex-shedding frequency, and vortex span-wise coherence length have been investigated. To quantify such effects, two types of experiments were performed. Each type of experiment consisted of a series of tests. All tests were performed by oscillating an instrumented 10 ft long, 6 inch diameter aluminum, articulated cylinder in a 30 ft diameter cylindrical tank with a water depth of 8.5 ft. In the first type of experiment, transverse motion was not allowed, while in the second type, the cylinder was allowed to move freely in the transverse direction. Reynolds numbers,  $Re$ , between  $0.61 \times 10^4$  and  $1.3 \times 10^5$  and Keulegan-Carpenter numbers,  $KC$ , between 2.4 and 9.35 were obtained. A new method, involving the use of miniature, quick response thermistors was employed for measuring frequency of vortex-shedding.

For the range of  $Re$  and  $KC$  tested, transverse force amplitudes as large as 70% of the in-line force were measured. Transverse forces occurred at frequencies that were multiples of the driving frequency. The dominant vortex-shedding frequencies

clustered around one of the harmonics of the driving frequency. The specific harmonic depended on the value of  $KC$ . A mathematical model for computing transverse forces taking into account the dependency of the lift coefficient on both  $R_e$  and  $KC$  as well as the fact that these forces have multiple frequency components has been also proposed. Using this model, the magnitude of the transverse force was found to be deterministic and repeatable. However, the phase of this force was random in nature. The constrained tower results for in-line and transverse force coefficients were found to agree well with data obtained by others for waves acting on vertical cylinders.

Transverse motion was found to have a significant effect on vortex-induced loading. The effect of transverse motion was also found to increase the vortex correlation length, increase the lift coefficient (by at least two and one-half times) and alter the nature of the vortex-shedding. For the range of  $KC$  tested, the results showed that, the larger the value of  $KC$ , the larger the amplitude of maximum transverse motion and the larger the value of reduced velocity,  $V_r$ , at which this maximum occurs.

## CHAPTER 1 INTRODUCTION

### 1.1 Problem Statement

With the depletion of near shore oil reservoirs, exploration and production is moving to deeper water and more remote locations. In most cases, this means more severe environmental conditions and more stringent design and safety regulations. At the same time, there is a great need to reduce the cost of producing hydrocarbons. One way to cut the cost is to optimize structural designs. An essential component of optimization is being able to predict accurately the loadings to be experienced by the structure. This trend has recently led to a massive research effort into the design and assessment of the short and long term reliability of offshore structures. The design usually involves three major steps, first, the long term prediction of environmental conditions, second, the estimation of the forces associated with these environmental conditions and third, the determination of the effects of these forces on an intended structure and its ability to survive the expected extreme environment. It is interesting to note that by 1970, over 10% out of 200 drilling rigs had collapsed and a further 20% had suffered severe fatigue failure of structural members due to flow-induced vibrations (King, 1974). This is in addition to frequent shut-down of operation for days due to the large oscillations induced by fluid-induced forces; see Lewis *et al.* (1991) and Koch *et al.* (1991).

In the past two decades, a significant amount of research on fluid-structure interaction problems has been conducted. This research can be divided into two categories, those concerned with i) the fluid-induced forces and ii) the fluid-induced response and/or vibration. The latter category has received the most attention.

The fluid-induced forces are comprised of in-line forces and vortex-induced transverse (lift) forces. Many studies have been done to predict the fluid in-line forces acting on a cylinder in steady and oscillating flow. The majority of those studies have been based on the Morison equation (Morison *et al.*, 1950), where the two in-line force components of drag and inertia are identified. The equation expresses these forces in terms of the velocity and acceleration of the fluid particles at the location of the cylinder. In comparison to in-line forces, vortex-induced transverse forces have received little attention. This is most likely due to the complexity of the vortex-shedding phenomena and the lack of a clear cut methodology for analyzing the data.

Structural elements are constantly subjected to loading due to wind and/or ocean currents and waves. Most flow situations encountered in nature are turbulent, non-planar (nonuniform), and unsteady. To further complicate matters, the structural element of interest is often in close proximity to other members, compliant, and perhaps partially covered with biofouling. To predict the vortex-induced transverse loading and response of such a structural element under such complex flow conditions is truly a challenging task, but nevertheless, one that is routinely faced by design engineers in the offshore industry.

The problems of in-line and transverse loading and the corresponding structural response are all related and interdependent. However, the quantities involved are difficult to isolate and to measure; and, therefore some of the reported data have been affected by the techniques, apparatus and/or instrumentation used. In addition, the diversity of the investigators' backgrounds, ranging from fluid to structural mechanics, resulted in differences in approaches taken and differences in the manner in which results were presented. This diversity of backgrounds has its advantages, but the lack of uniformity in data reporting makes it difficult to compare and extend data sets.

The focus of this research was on the investigation of some of the fluid-structure interaction problems, in particular on quantifying the effects of flow nonuniformity

and transverse motion on vortex-induced transverse loading and on developing a mathematical model for predicting transverse forces.

It is extremely difficult to obtain a theoretical solution for vortex-induced transverse forces especially at high Reynolds numbers. The difficulty is partly due to incomplete knowledge of the flow field around the structure, and to problems associated with the coupling of structural motion and fluid flow. Consequently, the approach for obtaining the solution to this problem has been the same as taken here, i.e. experimental.

## 1.2 Research Objectives

The overall objectives of this study were

1. To design and conduct experiments to establish the dependence of the vortex-shedding process, vortex span-wise coherence length, magnitude of the vortex-induced transverse forces and transverse motion on the in-line flow and structure parameters. The physical model must be sufficiently large to cover meaningful ranges of Reynolds ( $Re$ ) and Keulegan-Carpenter ( $KC$ ) numbers and
2. To develop an improved mathematical model for predicting vortex-induced transverse forces.

To achieve these objectives, the following tasks were performed:

1. Design, construct and instrument an articulated tower system. Two designs were necessary, one with and one without transverse motion.
2. Perform two types of experiments by sinusoidally oscillating the articulated tower in an otherwise still-water tank. In the first type the tower transverse motion was constrained. During the series of tests performed for this type, the following quantities were measured

- the in-line and transverse forces.
- the frequencies of vortex shedding along the physical model.
- the in-line motion.

During the series of tests for the second type, transverse motion was allowed and the following quantities were measured

- the in-line forces.
  - the in-line and transverse motion.
  - the frequencies of vortex shedding along the physical model.
3. Develop a mathematical model for predicting the vortex-induced transverse forces.
  4. Quantify the effects of flow nonuniformity and structure's transverse motion on the lift coefficients, frequency of vortex-shedding and spanwise coherence length of vortices.

## CHAPTER 2 LITERATURE REVIEW

In this chapter, a literature review and discussion of topics relevant to the work undertaken are presented. The review is limited to the vortex-shedding process and its induced transverse forces and concentrates on smooth, rigid cylinders in 1) steady, planar, 2) oscillatory, planar, 3) oscillatory, nonplanar, and 4) wave flows. The effects of transverse motion on the vortex-shedding process, span-wise coherence length and transverse loading are also discussed for those cases where sufficient data exist. It is the author's opinion that the above classification of quantities affecting vortex-induced loading and response will be beneficial in analyzing data from various investigators and in understanding the processes involved.

Analytical and computational approaches to the transverse force problem have been hampered by the complexity of the processes. Thus, most of the work to date has been experimental, guided by dimensional analysis techniques. For this reason, only experimental work will be discussed in this review.

### 2.1 Overview

When a viscous fluid such as water or air flows past a bluff body with sufficient velocity, flow separation occurs and a wake region is formed. Over a wide range of flow and structure parameters of interest, vortices are observed to form near the points of flow separation. For symmetric structure shapes, void of sharp edges, such as right circular cylinders, vortices are formed on both sides of the body. Under certain conditions these vortices remain attached to the body while under other conditions they are shed from the body in or out of phase with each other. The net effect of this phenomenon is a fluctuation in the points of flow separation, which in turn causes

a time varying distribution of normal and tangential stresses over the body. This results in time dependent in-line and transverse loads on the structure, even when the flow is steady and planar (uniform).

The processes associated with flow separation are complex and difficult to predict. Yet minor changes in the separation point can result in relatively large changes in both the in-line and the transverse forces on the structure. This flow instability problem is sensitive to perturbations such as those introduced by surface roughness, motion of the body, free stream turbulence, flow orientation relative to the structure, flow around the ends of the structure, etc. In an attempt to understand and model this phenomenon, researchers have isolated various aspects of the problem starting with the (seemingly) simplest case of uniform, steady flow and moving toward the more complex flow and structure situations. The processes are of course nonlinear and thus their individual effects cannot be simply superimposed to obtain the combined effect. However, much can be learned about the mechanisms involved and some guidance for the design engineer can be achieved by such a process.

Vortex-induced loads are of interest in a number of engineering disciplines and of particular importance in the design of offshore structures. Structural elements of interest are often compliant and subjected to complex flows (turbulent, oscillatory and nonuniform). For such a situation, the main danger from the vortex-induced loading arises from the possibility of resonance created by the vortex-shedding frequency being close to the system natural frequency (or one of its multiples). Large and damaging amplitudes of oscillation can result from the complicated and pernicious mechanism of resonance which can occur over a considerable range of conditions. The interaction between the flow and the structure's motion causes the frequency of vortex-shedding to be controlled by the response. This can result in what is known as "lock-in". Although the fluctuating pressure that causes the transverse force is predominantly at right angles to the direction of the approaching flow, it can also produce dynamic



forces in-line with the flow. The induced transverse motion can also increase the time-average drag significantly.

The problems of in-line and transverse loading and the corresponding structural response are all related and interdependent as pointed out in several excellent reviews on this subject (e.g. Bearman, 1984; Sarpkaya, 1979; Chen, 1987; Griffin, 1984). On the other hand, transverse forces depend on the nature of the flow, the structure's geometric parameters, and (when it exists) the structure motion. This is illustrated in the diagram in Fig. 2.1. As stated above, the flows are very complex. Perhaps the most surprising thing about this phenomenon is that it displays some degree of order and repeatability and thus predictability.

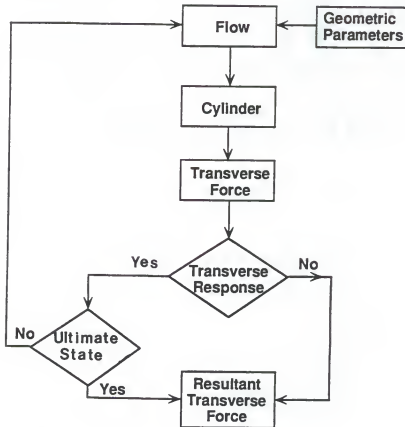


Figure 2.1: Flow chart for cylinder-loading response.

The quantities involved are difficult to isolate or to measure and therefore some of the reported data have been affected by the techniques, instrumentation and/or

apparatus used. In spite of these difficulties, researchers have managed to acquire at least a qualitative understanding of most of the processes and how the various geometric and flow parameters affect the transverse force. The matrix presented in Table 2.1 is an attempt to classify the existing work from the point of view of the more important geometric and flow parameters affecting the vortex-shedding process and the resulting transverse forces. Reference numbers for some of the more recent and historically important papers on the various subjects are given in the matrix. For a more complete list of references on these subjects the reader is referred to the review articles by Bearman (1984), King (1977) and Sarpkaya (1979). As one can see from Table 2.1, some areas have received more attention than others (e.g. steady and oscillatory planar flows have attracted most of the interest while other flows like oscillatory nonplanar and waves have received less attention). The author is aware that important proprietary research has also been conducted in this field, but these results are, of course, not available for review.

Table 2.1: Categorization of flow and structural parameters influencing vortex-induced transverse loadings and response (numbers refer to references).

Flow	Structure Parameter (Rigid Cylinders)							End Effects
	Smooth	Rough	Fixed	Inline Motion	Transverse Motion	L/D	BR	
Steady, Planar	1, 18, 34, 63, 71, 76, 77, 55, 19, 75, 67, 33, 17	1, 18	1, 76, 77, 55, 19, 75, 67, 17	63, 33	18, 34, 63, 71, 75, 33	77	77	19
Oscillatory, Planar	60, 61, 2, 40, 46, 71, 74, 76, 80, 43, 50, 32, 3, 45, 42, 69, 47, 78, 56, 70, 17	62, 60, 61, 71, 45, 56, 70	62, 60, 61, 76, 80, 43, 50, 32, 3, 45, 42, 69, 47, 78, 17		2, 40, 46, 71, 74, 42, 56, 70		74, 80	43
Oscillatory, Non-planar	13, 11		13, 11					
Regular Waves	7, 30, 65, 12, 11, 44, 76, 9, 66	11	7, 30, 12, 11, 44, 76, 9, 66	65, 11, 44, 76	7, 65, 44, 76			
Irregular Waves	73, 23		73, 23					

Some of the earliest studies were on steady, planar, relative flow, perpendicular to rigid, fixed, circular cylinders (see King, 1977; Fleischmann and Sallet, 1981; Blevins, 1990). The term relative flow is used since in some cases the cylinder was towed through still water while in other cases the fluid was forced to move around a fixed cylinder. This was followed by experiments with oscillatory, planar, relative flow around circular cylinders. More recent experiments with oscillatory, nonplanar, relative flows have been performed both by moving articulated cylinders in still-water (Chakrabarti *et al.*, 1983) and by subjecting cylinders to surface waves (see Bearman, 1988a; Isaacscon *et al.*, 1976, 1977; Sawaragi *et al.*, 1977; Chakrabarti *et al.*, 1976). While the above work was proceeding, other aspects of the problem such as the effects of surface roughness (e.g. Achenbach and Heinecke, 1981; Bearman, 1988a; Sarpkaya, 1976a, 1976b, 1990b; Wolfram *et al.*, 1989), in-line and/or transverse motion (e.g. Chakrabarti *et al.*, 1984; Maull and Kaye, 1988; Bearman and Hall, 1987; Donazzi *et al.*, 1981; King, 1974; Laird, 1962; McConnell and Park, 1982a; Sarpkaya, 1978; Sumer and Fredsøe, 1988; Tørum and Anand, 1985; Verley, 1980), structure aspect ratio (i.e., cylinder length to diameter ratio) (e.g. West and Apelt, 1982), flow blockage (e.g. Kozakiewicz *et al.*, 1991; Tørum and Anand, 1985; Ramamurthy and Ng, 1973; Yamamoto and Nath, 1976), free stream turbulence (e.g. Tørum and Anand, 1985), end effects (e.g. Tørum and Anand, 1985; Matten *et al.*, 1978), etc. were also being investigated. One of the factors affecting the overall lift coefficient is the span-wise coherence length of the vortices (i.e. the length along the axis of the cylinder where the vortices are being shed in unison). Even though this parameter length has been the subject of much discussion, very few measurements with circular cylinders in water have been reported in the literature (see King, 1977; Wolfram *et al.*, 1989; Obasaju *et al.*, 1988; Kozakiewicz *et al.*, 1991). It is thought that this length depends on: cylinder aspect ratio, end effects, free stream turbulence, nonuniformity of the in-line flow, roughness and roughness gradients along the cylinder, two and three

dimensionality of the flow (such as would be generated by uni- and multi-directional surface waves, respectively), nonaligned currents and waves, etc.

During the past few decades, much has been learned about the vortex-induced transverse force problem; yet it is safe to say that more work is needed before reliable information required by design engineers is available. In the following sections a review of the vortex-induced transverse forces (in particular, the lift coefficients and frequency of vortex-shedding) and span-wise coherence length of vortices on smooth, fixed and transversely unconstrained cylinders in 1) steady, planar, 2) oscillatory, planar, 3) oscillatory, nonplanar, and 4) wave flows is presented. Lock-in conditions and their relation to the vortex-shedding frequency and the system natural frequency are also presented where sufficient data exist. Flexible cylinders will not be discussed in this review. This is because it is difficult to devise experiments with flexible cylinders that provide quantitative results specifically on the effects of flow nonuniformity. Results obtained from the more easily controlled experiments discussed here could; however, be helpful in analyzing the loading and response of flexible cylinders.

## 2.2 Steady, Planar Flow

### 2.2.1 Transversely Constrained Cylinder in Steady, Planar Flow

Vortex-induced transverse forces on a smooth, circular cylinders in steady, planar, flows have received considerable attention during this century (see e.g. King, 1977; Fleischmann and Sallet, 1981). For this type of flow, it was found that Reynolds number,  $R_e$  (relative magnitudes of inertia and viscous forces), was the most important parameter to characterize the flow around a circular cylinder. For steady, turbulent flows around right circular cylinders, the in-line loading has been formulated in terms of a drag force that is proportional to the square of the relative speed, the mass density of the fluid, and a projected area. The constant of proportionality is one-half the drag coefficient ( $C_D/2$ ). Plots of  $C_D$  versus  $R_e$  for this flow situation can be found in numerous publications (e.g. Sarpkaya and Isaacson, 1981). In the

absence of a better formulation, a similar model for the transverse or lift force in terms of the in-line relative speed squared, fluid mass density, and projected area has also been used. In this case, the constant of proportionality is one-half the lift coefficient ( $C_L/2$ ). In both cases, the coefficient is a catch-all term whose value depends to some degree on the flow and most, if not all, of the quantities given in Table 2.1.

Sarpkaya and Isaacson (1981) showed that there is considerably more scatter in  $C_L$  data for this flow than say for  $C_D$ . In an attempt to show both the consistency and the scatter in the available experimental data,  $C_{L(rms)} (\equiv 2F_{rms}/\rho_w DU^2)$  versus  $R_e (\equiv UD/\nu)$  has been plotted in Fig. 2.2 for twelve different investigators. Most of these data were taken from Sarpkaya and Isaacson (1981), but the results of two more recent studies (Dronkers and Massie, 1978; van der Vegt and van Walree, 1987) have been added. However, it should be pointed out that many of these data are for experiments conducted some years ago in air. In addition, it is possible that at least some of the cylinders experienced transverse vibration during the tests. Dronkers and Massie (1978) had a fixed vertical cylinder in a circulating flume while van der Vegt and van Walree (1987) towed a horizontal cylinder in still-water. These data appear to only add to the scatter. This lack of agreement in the reported data has been attributed to differences in free stream turbulence, aspect ratios, flow uniformity, etc.

In structural design, the frequency components of the transverse force are perhaps as important as the magnitude. The basic phenomenon of vortex-shedding is illustrated in Fig 2.3, where the major regimes of vortex-shedding from a right circular cylinder in steady, planar flow are sketched, based upon the observations of various investigators.

Recently, a flow visualization by van der Vegt and Walree (1987) has confirmed some of the patterns by which the vortex-shedding process occurs as presented in Fig. 2.3. In all the investigations carried out in this category, the frequency with which the individual vortices are shed was found to be proportional to the ratio  $U/D$ ,

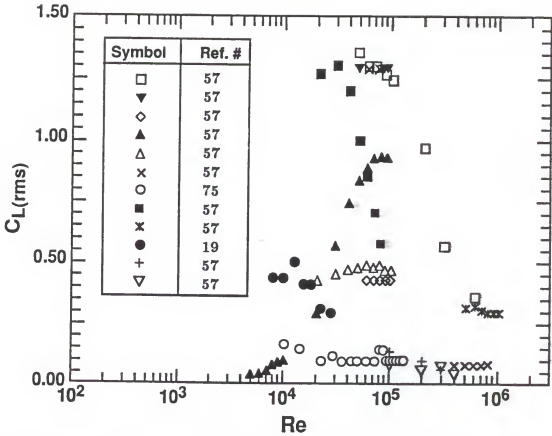


Figure 2.2: Lift coefficient versus Reynolds number for steady, planar flow around a smooth, fixed cylinder.

so that  $f_v = S_t U/D$ , where the constant of proportionality is called Strouhal number and  $f_v$  is the frequency of vortex-shedding. Later  $S_t$  was presented versus  $Re$  in an envelope, within  $\pm 10\%$  accuracy over a large Reynolds number range, see Fig. 2.4. Transverse force spectra (in this case, spectral density versus Strouhal Number) for various values of  $Re$  are also shown in Fig. 2.4. These spectra were computed by Schewe (1983), using data from steady flow around a fixed, rigid cylinder in a pressurized wind tunnel. It is important to note the relative energy levels in the various flow regimes. Single spike spectra similar to Schewe's spectra for  $Re = 1.3 \times 10^5$  (see Fig. 2.4) were recently obtained for water flows by van der Vegt and van Walree (1987). Thus for all practical purposes, it appears that vortices are shed at a single frequency for  $60 < Re < 2 \times 10^5$  and well defined by a Strouhal number of about 0.2 for smooth cylinders.

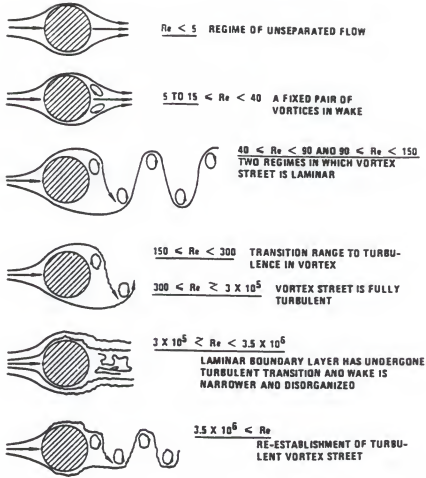


Figure 2.3: Regimes of steady, planar flow across a smooth, fixed circular cylinder, (Ref. 14).

Patal (1989) and others presented the relationship of Fig. 2.4 in the form of empirical equations:

$$f_v = (S_t U/D) \quad R_e < 60 \quad (2.1)$$

$$f_v = S_t (1 + 19.7/R_e)(U/D) \quad 60 < R_e < 2 \times 10^5 \quad (2.2)$$

In the turbulent regime ( $2 \times 10^5 < R_e < 7 \times 10^6$ ), the Strouhal number varies between 0.15 and 0.4 depending on the intensity of the free stream turbulence. In this region, the spectrum is broad banded, reduced in magnitude and very sensitive to flow disturbance. In the supercritical regime ( $R_e > 7 \times 10^6$ ), the spectrum becomes narrow banded once again.

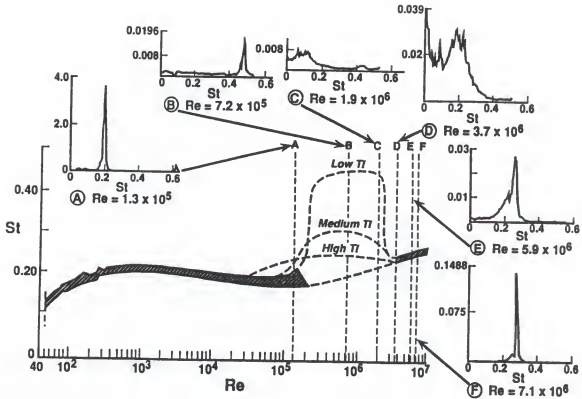


Figure 2.4: Strouhal-Reynolds numbers relationship with transverse force spectra for steady, planar flows around a smooth, fixed cylinder (Refs. 14, 67).

The vortices shed along a cylinder can be in or out of phase with each other. The total transverse force on the cylinder is very sensitive to these phase angles. It is important to understand what quantities control or influence the shedding process. A parameter known as the span-wise coherence length (a length over which the vortices are considered well correlated) has been used as a measure of the coherence between the vortices shed along a cylinder. In general, the greater the coherence length the larger the total transverse force. This correlation length has been observed to vary with Reynolds number, surface roughness and free stream turbulence (King, 1977). The only data found that demonstrate the parameters influencing the coherence length support the importance of the Reynolds number ( $Re$ ). These data (by Scruton, 1967; taken from Overvik, 1982) are shown in Fig. 2.5 and generally indicate a reduction in the span-wise coherence length with increased Reynolds number.



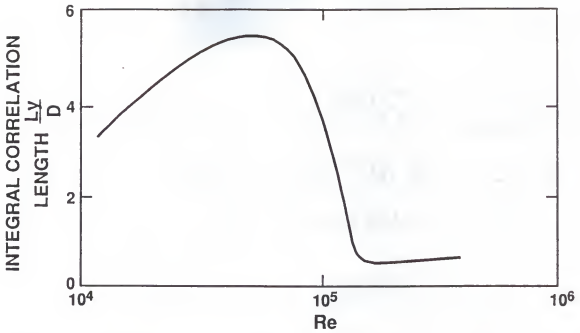


Figure 2.5: Span-wise coherence length versus Reynolds number for steady, planar flow around a smooth, fixed cylinder (Ref. 68).

### 2.2.2 Transversely Unconstrained Cylinder in Steady, Planar Flow

When the structure is allowed to move in the transverse direction and its support is such that a restoring force exists (resulting in a system natural frequency), there can be strong interaction between the transverse response and the transverse loading as indicated in Fig. 2.1. Extreme caution, therefore, should be exercised when using lift coefficient data obtained for fixed cylinders when the structural element is compliant. When the vortex-shedding frequency is in the vicinity of the natural frequency of the cylinder-support system, large transverse excursions can occur which in turn result in further increases in the transverse force. This large amplitude motion at the natural frequency can change the frequency of vortex-shedding to that of the oscillation frequency and “lock-in” occurs.

Even though a number of experiments have been performed with cylinders free to move in the transverse direction, only a few investigators (e.g. King *et al.*, 1973; King, 1974; Griffin and Koopman, 1977; Tørum and Anand, 1985) have reported

information on the response of the cylinder. The spectra of the transverse force and corresponding response by Tørum and Anand (1985) were the only data found that show the relationship between the vortex-shedding frequency ( $f_v$ ) and response frequency ( $f_r$ ). Tørum and Anand's investigation was primarily to study wall effects, however, their results for the largest cylinder gap to diameter ratio (i.e.,  $G/D = 3$ ) shown in Fig. 2.6 should be very similar to an unobstructed cylinder. For these data, the authors did not report the values of Reynolds numbers. A value of  $\nu \simeq 10^{-6} \text{ m}^2/\text{sec}$  was assumed in the computations of  $R_e$  shown in the figure.

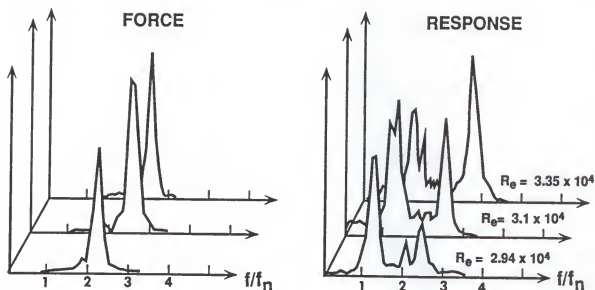


Figure 2.6: Schematic transverse force and corresponding response power spectra for steady, planar flow around a smooth, transversely unconstrained cylinder (Ref. 74).

The spectra given by the authors were only for the conditions after lock-in. For those conditions, Fig. 2.6 shows that the vortex-shedding frequency displays a dependency on Reynolds number as for the fixed cylinder. As the vortex-shedding frequency moves further from the system natural frequency the response at the natural frequency decreases while the response at the vortex-shedding frequency increases. In a plot of vortex-shedding frequency versus velocity their results show that the vortex-shedding frequency follows the  $S_t = 0.2$  relationship except in the neighborhood of the natural frequency where lock-in occurs.

It is known that the transverse motion of the cylinder has a significant effect on the vortex correlation and consequently on the transverse force. It has been demonstrated by Koopman (1967) and Toebe (1969) that the vortex span-wise coherence length for a transversely unconstrained cylinder exposed to a steady, planar current increases drastically with increasing amplitudes of oscillations. However, the author has not been able to locate information on lift coefficients for this flow situation.

### 2.3 Oscillatory, Planar Flow

#### 2.3.1 Transversely Constrained Cylinder in Oscillatory, Planar Flow

In oscillatory, planar flow around rigid, stationary cylinders both the acceleration and relative velocity of the free stream are constantly changing with time, but are uniform along the cylinder. The dimensionless groups that characterize this flow situation are the Reynolds Number ( $R_e = U_{max}D/\nu$ ) and Keulegan-Carpenter Number ( $KC = U_{max}T/D = 2\pi A/D$ ). Combinations of these groups such as  $\beta = R_e/KC$  have also been used to correlate and present experimental data with varying degrees of success. Several different lift coefficients have been used ( $C_{Lmax} = 2F_{ymax}/\rho DU_{max}^2$ ,  $C_{Lrms} = 2F_{yrms}/\rho DU_{max}^2$ ,  $C_{Lrms} = 2F_{yrms}/\rho DU_{rms}^2$ , etc.) to present results (often without specifying which was used). Since the transverse force had been found in nature to exhibit some degree of irregularity, many investigators have commonly used an *rms* lift coefficient ( $C_{Lrms}$ ) and so is this review.

The investigations for this flow were conducted by oscillating the flow past a fixed cylinder or by oscillating a rigid cylinder in still-water. Some very good work has been done in this area resulting in the largest data set for  $C_L$  of any of the categories outlined in Table 2.1. In an attempt to compare the results, the author compiled *rms* lift coefficient data for smooth cylinders from a number of these investigations and plotted them versus  $KC$ . Some of the data were taken holding  $R_e$  constant while other investigators maintained  $\beta$  constant. These data are plotted separately in Figs. 2.7 and 2.8. Those data not reported in terms of  $C_{Lrms} = 2F_{yrms}/\rho DU_{max}^2$

were converted to this definition prior to plotting. The data for Chaplin (taken from Bearman, 1988b) and Justesen (1989) in Fig. 2.7 had to be converted. Other investigators' data (such as Bearman *et al.*, 1984; Maull and Milliner, 1987) are not shown since they presented their data in a manner that would be difficult, if not impossible, to convert to the coordinates used in these figures. In Fig. 2.7 recent data from Longoria *et al.* (1991) are presented along with those for Sarpkaya (1990a) and Skomedal (1989). Both plots show that the lift coefficient is a maximum at  $KC$  between 10 and 12. There is surprisingly good agreement among the data within each of the two plots. The fact that both plots have the same shape and magnitude means that for oscillatory, planar flow the lift coefficient depends primarily on the Keulegan-Carpenter number.

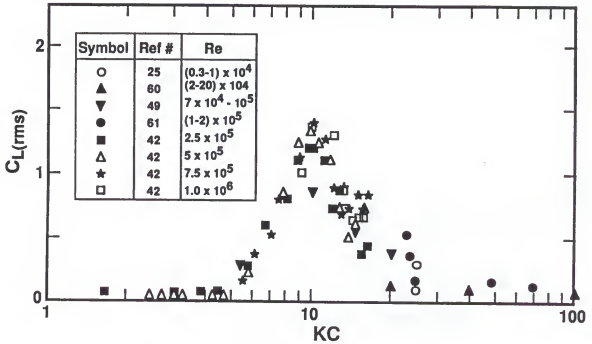


Figure 2.7: Lift coefficient versus Keulegan-Carpenter number for oscillatory, planar flow around a smooth, transversely constrained cylinder (for constant Reynolds number,  $Re$ ).

The basic nature of the flow in this category depends on the period of time for which the flow continues in one direction before it reverses. If the period is very short,

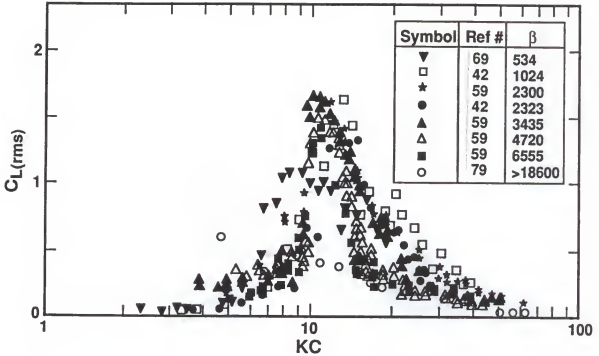


Figure 2.8: Lift coefficient versus Keulegan-Carpenter number for oscillatory, planar flow around a smooth, transversely constrained cylinder (for constant frequency parameter,  $\beta$ ).

there will not be sufficient time for the vortices to form before the flow reverses. If the period is very long, the flow will be quasi-steady and will have the character of streaming flow, first in one direction and then in the other. For flow periods between these extremes some downstream vortex effects will occur. In nondimensional terms, it was found that, the parameter that best determines the general character of vortex-shedding from a circular cylinder in oscillatory flows is the ratio of how far a fluid particle moves in one half-cycle to the characteristic cylinder dimension that the particle flows past. This nondimensional term is what is known by the Keulegan-Carpenter number " $KC = U_{max}T/D$ ".

Since the early seventies many vortex-shedding flow visualization studies have been conducted for this flow situation. Most of these investigations were carried out to further the understanding of the mechanisms and thus help in the development

of numerical models for predicting transverse force. Detailed descriptions of these processes have been given by Bearman (1988b), Sarpkaya (1976a), Skomedal *et al.* (1989) and Williamson (1985). Even though there is general agreement on the nature of the vortex shedding processes there are differences among researchers regarding the details. The subjectivity in the flow visualization techniques used to measure the conditions under which vortices are shed, the number shed, etc. probably accounts for many of the differences.

Experimentally, the frequency of the vortex-shedding is computed from the spectral analysis of the transverse force. It is surprising that more investigators have not reported transverse force spectra. The spectra that have been reported (Justesen, 1989,  $KC = 1.7$  to  $15.6$ ; Bearman and Hall, 1987,  $KC = 36.13$ ; McConnell and Park, 1982b,  $KC = 37.7$ ), are shown, schematically, in Fig. 2.9. The intent of this plot is to illustrate the behavior of the frequency and not the magnitude of the spectral density of the transverse force. The results are by no means conclusive, but the vortex energy for this flow appears to cluster around one of the harmonics of the in-line driving (or flow oscillation) frequency with moderate energy in the surrounding harmonics, depending, primarily, on the value of  $KC$ . As  $KC$  increases the frequency of vortex-shedding increases.

Correlation measurements have also been made for a fixed cylinder in oscillatory, planar flow, but unfortunately, only those results for correlation length measured by Obasaju *et al.* (1988) have been reported. They measured the span-wise correlation of vortex-shedding for a range of  $KC$  from 4 to 55. Their results show that the correlation length does not decrease monotonically with increasing  $KC$ . The highest correlation length was obtained at  $KC = 10$  (see Fig 2.10) and at this value it was approximated by  $4.5D$ . They also found that for  $KC > 30$  the correlation is no longer sensitive to  $KC$ .

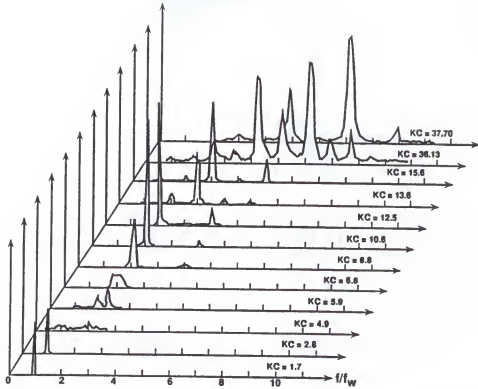


Figure 2.9: Schematic transverse force power spectra for oscillatory, planar flow around a smooth, transversely constrained cylinder for various Keulegan-Carpenter number,  $KC$  (Refs. 2, 32, 47).

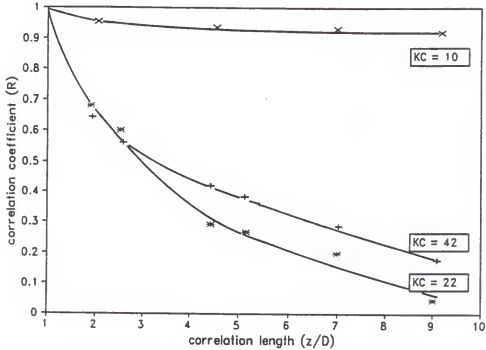


Figure 2.10: Span-wise coherence length for transversely constrained cylinder in oscillatory, planar flow (Ref. 50).

### 2.3.2 Transversely Unconstrained Cylinder in Oscillatory, Planar Flow

The work conducted for this case can be put into two categories; 1) that which is concerned with the effect of the transverse motion on the transverse force (McConnell and Park, 1982a, b; Sarpkaya and Rajabi, 1979) and 2) that which is concerned with determining the conditions under which transverse motion can be excited (Bearman and Hall, 1987; Sarpkaya and Rajabi, 1979; Sumer and Fredsøe, 1988, 1989). In general, when the cylinder is allowed to have transverse motion, the vortex-shedding frequency as well as the strength of the vortices is modified. For this situation  $KC$  alone is no longer adequate to characterize the transverse loading. This was clearly demonstrated by Sumer and Fredsøe (1988, 1989) in their experiments that covered a wide range of  $KC$  ( $KC = 10$  to  $100$ ) and a large range of reduced velocity,  $V_r = U_{max}/Df_n = 2\pi(A/D)(f_w/f_n) = KC(f_w/f_n)$ . Their results demonstrated that, at least for the range of  $KC$  tested, both  $V_r$  and  $KC$  are necessary to describe the behavior of the transverse response. Their plots of transverse motion due to vortex-shedding, i.e.,  $y_{rms}$  versus  $V_r$  for constant values of  $KC$  show that for lower  $KC$  (up to  $\approx 10$ ) a single spike exists. As  $KC$  increases, the number of spikes increases until at  $KC \approx 100$  the response versus  $V_r$  is flat for  $6 < V_r < 11$ . The reader is referred to their paper for a detailed interpretation of this behavior.

To the author's knowledge, McConnell and Park (1982a) are the only investigators reporting lift coefficients for this situation. Their results showed that the lift coefficient increased up to twice that for a fixed cylinder. Others presented only structure response information such as  $y_{rms}/D$  or  $y_{max}/D$  versus  $V_r$  or  $f_w/f_n$  ratio.

As shown in Fig. 2.1, when transverse motion exists there can be an interaction between the response and the transverse force. The level of this interaction is very much dependent on how close the stationary vortex-shedding frequency is to the system's natural frequency. In order to study this phenomenon the transverse force and response should be measured simultaneously. Of the literature reviewed,



only McConnell and Park (1982b) reported spectra for both transverse force and the corresponding response. Schematized versions of these spectra are presented in Fig. 2.11. The frequency for the force and response spectra has been normalized by the cylinder natural frequency in still-water. Their results showed for  $4.4 < V_r < 6.6$  and  $f_n/f_d = 6.22$  lock-in occurred, i.e.,  $f_r/f_n = f_v/f_n = 1$ . This shows that it is not necessarily for  $f_n/f_d$  to be an integer to have a lock-in. Their results also show (at least qualitatively) the influence of the transverse motion on the frequency of vortex-shedding.

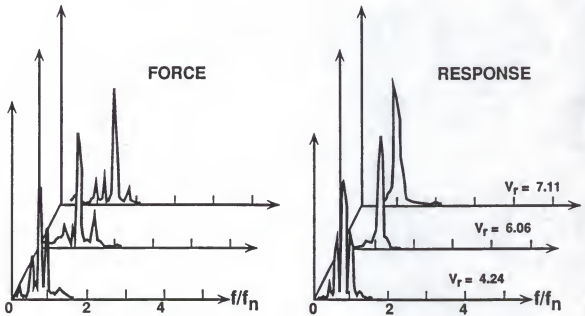


Figure 2.11: Schematic transverse force and corresponding response power spectra for oscillatory, planar flow around a smooth, transversely unconstrained cylinder for various reduced velocities,  $V_r$  (Ref. 47).

Data or information on the vortex span-wise coherence length for this category was not available until recently when Kozakiewicz *et al.* (1991) measured and reported the correlation length for a vibrating cylinder near a wall. The study is not directly related to the work undertaken here as it was mainly concerned with the wall effect on the vortex correlation; however, some insight can be gained from the results. Their results for the largest gap/diameter ratio (that is  $G/D = 2.3$ ) are reproduced

in Fig. 2.12. As shown in this figure the correlation between vortices is largest at  $KC = 6$  (as compared to  $KC = 10$  for a fixed cylinder [Obasaju *et al.*, 1988]) and like the case of fixed cylinder is mainly dependent on  $KC$ . The results of their study also showed that for a fixed  $KC$  the larger the amplitude of transverse motion the larger the correlation.

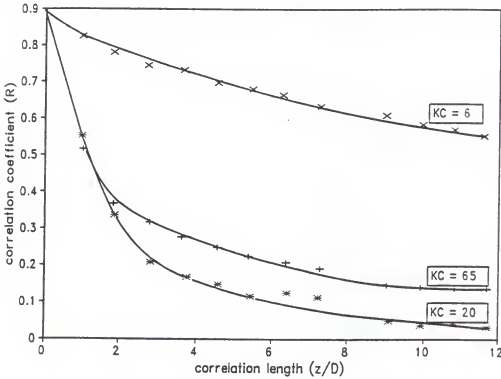


Figure 2.12: Span-wise coherence length for transversely unconstrained cylinder near a wall in oscillatory, planar flow (Ref. 39).

#### 2.4 Oscillatory, Nonplanar Flow

The final flow configuration to be considered in this review is that of nonplanar, oscillatory relative flow around rigid, circular cylinders. Very little work has been done with these flow conditions as can be seen from Table 2.1. The need for information on the effects of flow nonuniformity and transverse motion on transverse force and vortex span-wise coherence length was the motivation for the work of this dissertation.

Both transversely constrained and unconstrained cylinders will be discussed in this section. Surface waves acting on vertical cylinders are also included in this

category, but will be treated separately due to the effects of the vertical component of water particle velocity on the transverse force.

The question is, what effect does flow nonuniformity have on the transverse force? More specifically, what effect does it have on the span-wise coherence of the vortices? Does the coherence length of the vortices diminish with nonuniformity as a result of  $KC$  gradients along the cylinder or do the higher energy vortices, associated with the regions of higher velocity and vorticity, dominate the shedding process? Also, what effect does the transverse motion of the structure have on the vortex-shedding process and transverse force?

Chakrabarti *et al.* (1983) and Chakrabarti and Cotter (1984) conducted experiments on an articulated cylinder where the top was oscillated sinusoidally while constraining the transverse motion. They measured local and total forces on the cylinder and, among other things, investigated the frequency and magnitude of the transverse force for a range of  $KC$  values. They used a five term Fourier series (similar to Mercier, 1973) to represent the measured transverse force, defining a different lift coefficient for each term in the series. These lift coefficients are reproduced in Fig. 2.13 but will be discussed in the following section on waves. They did not calculate the phase angles associated with the different harmonics. However, they advised the use of a random phase angle to calculate the transverse force. Their results also show that the dominant frequencies of vortex-shedding are dependent on  $KC$  and cluster around the driving frequency for the lower values of  $KC$ . As  $KC$  increases, the frequencies cluster around a value twice the driving frequency but became less organized at higher  $KC$ . The trend continued but the basic assumption of clustering to one of the multiples of the driving frequency seemed to break down. The author was unable to find any published data on vortex span-wise coherence length for this flow category. Likewise, no information was found on the effect of transverse motion on transverse force and vortex span-wise coherence length.

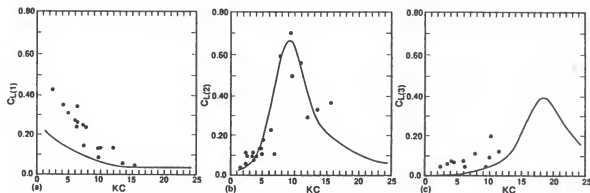


Figure 2.13: Lift coefficient harmonics versus Keulegan-Carpenter number,  $KC$ , — curve fit of data from harmonically oscillated articulated cylinder in still water, • data from waves impinging on a smooth, fixed vertical cylinder (Refs. 12, 13).

## 2.5 Wave Flows

Flows generated by regular, unidirectional surface waves impinging on fixed vertical cylinders are discussed separately due to the three dimensionality of the particle motion and its potential effects on the transverse force. Several researchers (Bearman *et al.*, 1985; Bearman, 1988b; Bidde, 1971; Chakrabarti *et al.*, 1976, 1983; Chakrabarti and Cotter, 1984; Isaacson and Maull, 1976, 1977; Sawaragi *et al.*, 1976, 1977; Tørum and Reed, 1982) have conducted experiments with regular waves and have reported lift coefficient data as a function of  $KC$ . Others (e.g. Maull and Kaye, 1988) have observed the effect of transverse motion on the in-line motion and transverse forces in regular waves. Random waves have also been investigated (see Bearman *et al.*, 1985; Graham, 1987).

Chakrabarti *et al.* (1976) measured vortex-induced transverse forces on local sections of a fixed vertical cylinder (same articulated cylinder they oscillated in still water) in regular waves. They used the same series technique as outlined in the previous section to obtain the lift coefficients. Data reported for the first three harmonics of lift coefficient are plotted in Fig. 2.13 along with curves representing (i.e. polynomial curve fits) data for the articulated tower discussed above under oscillatory,

nonplanar flows. Note that  $C_{L(1)}$  and  $C_{L(3)}$  from the articulated tower experiments are lower than the corresponding values for waves while  $C_{L(2)}$ , which is the larger of the coefficients, is about the same for waves and the oscillated articulated tower. More data and comparisons are needed before conclusions can be drawn for this flow situation.

The experiments performed in this category (wave flows) covered a wide range of apparatus sizes ranging from the 25 mm (1 in) diameter, 51 mm (0.167 ft) long cylinder (used by Sawaragi *et al.*, 1976) to the 0.5 m (19.7 in) diameter, 10 m (32.8 ft) long cylinder (Bearman, 1988b). Since the transverse force was found to exhibit some degree of irregularity, many of the investigators presented their data in terms of an *rms* lift coefficient. As in the case of planar flows discussed above there are differences in  $C_{L_{rms}}$  used by the different investigators. Once again the author compiled available data for  $C_{L_{rms}}$  and plotted them versus  $KC$  (see Fig. 2.14). Those for Bidde (1971) were not included since they are defined in terms of  $C_{L_{max}}$ . In this figure, Bearman's data are based on an *rms* velocity from measurements near the location of his instrumented segment. It is not clear what definition was used by Isaacson and Maull (1976) but the author assumed it to be based on the maximum value of the velocity at the instrumented segment as computed using linear wave theory. Sawaragi *et al.* (1976) did not define their  $C_{L_{rms}}$  but since they compared their results with Isaacson and Maull the same assumption made for Isaacson and Maull was applied to them. As would be expected there is more scatter in these data than for the less complex flows. This is particularly true for the data of Sawaragi *et al.* for larger values of  $KC$  and  $kh$  between 1.2 and 2.4. Possible reasons for such scatter include the large differences in model sizes, differences in  $H/D$ , and differences in ellipticity of the particle motion (Bearman *et al.*, 1985 found this was not a factor for the conditions of their experiments). However, it is interesting to note that the lift coefficient is a maximum at about the same  $KC$  values as for oscillatory, planar flow ( $KC$  between 10 and 12).

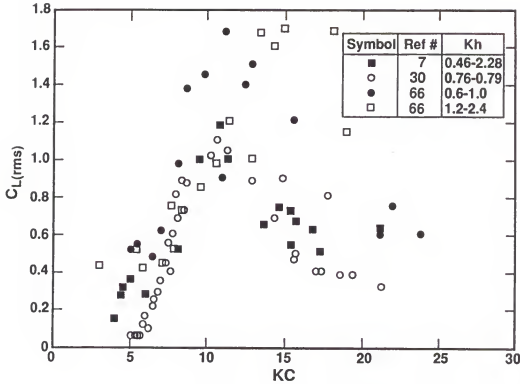


Figure 2.14: Lift coefficient versus Keulegan-Carpenter number for regular waves around a smooth, fixed vertical cylinder.

Some flow visualization tests have also been conducted in this flow category to study the vortex-shedding process and its frequency. Bearman (1988b), Isaacson and Maull (1976) and Sawargi *et al.* (1976) carried out visualization tests to characterize the frequency of the vortex-shedding process. However, due to the subjectivity in the visualization techniques the behavior of vortex-shedding frequency is examined from the transverse force power spectra. The spectra obtained by Chakrabarti *et al.* (1976) and by Tørum and Reed (1982) were thus compiled and plotted in Fig 2.15. From these spectra, one can see the existence of multiple frequencies at all values of  $KC$ , but the dominant frequencies have the same trend as in oscillatory, planar flows. That is, at lower values of  $KC$  the dominant frequencies cluster around the wave frequency. As  $KC$  increases to  $\approx 9$  the frequencies cluster at twice the wave frequency, then at three times the wave frequency as  $KC$  increases further, etc.

The author was unable to find reported data on span-wise coherence length or transverse motion for this flow category (waves). However, as mentioned before, some investigators allowed transverse motion in their studies. These investigators were mainly concerned with determining the conditions under which transverse motion can be excited since this motion can cause shut-down of operations and fatigue of structural members (such as marine risers). In an attempt to quantify such conditions, the maximum values of  $y_{rms}/D$  (defined as  $Y_{rms}/D$ ) from several investigators' data were plotted versus several of the pertinent parameters. A plot of  $Y_{rms}/D$  versus  $V_r$  (see Fig. 2.16) was found to be a meaningful. This plot shows that the maximum values of the response ( $Y_{rms}/D$ ) for different flow conditions fell in a relatively narrow range of reduced velocity,  $V_r$ .

In summary, the existing data on the vortex-induced transverse loading and response for fixed and transversely unconstrained, smooth, cylinders were reviewed for the different flow situations. As a result of this review one can say there have been significant advances in the understanding of vortex-induced forces on bluff bodies for some types of flow, especially steady and oscillatory, planar flows. In spite of these advances, however, more work is needed before the effects of many of the flow and geometric parameters on the transverse force and response can be quantified for the design engineer. Lack of consistency in data reporting has hindered progress in some areas while the difficulty of measuring some of the important quantities (such as, span-wise coherence length of vortices) has limited the data available for analysis. With an increasing awareness of the problems associated with inconsistent data reporting and with rapid advances in instrumentation technology, hopefully, these problems can be eliminated. This study focuses on the effects of flow nonuniformity and transverse motion on vortex-induced transverse forces (in particular, lift coefficients and frequency of vortex-shedding) and on the vortex span-wise correlation length.

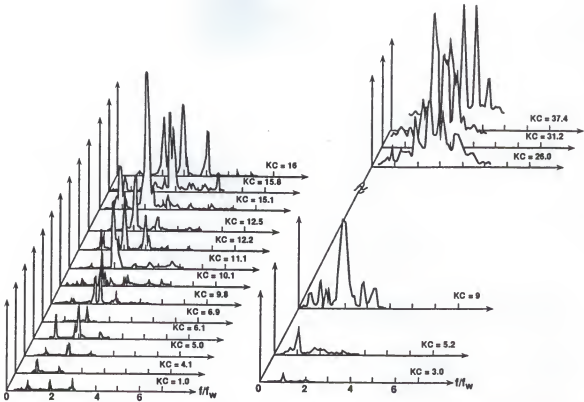


Figure 2.15: Schematic transverse force power spectra for regular waves around a smooth, fixed vertical cylinder for various Keulegan-Carpenter numbers,  $KC$  (Refs. 12, 73).

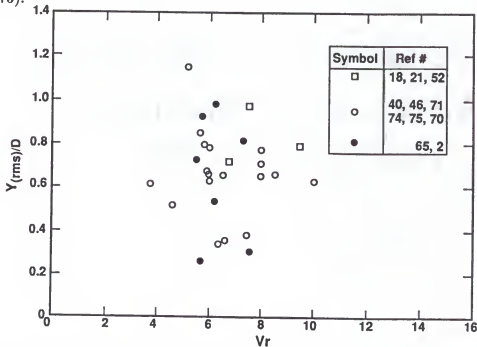


Figure 2.16: Maximum transverse response for various flow configurations (□ steady, planar flow), (○ oscillatory, planar flow), (● wave flows).



## CHAPTER 3 EXPERIMENTAL INVESTIGATIONS

### 3.1 Scaling Parameters and Model Selection

The modelling of fluid-induced dynamic forces exerted on bodies immersed in a viscous fluid has always presented difficulties with regard to similarity and scale. This is especially true when the structure is such that it is free to move. If dimensional analysis is applied to the particular problem of a transversely unconstrained bottom-hinged cylinder in nonuniform oscillatory fluid flow, the amplitude of transverse motion can be expressed in terms of the lift coefficient,  $C_L$ , reduced velocity,  $V_r$ , stability parameter,  $K_s$ , and added mass to cylinder mass ratio,  $m_a/m_s$ , (see Appendix A for details), i.e.,

$$y/D = Y(C_L, V_r, K_s, m_a/m_s) \quad (3.1)$$

where

$$C_L = C_L(R_e, KC, T_y). \quad (3.2)$$

If the cylinder is smooth and the external generated turbulence " $T_y$ " in the flow is small, Eqn. 3.2 reduces to

$$C_L = C_L(R_e, KC). \quad (3.3)$$

Consequently, Eqn. 3.1 reduces to

$$y/D = Y(R_e, KC, V_r, K_s, m_a/m_s). \quad (3.4)$$

For complete similarity the values of all the parameters should be the same for both model and prototype, i.e.,

$$R_e = \left(\frac{UD}{\nu}\right)_m = \left(\frac{UD}{\nu}\right)_p,$$

$$KC = \left(\frac{UT}{D}\right)_m = \left(\frac{UT}{D}\right)_p,$$

$$V_r = \left(\frac{U}{f_n D}\right)_m = \left(\frac{U}{f_n D}\right)_p,$$

$$\left(\frac{m_s \delta}{\rho D^2}\right)_m = \left(\frac{m_s \delta}{\rho D^2}\right)_p \quad \text{and}$$

$$\left(\frac{m_a}{m_s}\right)_m = \left(\frac{m_a}{m_s}\right)_p$$

where  $m$  and  $p$  refer to model and prototype, respectively.

Of these similarity groups the most important parameters are the Reynolds number ( $R_e$ ), Keulegan-Carpenter number ( $KC$ ) and reduced velocity ( $V_r$ ). Hydrodynamic force coefficients for large values of  $R_e$  are needed in full-sized offshore structures applications. These conditions are difficult if not impossible to produce in laboratory experiments. Wave tank testing generally produces Reynolds numbers (based on structure diameter) up to approximately  $5 \times 10^4$ , whereas most prototype structures experience Reynolds numbers well beyond  $10^5$ , i.e., in the upper subcritical, critical and supercritical regions (according to steady flow principal Reynolds number flow regimes around smooth cylinders). Wave tank testing has also the additional problem of not being able to precisely control Reynolds number. Ideally both Reynolds number and reduced velocity must be scaled. It is practically impossible to achieve both a desired Reynolds number and reduced velocity at the same time unless a full scale structure is tested.

For an average prototype articulated tower, such as the "ELF" loading tower operating in the North Sea, (diameter = 4.5 m, length = 150 m and water depth = 135 m), the reduced velocity,  $V_r$  varies between 0 and 12 for a current velocity varying between 0 and 2.5 knots. It can also be as high as 20 for a 100 year design wave (having a 17 sec. period and 30 m height according to Kirk and Jain, 1977).

In laboratory testing it is important to cover the range mentioned above for both prototype Reynolds number and reduced velocity. Using a constant diameter cylinder this can be done by adjusting either the natural frequency  $f_n$  or the velocity range or both. In the tests carried-out in this investigation the natural frequency was held approximately constant.

The intent of this investigation was to study the effect of flow nonuniformity and transverse motion on the vortex-induced transverse loading. In order to make the results of this study as useful as possible to the design of offshore structures, the model was designed to produce ranges of similarity parameters as close as possible to those experienced by prototype structures where vortex-induced loading is important. Other geometric parameters such as the length/diameter ratio ( $\ell/D$ ) should also fall within the prototype range. A survey of the available literature revealed that vortex-shedding is considerable in the following ranges of similarity parameters:  $3 \times 10^4 < R_e < 10^6$ ,  $5.0 < KC < 12.0$ ,  $1.0 < V_r < 20.0$  and  $\ell/D$  between 20 and 30.

The requirements for achieving similarity (i.e., equivalent values for model and prototype) for Reynolds number conflicts with the conditions required for similarity for reduced velocity and other parameters. For example, to produce high values of Reynolds number requires high values of flow velocity since  $\nu$  is fixed and the cylinder diameter is constrained by the ratio  $\ell/D$ . To satisfy reduced velocity similarity the higher flow velocities imposed by Reynolds number similarity require high system natural frequency which means a very light structure which is limited by required rigidity. Also higher flow velocities means higher amplitudes of oscillation or higher driving frequencies which are constrained by the available driving mechanisms. Due to these complications, the design of the cylindrical model used in these experiments was accomplished with the aid of a computer program that optimized the range of the parameters within the limitations imposed by the drive mechanism, tank, budget, etc. In other words, given the values of the facilities available such as maximum water

depth, maximum in-line velocity and others, the program selects the dimensions that cover ranges of the similarity parameters overlapping with those of prototypes. In this study, model dimensions of 0.1524 m diameter and 3.05 m length were selected, i.e, a ratio of  $\ell/D = 20$ . Such a model covered ranges of  $R_e$  between  $6.1 \times 10^3$  and  $1.3 \times 10^5$ ,  $KC$  between 2.5 and 9.5 and  $V_r$  between 3.15 and 46.

For an elastically-mounted cylinder, experiments should be carried-out at constant  $K_s$  to facilitate comparison of maximum response amplitudes for different conditions. In this investigation, despite the changes in temperature during the course of testing,  $K_s$  was approximately constant.

The ratio of the fluid added mass to the structural mass ( $m_a/m_s$ ) should be modelled properly. In air  $m_a/m_s = O(10^{-3})$  and thus is of little importance. In water, however, the ratio  $m_a/m_s = O(1)$  and affects both the maximum amplitude of motion due to vortex-shedding and the velocity range over which lock-in occurs.

### 3.2 Experimental Set-up

Very little information exists on the effect of flow nonuniformity and structure transverse motion on vortex-induced transverse loading and vortex span-wise coherence length. To investigate such effects two types of experiments were designed and performed. Both experiments were performed in a circular water tank with a rigid articulated tower model. In the first type of experiment the model was constrained from transverse motion while in the second type it was free to move in the transverse direction.

As discussed before in Chapter 2, there are two different ways to produce a relative oscillatory motion between a cylindrical model and the surrounding fluid. One method is to oscillate the fluid past a stationary cylinder while the other is to oscillate the cylinder past the stationary fluid. Kinematically there is no difference between the two situations when viewed from the appropriate reference frame. Experimentally, there are differences in implementation between the two methods.

In the experiments of this investigation, an articulated cylinder was oscillated in an otherwise still fluid. This approach was taken because it was relatively easy to implement and because it allowed more precise control over the parameters. It also allowed the fluid-induced forces to be determined more directly. In other words one can determine, after subtracting the inertial force due to the mass of the oscillating cylinder, the coefficient of added mass ( $C_m$ ) instead of the inertia coefficient ( $C_M$ , i.e.,  $1 + C_m$ ) since no horizontal pressure gradient exists in the flow field. On the other hand, this approach has certain disadvantages which must be overcome. These are: i) waves and free surface disturbances can be created by the oscillating cylinder, ii) the drive mechanism can transmit vibrations to the cylinder and surrounding fluid and iii) the inertia force due to the mass of the oscillating body has to be accounted for in the measured force signal.

In this experiment, several ideas and designs were employed to overcome these difficulties. Due to the tank to cylinder diameter ratio ( $= 60$ ) wall effects were negligible (in terms of a blockage ratio it was 1.6%). This is well below the 6.0% limit given by West and Apilt (1982) for no influence from blockage on the Strouhal number. Soft and porous packing materials were also placed at water surface half-way between the cylinder and the tank wall to absorb surface disturbances and reduce wave reflections from the wall (see Fig. 3.3). Two heavy steel I-beams were placed across the tank to support the linear driving motor. The feed back control system for the linear drive motor was initially a source of high frequency vibration, but this was minimized by using a lowpass analog filter in the feed back circuit.

The two types of experiments used in this study were designed to obtain the information needed to quantify the dependence of the vortex-shedding process, vortex span-wise coherence length and transverse force on the flow and structure parameters. All tests were performed in a deep circular water tank 9.15 m in diameter and 3.1 m high. The tower model was a right circular rigid aluminum cylinder with a diameter

of 0.1524 m, a thickness of 3.0 mm and a length of 3.05 m. It was instrumented with miniature, quick response, (2.15 mm diameter bead) thermistors embedded in its surface to measure the frequency of vortex shedding along the tower. These thermistors were located at the leading and trailing sides of the tower at 20 different locations (total of 10 thermistors along each side). All the wires of the thermistors were run through the inside of the tower. The signal processing circuits for the thermistors were mounted inside the cylinder near the top. The cylinder was attached to the bottom at the center of the tank through a low friction hinge designed to allow  $X$  and  $Y$  motion while constraining cylinder rotation about its axis. Its top was attached through a vertically sliding shaft to a linear drive electric motor mounted horizontally between the I-beams. The vertical sliding shaft was designed to account for the change in the vertical position of the top of the tower during its rotation about the bottom hinge. Ultra low friction linear ball bushings for the vertical sliding shaft were mounted in the upper end plate of the cylinder. An  $X - Y$  force transducer was inserted between the top of the tower and the table of the linear drive motor. To negate the need to measure forces at the base, a pin joint was placed between the tower and the  $X - Y$  force transducer at the top. Two Linear Displacement Transducers (LDT) were used to measure in-line and transverse displacements of the tower. The active strokes of the in-line and transverse LDT were 0.66 m and 0.46 m, respectively. All alignments were made prior to adding water to the tank.

In the first type of experiments, tests were performed with the configuration shown in Fig. 3.1. An in-line simple harmonic motion was imposed at the top of the tower while constraining the transverse motion. Quantities measured during these tests were i) in-line position, ii) in-line force, iii) transverse force and iv) vortex-shedding frequencies from the 20 thermistors mounted along the tower.

The second experiment type configuration shown in Fig. 3.2 used the same tower model with the exception of the mechanism that attaches the cylinder to the linear

drive motor. The tower was driven with the same in-line motion as in the first type experiment, but in this case it was allowed to respond freely in the transverse direction. Quantities measured in these tests included i) in-line position, ii) in-line force, iii) transverse motion and iv) vortex-shedding frequencies from the 20 different thermistors along the tower. The water depth for all the tests (type I and II) was 2.65 m. Photographs of the general setup and transverse motion mechanism are shown in Fig. 3.3.

### 3.3 Instrumentation and Calibration

As discussed in the previous section, the following quantities were measured

1. In-line tower position.
2. In-line force.
3. Transverse force (type I experiment only).
4. Transverse response (type II experiment only).
5. Thermistor signals.

Other signals such as the input driving frequency were measured and held constant during each test. Quantities such as water temperature and surface wave activity were also monitored.

A block diagram of the measurement system used is shown in Fig. 3.4. The instrumentation used to measure these quantities are listed below. The calibration procedures used, where needed, are also discussed.

#### 3.3.1 Frequency Generator

The sinusoidal motion imposed at the top of the tower was generated using a Hewlett Packard (HP) frequency generator. A Hewlett Packard (HP) frequency counter in parallel with the frequency generator was also used to continuously monitor the input driving frequency ( $f_d$ ) during each run.

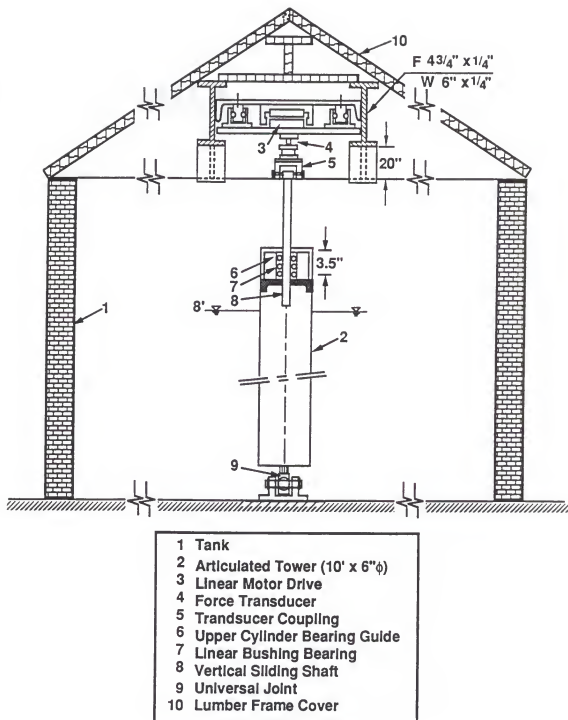


Figure 3.1: Schematic diagram of transversely constrained experiment set-up.



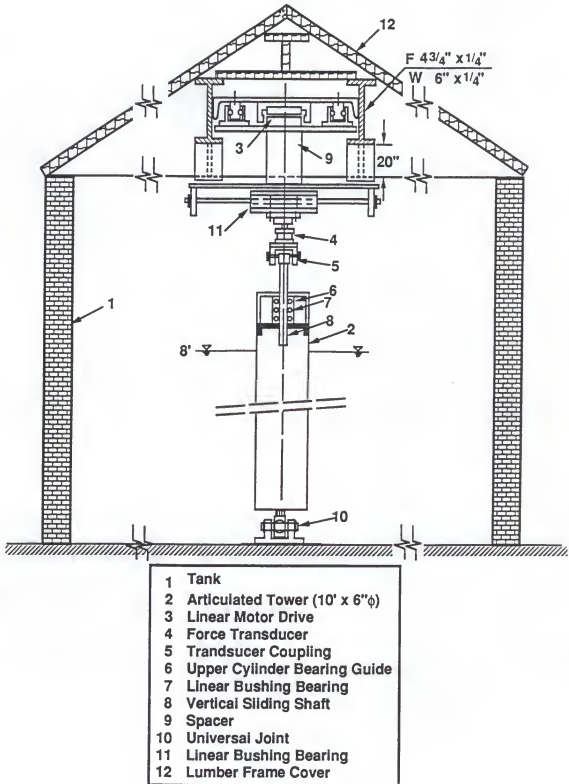


Figure 3.2: Schematic diagram of transversely unconstrained experiment set-up.



Figure 3.3: Photographs of experimental set-up.

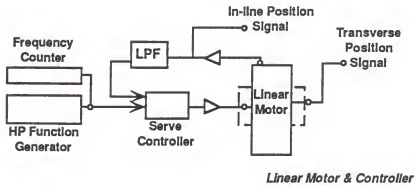
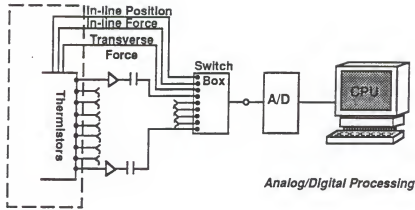


Figure 3.4: Block diagram of measurement system.

### 3.3.2 Force Transducers

Due to the high cost of commercial  $X - Y$  (horizontal components) load cells, the one used in these experiments was designed, constructed and tested in the department laboratory. The transducer was a beam-type load cell (see Appendix B, Fig. B.1) made of 304 stainless steel with overall dimensions  $3.8 \times 3.8 \times 7.5$  cm. It was constructed as if two I-beam were placed flange-to-flange so that their webs make a "90°" angle. The thickness of each web which was required to withstand the maximum loads anticipated in its direction was calculated using Hooke's law, with a safety factor of 1.5. With the scantlings selected, the transducer had a resolution of 0.2 N in each direction. Each web was instrumented with four (two on each side) active 350 ohm strain gages (with a gage factor of  $2.03 \pm 1\%$ ). These gages formed the

elements in a standard four-arm wheatstone bridge circuit and provided both high sensitivity and temperature compensation. The strain gage bridge was connected to a strain gage amplifier, the Omega DMD 465 (see Appendix B, Fig. B.2 and Table B.1 for schematic and specifications). A pulley system was developed to calibrate each channel of the transducer. The calibration was carried out by varying the loads on one channel in both directions (i.e., in tension and compression). Loads were added in increments then removed in increments to test for hysteresis. At the same time a constant load was maintained on the other channel to examine the side load effect. This was repeated for different constant side loads. The calibration curves are shown in Appendix B, Figs. B.3, to B.5. Note that the two channels are very well isolated (i.e., loads in one direction have minimum influence on the transducer output in the other direction).

### 3.3.3 Linear Displacement Transducers

The tower's in-line and transverse motions were measured using two, MTS Temposonics II, LDT (Linear Displacement Transducers) systems with AOM (Analog Output Modules), see Appendix B, Fig. B.6 for a schematic setup and Table B-2 for the specifications of the AOM. Both LDTs were calibrated by giving the tower known displacements measured with a rule while the output from the A/D data acquisition board was recorded. A statistical analysis (average and standard deviation) of the recorded calibration data at each position was then carried-out. This procedure was repeated for the different positions around the vertical position of the tower i.e., in the positive and negative directions. The resultant data gave straight line calibration curves for each transducer, as shown in Appendix B, Fig. B.7 and Fig. B.8.

### 3.3.4 Thermistors

The vortex shedding frequencies were measured by using miniature, quick response, thermistors embedded in the surface of the tower. Dimensions, thermal and electrical properties of these thermistors are given in Appendix B, Table B-3. The

principal is similar to that of a hot film anemometer. That is, the overheated thermistor is cooled by the flow of the fluid past its 2.15 mm diameter bead which in turn reduces its electrical resistance. The circuit designed for processing the signals of these thermistors is given in Appendix B, Fig. B.9. The concept of using thermistors to measure frequency of vortex-shedding was tested using a thermistor embedded in a 0.065 m diameter and 0.61 m long PVC cylinder. The cylinder was then placed in a steady flow on a flow visualization table as shown in Appendix B, Fig. B.10. Three different flow velocities with Reynolds numbers of  $4.6 \times 10^3$ ,  $9.7 \times 10^4$  and  $5 \times 10^4$  were used. The thermistor output signals were sampled at 50 Hz and a spectral analysis performed on each signal. The spectra of the signals (see Appendix B, Fig. B.11) showed a single large spike (relative to other frequency components in the spectrum). The Strouhal number,  $S_t$  at these spikes was found to equal 0.23, 0.188 and 0.123, respectively for the Reynolds numbers above.

### 3.3.5 Lowpass Filters

Analog filters must always be used with caution since they can produce undesirable as well as desirable effects. The undesirable effects are in the form of signal phase shift and amplitude attenuation. To minimize these effects, a second order, Butterworth, lowpass filter was designed for the in-line position signal to reduce the noise in the signal to the servo controller. The cut-off frequency was carefully selected for the filter after considering the useful driving frequency range. Since the highest driving frequency was 1.0 Hz, a cut-off frequency of 3.0 Hz for the feed back loop filter was deemed sufficiently high. A schematic diagram of this filter is shown in Appendix B, Fig. B.12. Two other lowpass filters were used for the in-line and transverse forces. Their cut-off frequencies were selected after examination of the unfiltered signals from exploratory runs for all the proposed driving frequencies. Spectral analyses were then performed on the measured signals. The results of these spectra showed no strong frequency components (even for the highest driving frequency, 1.0 Hz) above 15.0 Hz

for the in-line and 20.0 Hz for the transverse force signals. Accordingly 17.0 Hz and 22.0 Hz cut-off frequencies for the in-line force and transverse force signals were selected. A sample output of the transverse force time series and its power spectrum before and after filtering is given in Appendix B, Fig. B.13.

Other more standard instruments used in these experiments included: A Normag DC-linear drive motor (specifications given in Appendix B, Table B.4); DC-servo controller (Moog, Model 82 – 300); glass bulb mercury thermometer and a 12-bit, multi-function, high speed A/D Metrabyte/Asyst/DAC expansion board with analog input accuracy of 0.01% and a variable input voltage range. This board was installed in an IBM compatible personal computer.

### 3.4 Data Reduction

As mentioned before, two types of experiments were performed. Type I was with the transverse motion constrained and type II was with a cylinder free to move in the transverse direction.

Tests were run for different values of in-line amplitude and driving frequency. In the first type experiment, the cylinder driving frequency ( $f_d$ ) was varied from 0.4 Hz to 1.0 Hz. At most frequencies the amplitude of oscillation varied from 0.1 m to 0.28 m. A total of 86 runs were made during this experiment. Of these 8 runs were performed to test the repeatability. In each run, in-line and transverse forces, in-line position and the signals from the 10 thermistors were recorded. During the test runs GLOBALAB software was used to perform preliminary analysis of the measured data. The tower driving frequency ( $f_d$ ) and amplitude ( $a$ ) were also monitored during each run using a frequency counter and oscilloscope.

In the type II experiment, where transverse motion was allowed, the driving frequency ( $f_d$ ) was varied from 0.15 Hz to 0.8 Hz. At each frequency the amplitude was varied from 0.076 m to 0.28 m. A total of 190 runs, including 36 runs to test repeatability, were made during this experiment. In each run the in-line force, in-line

and transverse position and the thermistor signals were measured and recorded. To reduce the scatter in the measured data of in-line force and transverse motion some longer test runs, where only in-line force, transverse motion and the signal of vortex shedding from the top thermistor, were made.

Since the Direct Memory Access (DMA) page registers cannot be incremented by the controller, the maximum data area available (64K, a page, for 32,767 conversions) was used to acquire data for each run. This resulted in a duration of 63 sec for each recorded signal in the first type experiment where 13 data channels were acquired and 91 sec (273) sec for the second type experiment when 9 or (3) channels were used.

The maximum obtainable in-line amplitude was found to vary with the driving frequency ( $f_d$ ). The intent was to obtain as wide a range of Keulegan-Carpenter ( $KC$ ) and Reynolds ( $R_e$ ) numbers as possible. The range covered by these parameters and others during both experiments together with a summary of the test conditions are shown in Table 3.1. The natural frequency ( $f_n$ ) and damping ratio ( $\xi$ ) included in Table 3.1 were obtained by measuring the frequency of free oscillation in still water. The measured value of ( $f_n$ ) compared well with the analytical value obtained from the free vibration response predicted by a computer program developed by Omar and Sheppard (1991) for predicting response of articulated towers under the action of wind, current and waves.

Table 3.1: Test conditions for experiments I and II.

Item	Exp. I	Exp. II
minimum $f_d$	0.5 Hz	0.15 Hz
maximum $f_d$	1.0 Hz	0.8 Hz
minimum $a$	0.085 m	0.08 m
maximum $a$	0.283 m	0.29 m
temp. range	$83 - 88^\circ F$	$60 - 74^\circ F$
minimum $R_e$	$6.1 \times 10^3$	$8.4 \times 10^3$
maximum $R_e$	$2.15 \times 10^4$	$1.3 \times 10^5$
minimum $KC$	2.6	2.4
maximum $KC$	8.65	9.35
minimum $\beta$	1792	3151
maximum $\beta$	3692	18336
minimum $V_r$		2.66
maximum $V_r$		36.10
$f_n$		0.15 Hz
$\xi$		0.12
water depth	2.625 m	2.625 m
No. of channels	13 or 14	3 or 9
sampling frequency	40 Hz	40 Hz



## CHAPTER 4 MATHEMATICAL MODELS

### 4.1 In-line Force

The following equation of motion was used to reduce the in-line force data:

$$I_m \ddot{\theta}(t) = \sum M_{\text{total}} = M_g + M_D + M_{fz}, \quad (4.1)$$

where

- $I_m$  =  $I_o + I'_a$
- = total mass moment of inertia about the bottom hinge,
- $I_o$  = cylinder mass moment of inertia,
- $I'_a$  = added mass moment of inertia,
- $M_{\text{total}}$  = total moment about bottom hinge,
- $M_g$  = moment due to tower weight and buoyancy,
- $M_D$  = moment due to drag,
- $M_{fz}$  = moment due to linear drive motor and
- $\theta(t)$  = in-line deflection angle.

For the tower shown in Fig. 4.1 the moments  $M_g$ ,  $M_D$  and  $M_{fz}$  are given by

$$M_g = \left( \sum_{i=1}^n w_i r_i - \int_0^{d_1/\cos\theta} \rho_w A_c g r dr \right) \sin\theta, \quad (4.2)$$

$$M_D = -\frac{1}{2} \rho_w D C_D \int_0^{d_1/\cos\theta} (r \dot{\theta}) |r \dot{\theta}| r dr \text{ and} \quad (4.3)$$

$$M_{fz} = R L, \quad (4.4)$$

where  $A_c = \pi D^2/4$  is the cross sectional area of the tower element. The added mass moment of inertia,  $I'_a$  can be expressed as

$$I'_a = \int_0^{d_1/\cos\theta} I_a dr = \int_0^{d_1/\cos\theta} \frac{\pi}{4} \rho_w C_m D^2 r^2 dr. \quad (4.5)$$

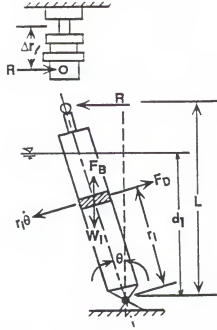


Figure 4.1: Definition sketch for the articulated tower showing in-line motion.

The motion of the tower was imposed by a horizontal linear drive motor mounted directly above the tower as shown in Fig. 4.1. The position of the moving table of the motor and thus the upper end of the shaft connected to the tower was monitored by a LDT (Linear Displacement Transducer). Due to the relatively small angular movement of the tower, the arc  $L\theta(t)$  can be approximated by the measured horizontal linear displacement  $X_m(t)$ . Substituting Eqns. 4.2 – 4.5 into Eqn. 4.1 and replacing  $L\theta$  by  $X_m$  results in

$$\begin{aligned}
 & -\left(\frac{I_o}{L} + \frac{\pi}{12}\rho_w D^2 \frac{d_1^3}{L \cos^3[X_m(t)/L]} C_m\right) \ddot{X}_m(t) - \\
 & \frac{1}{8}\rho_w D \frac{d_1^4}{L^2 \cos^4[X_m(t)/L]} C_D \dot{X}_m(t) |\dot{X}_m(t)| \\
 & + \left(\sum_{i=1}^n w_i r_i - \frac{\pi}{8}\rho_w g D^2 \frac{d_1^2}{\cos^2[X_m(t)/L]}\right) \sin[X_m(t)/L] = R L. \quad (4.6)
 \end{aligned}$$

Since the measured in-line moment  $M_m(t) = R \Delta r_\ell$ ,  $R = M_m(t)/\Delta r_\ell$ . Substituting this expression for  $R$  into Eqn 4.6 and rearranging results in

$$\begin{aligned}
& M_m(t) L / \Delta r_\ell + \frac{I_o}{L} \ddot{X}_m(t) - \\
& \left( \sum_{i=1}^n w_i r_i - \frac{\pi}{8} \rho_w g D^2 \frac{d_1^2}{\cos^2[X_m(t)/L]} \right) \sin[X_m(t)/L] = \\
& - \frac{\pi}{12} \rho_w D^2 \frac{d_1^3}{L \cos^3[X_m(t)/L]} C_m \ddot{X}_m(t) - \\
& \frac{1}{8} \rho_w D \frac{d_1^4}{L^2 \cos^4[X_m(t)/L]} C_D \dot{X}_m(t) |\dot{X}_m(t)|. \quad (4.7)
\end{aligned}$$

The quantities on the left hand side in Eqn. 4.7,  $M_m(t)$ ,  $\ddot{X}_m(t)$  and  $X_m(t)$  are known from the measured values. The in-line motion  $X_m(t)$  was monitored by the LDT and found to conform with the input signal,  $a \sin \omega_d t$ , where, "a" is the amplitude of oscillation and  $\omega_d$  the oscillation circular frequency. Thereupon, the velocity  $\dot{X}_m(t)$  and acceleration  $\ddot{X}_m(t)$  were computed from the time derivatives of  $X_m(t) = a \sin \omega_d t$ .

Equation 4.7 can be written as

$$f_m(t) = f_I(t) C_m + f_D(t) C_D, \quad (4.8)$$

where

$$\begin{aligned}
f_m(t) &= \frac{M_m(t)L}{\Delta r_L} + \frac{I_o}{L} \ddot{X}_m(t) - \left( \sum_{i=1}^n w_i r_i - \frac{\pi}{8} \rho_w g D^2 \frac{d_1^2}{\cos^2[X_m(t)/L]} \right) \sin[X_m(t)/L], \\
f_I(t) &= - \frac{\pi}{12} \rho_w D^2 \frac{d_1^3}{L \cos^3[X_m(t)/L]} \ddot{X}_m(t) \text{ and} \\
f_D(t) &= - \frac{1}{8} \rho_w D \frac{d_1^4}{L^2 \cos^4[X_m(t)/L]} \dot{X}_m(t) |\dot{X}_m(t)|.
\end{aligned}$$

$C_D$  and  $C_m$  are the unknown quantities in Eqn. 4.8 and can be obtained by minimizing the squares of the differences between the computed and measured values, i.e., by minimizing  $\bar{\delta}_i^2$  where

$$\bar{\delta}_i^2 = \frac{1}{N} \sum_i^N [f_I(t_i) C_m + f_D(t_i) C_D - f_m(t_i)]^2. \quad (4.9)$$

$N$  is the number of data points in one cycle. From this equation the minimum  $C_D$  and  $C_m$  were obtained by solving the two simultaneous equations

$$\frac{\partial \bar{\delta}_i^2}{\partial C_D} = 0 \text{ and} \quad (4.10)$$

$$\frac{\partial \bar{\delta}_i^2}{\partial C_m} = 0. \quad (4.11)$$

Equation 4.10 and Eqn. 4.11 can be written in a matrix form as

$$\begin{bmatrix} \sum_{i=1}^N f_D^2(t_i) & \sum_{i=1}^N f_I(t_i)f_D(t_i) \\ \sum_{i=1}^N f_I(t_i)f_D(t_i) & \sum_{i=1}^N f_I^2(t_i) \end{bmatrix} \begin{Bmatrix} C_D \\ C_m \end{Bmatrix} = \begin{Bmatrix} \sum_{i=1}^N f_m(t_i)f_D(t_i) \\ \sum_{i=1}^N f_m(t_i)f_I(t_i) \end{Bmatrix}. \quad (4.12)$$

The solution of Eqns. 4.12 results in the following equations for  $C_D$  and  $C_m$

$$C_D = \frac{\sum[f_m(t_i)f_D(t_i)]\sum f_I^2(t_i) - \sum[f_m(t_i)f_I(t_i)]\sum[f_D(t_i)f_I(t_i)]}{\sum[f_I^2(t_i)]\sum[f_D^2(t_i)] - [\sum f_D(t_i)f_I(t_i)]^2} \text{ and} \quad (4.13)$$

$$C_m = \frac{\sum[f_m(t_i)f_I(t_i)]\sum f_D^2(t_i) - \sum[f_m(t_i)f_D(t_i)]\sum[f_D(t_i)f_I(t_i)]}{\sum[f_I^2(t_i)]\sum[f_D^2(t_i)] - [\sum f_D(t_i)f_I(t_i)]^2}. \quad (4.14)$$

where the summations are evaluated from  $i = 1$  to  $N$  for each cycle. To put more emphasis on the large data values and thus further reduce the differences between the measured and predicted forces in the neighborhood of maximum forces, the weighted least squares technique was also applied using  $f_m^2(t_i)$  as a weighing factor. The suitability of the in-line force data for determining  $C_D$  and  $C_m$  was also evaluated using Dean's (1976) approach. In this approach, the mean square error  $\bar{\delta}_i^2$  given by Eqn. 4.9 defines a quadratic "error surface" which is a minimum at the  $C_D$  and  $C_m$  obtained by solving Eqn 4.12. The suitability of the data can then be evaluated from the lines of constant error values,  $\bar{\delta}_i^2(C_D, C_m)$ , which are ellipses. For example, the steeper the slope of the error surface with  $C_D$ , the better the data are suited for evaluating the drag coefficient, see Fig. 4.2.

$C_D$  and  $C_m$  are time averages over several cycles. This study did not deal with the instantaneous values of these coefficients. However, since the measurement errors in the data must introduce some uncertainty, the variance and covariance of the

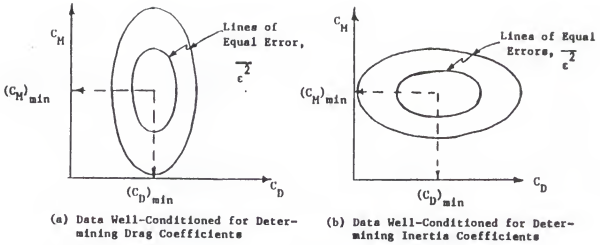


Figure 4.2: Contour lines defining Error surfaces for the in-line force (Ref. 15).

estimates ( $C_D$  and  $C_m$ ) were computed. The variance,  $\sigma_f^2$ , in the value of any function can be written as

$$\sigma_f^2 = \sum_{i=1}^N \left( \frac{\partial f}{\partial y_i} \right)^2. \quad (4.15)$$

For estimating the uncertainties in  $C_D$  and  $C_m$ , Eqn. 4.12 can be rewritten as

$$[\alpha]\{a\} = \{\beta\} \quad (4.16)$$

or

$$\sum_{j=1}^2 \alpha_{kj} a_j = \beta_k, \quad (4.17)$$

where

$[\alpha]$  =  $2 \times 2$  matrix, or

$$\alpha_{kj} = \sum_{i=1}^N X_j(t_i) X_k(t_i), \quad k = 1, 2 \text{ and } j = 1, 2 \text{ and}$$

$\{\beta\}$  = a vector of length 2, or

$$\beta_k = \sum_{i=1}^N f_m(t_i) X_k(t_i) \quad k = 1, 2.$$

The inverse matrix  $C_{jk} \equiv [\alpha]_{jk}^{-1}$  is closely related to the probable (or more precisely, the standard) uncertainties of the estimated parameters  $a_j \equiv (C_D, C_m)$ . The

solution to Eqn. 4.12 (or equivalently Eqn. 4.16) is

$$a_j = \sum_{k=1}^2 [\alpha]_{jk}^{-1} \beta_k = \sum_{k=1}^2 C_{jk} \left[ \sum_{i=1}^N f_m(t_i) X_k(t_i) \right]. \quad (4.18)$$

Note that  $a_j$  corresponds to  $f$  and  $f_m(t_i)$  to  $y$ , in Eqn. 4.15 thus

$$\frac{\partial f}{\partial y_i} = \frac{\partial a_j}{\partial f_m(t_i)} = \sum_{k=1}^2 C_{jk} X_k(t_i). \quad (4.19)$$

Consequently, the variance associated with the estimate parameters  $a_j$  is

$$\sigma^2(a_j) = \sum_{k=1}^2 \sum_{\ell=1}^2 C_{jk} C_{j\ell} \left[ \sum_{i=1}^N X_k(t_i) X_\ell(t_i) \right]. \quad (4.20)$$

The final term in the square brackets is just the matrix  $[C]$ . Since this is the matrix inverse of  $[C]$ , Eqn. 4.20 reduces to

$$\sigma^2(a_j) = C_{jj}. \quad (4.21)$$

In other words, the diagonal elements of  $[C]$  are the variances of  $C_D$  and  $C_m$ , while the off-diagonal elements  $C_{jk}$  are the covariances between  $C_D$  and  $C_m$  (i.e.,  $COV(C_D, C_m)$ ).

An estimate of the goodness-of-fit of the data to the model is still needed. A simple measure of the goodness-of-fit defined as the average percentage error between the measured and predicted signals ( $f_m(t_i)$  and  $f_p(t_i)$ ) was used. This was defined as

$$ERR = 100 \sqrt{\frac{\sum [f_m(t_i) - f_p(t_i)]^2}{\sum f_m^2(t_i)}} \% \quad (4.22)$$

where the summation is evaluated for  $i = 1, 2, \dots, N$ .

### Drag Force

$C_D$ , for most situations, has been found to depend on Reynolds number, and thus on the velocity. In an attempt to minimize this dependence and maintain the drag coefficient constant, an investigation of the power to which the velocity must be raised in the drag force equation was made. The drag moment in Eqn. 4.3 was replaced by the following expression

$$M_D = -\frac{1}{2} \rho_w D C_D \int_0^{d_1/\cos\theta} (r\dot{\theta})^n \operatorname{sgn}(r\dot{\theta}) r dr, \quad (4.23)$$

where  $\dot{C}_D$  is the drag coefficient associated with this expression and "sgn" is a sign function equal to  $\pm 1$  depending on the sign of the argument,  $r\dot{\theta}$ . Making the same assumption  $X_m(t) \simeq L\theta(t)$  and carrying out the integration of Eqn. 4.23, the equation of motion (Eqn. 4.7) reduces to

$$\begin{aligned} M_m(t) \frac{L}{\Delta r_t} + \frac{I_o}{L} \ddot{X}_m(t) - \\ \left( \sum_{i=1}^m w_i r_i - \frac{\pi}{8} \rho_w g D^2 \frac{d_1^2}{\cos^2[X_m(t)/L]} \right) \sin[X_m(t)/L] = \\ - \frac{\pi}{12} \rho_w D^2 \frac{d_1^3}{L \cos^3[X_m(t)/L]} C_m \ddot{X}_m(t) - \\ \frac{1}{2} \rho_w D \left[ \frac{d_1}{\cos[X_m(t)/L]} \right]^{n+2} \left[ \frac{\dot{C}_D}{n+2} \right] \left| \frac{\dot{X}_m(t)}{L^2} \right|^n \text{sgn}[\dot{X}_m(t)]. \end{aligned} \quad (4.24)$$

In this equation, the quantities on the left hand side,  $M_m(t)$ ,  $\ddot{X}_m(t)$  and  $X_m(t)$  are known from the measurements. Using  $f_m(t)$  and  $f_I(t)$  defined before, and defining

$$\begin{aligned} f_{dr} &= -\frac{1}{2} \rho_w D \text{sgn}[\dot{X}_m(t)], \\ C(t) &= \left[ \frac{d_1}{\cos[X_m(t)/L]} \right] \text{ and} \\ D(t) &= \left| \frac{\dot{X}_m(t)}{L^2} \right|, \end{aligned}$$

Equation 4.24 reduces to

$$f_m(t) = f_I(t) C_m + f_{dr} [C(t)]^{n+2} [D(t)]^n \dot{C}_D / (n+2). \quad (4.25)$$

The unknown quantities in this equation are  $C_m$ ,  $\dot{C}_D$  and  $n$  which can also be obtained by using the least squares equation:

$$\bar{\delta}_1^2 = \frac{1}{N} \sum_i^N [f_I(t_i) C_m + f_{dr} [C(t_i)]^{n+2} [D(t_i)]^n \dot{C}_D / (n+2) - f_m(t_i)]^2 \quad (4.26)$$

or the weighted least squares equation

$$\bar{\delta}_1^2 = \frac{1}{N} \sum_i^N f_m^2(t_i) [f_I(t_i) C_m + f_{dr} [C(t_i)]^{n+2} [D(t_i)]^n \dot{C}_D / (n+2) - f_m(t_i)]^2. \quad (4.27)$$

The minimum  $C_m$ ,  $\dot{C}_D$  and  $n$  were then obtained by solving the coupled nonlinear system of equations given by

$$\frac{\partial \bar{\delta}_1^2}{\partial C_m} = 0, \quad (4.28)$$

$$\frac{\partial \bar{\delta}_1^2}{\partial \dot{C}_D} = 0 \text{ and} \quad (4.29)$$

$$\frac{\partial \bar{\delta}_1^2}{\partial n} = 0. \quad (4.30)$$

The Newton-Raphson method for nonlinear systems of equations was applied to solve this set of equations (Eqns. 4.28 to 4.30). The method is given in many text books (e.g. Press *et al.*, 1988).

#### 4.2 Transverse Force

For several reasons the transverse force has been the subject of greatest interest in this study. First, its amplitude can, under certain conditions, be as large as that of the in-line force. Second, the transverse force can give rise to fluid-induced oscillations and to fatigue failure. Third, even small transverse motions of the body regularize the wake motion, alter the span-wise correlation of the vortices, and drastically change the magnitude of both the in-line and transverse forces.

With all the information available on vortex-shedding, there is no simple, explicit formula to predict the time variation of the vortex-induced transverse force. This is because of its dependency on the type of flow and structure motion. In most types of flows it also exhibits some degree of irregularity that is usually due to the alternating eddies behind the structure. Therefore, most formulations of transverse forces are semi-empirical and based heavily on experimental data. Of course, there are many numerical models available (e.g. Navier-Stokes based-models, discrete-vortex models, wake oscillator models) but due to their limitations (such as laminar, two-dimensional flows at low Reynolds number, sensitivity to the numerical technique used and their dependency on experimental data and flow visualization) they are not reviewed here.



A number of authors, including Maull and Milliner (1978), Sarpkaya and Shoaff (1979) and Graham (1980), have proposed a method that uses Blasius equation and the "discrete-vortex method". Such a method assumes that the induced-force consists of a component due to the attached unsteady irrotational flow past the body and a component generated by the vortices shed into the flow as a result of separation. The application of this model requires detailed information on vortex strengths and trajectories. Such information usually is difficult to obtain, especially for the cases involving wave flows.

In the following sections, the existing semi-empirical models that predict transverse forces are briefly discussed.

#### 4.2.1 Steady Flow Model

This model is similar to the drag force in Morrison's equation and is written in terms of the lift coefficient,  $C_L$  as

$$F_L = \frac{1}{2} \rho_w D \ell C_L U^2. \quad (4.31)$$

The model was originally developed for steady flow where it has been confirmed by many investigators that the transverse force spectra has a single frequency, predicted by Strouhal number,  $S_t = 0.2$  for  $10^3 < Re < 2 \times 10^5$ . Some researchers and designers use this steady flow model for predicting transverse forces for oscillatory and wave flows. In order to account for the time variation of flow velocity and transverse force, a maximum transverse force which yields a lift coefficient defined by

$$C_{Lmax} = \frac{\text{maximum transverse force}}{\frac{1}{2} \rho_w D \ell U_{max}^2} \quad (4.32)$$

has been used.

Others use an *rms* transverse force that gives a lift coefficient defined by

$$C_{Lrms} = \frac{\text{rms value of the transverse force}}{\frac{1}{2} \rho_w D \ell U_{max}^2}. \quad (4.33)$$

Other methods based on semi-peak-to-peak values of the transverse force or different velocities, such as those corresponding to the maximum in-line force rather than to the maximum velocities, will not be discussed here in order to avoid confusion. In the author's opinion, the use of such methods for oscillatory flows, especially wave flows, is one of the reasons for the scatter in the existing  $C_L$  data as illustrated in Fig. 2.14. This is because, unlike the in-line force in oscillatory and wave flows, the transverse force has multiple frequencies and exhibits some degree of irregularity which are a result of the different shedding mechanisms in these types of flow.

#### 4.2.2 Quasi-Steady Model

Recently the steady flow model has been extended to include the frequency of vortex-shedding. Verley (1980), followed by McConnell and Park (1982b), suggested the following simple quasi-steady model

$$F_L = \frac{1}{2} \rho_w D \ell C_L U^2 \sin \omega_v t. \quad (4.34)$$

The model is based on the instantaneous values of flow velocity and vortex-shedding frequency. It also assumes that at the beginning of each half cycle the flow starts from rest again (i.e., does not account for the flows previous history) and the phase is brought to either  $0^\circ$  or  $180^\circ$ . In an attempt to improve this model, Bearman *et al.* (1984) proposed the following quasi-steady model

$$F_L = \pm \frac{1}{2} \rho_w D \ell C_L U_m^2 \cos \phi \sin^2 \omega_f t, \quad (4.35)$$

where  $\phi$  is a function of time given by

$$\phi = 0.2KC [1 - \cos \omega_f t] + \psi, \quad (4.36)$$

$\omega_f$  is the frequency of flow oscillation and  $\psi$  is a constant to be adjusted for every half cycle. This model is also based on the instantaneous flow velocity. It does not predict the sign of the force which depends upon the sense of the vortices shed. It is based on the assumption that the Strouhal number is constant and equal to 0.2

(the appropriate value for steady flow). With a suitable choice of the lift coefficient  $C_L$  for each half cycle of the incident flow, the model seems to work reasonably well for  $KC > 20$ . However, the variation of force with time was found to be somewhat regular and the vortices tend to form and shed in a certain prescribed manner. In general, such a model may be helpful in understanding the flow phenomenon but may not be suitable for design purposes as it is sensitive to the phase angle and still needs an experimentally determined  $C_L$ .

#### 4.2.3 Series Model

Since transverse forces exhibit some degree of irregularity, Mercier (1973) found it is appropriate to express the transverse force in the form of a series. Later Isaacson (1974) and Chakrabarti *et al.* (1976) used the same idea. Their results showed this model to be superior to previous models with regards to the force-time history. In general, the series form of the transverse force can be written as

$$F_L(t) = \frac{1}{2} \rho_w D \ell U_m^2 \sum_{n=1}^N C_{L(n)} \cos(2\pi n f t + \phi_{(n)}), \quad (4.37)$$

where  $N$  is the number of harmonics,  $C_{L(n)}$  is the lift coefficient at the  $n$ th harmonic and  $\phi_{(n)}$  is the phase angle associated with  $C_{L(n)}$ .

In 1977 Sawaragi *et al.* used the same model, but introduced the assumption that the transverse force is a random variable. Moreover, the spectrum of the force in the region of the dominant harmonic can be treated as a narrow-band spectrum. Based on these assumptions, they reduced the series model (Eqn. 4.37) to

$$F_L(t) = \sigma_L \sum_{n=1}^N \sqrt{\frac{2S(nf)\Delta f}{\sigma_L^2}} \cos(2\pi n f t + \phi_{(n)}), \quad (4.38)$$

where  $\sigma_L^2$  is the variance of the transverse force defined by

$$\sigma_L^2 = \left\{ \frac{1}{2} \rho_w D U_m^2 \right\}^2 \cdot \frac{1}{2} E[C_L^2], \quad (4.39)$$

and  $S(nf)\Delta f$  is the spectral energy of the transverse force at frequency  $nf$ .

#### 4.2.4 Proposed Model

Fixed and compliant structures in deep water under the action of nonuniform oscillatory or wave flows have varying values of  $KC$  and  $R_e$  starting from zero at the bottom to a maximum at the surface. Therefore, using the maximum velocity in the series model discussed above does not yield a representative total transverse force. Furthermore, experimental investigations show that, in general, the vortex-shedding process for this type of flow depends on  $KC$  and  $R_e$ . Thus, the lift coefficient is not a constant over the structure. In an attempt to improve the series model the following assumptions were made. The structure was divided into  $N$  number of finite elements with length  $\Delta\ell$ . Each element was then considered to be subjected to uniform flow (see Fig. 4.3). The total transverse force thus could be expressed by

$$F_L(t) = \frac{1}{2} \rho_w D \sum_{m=1}^M \sum_{n=1}^N C_{Lmn} U_{nmax}^2 \Delta\ell \cos(2\pi mft + \phi_{(m)}). \quad (4.40)$$

This representation allows  $C_L$  to be dependent on  $KC$ ,  $R_e$  and the frequency of vortex-shedding.

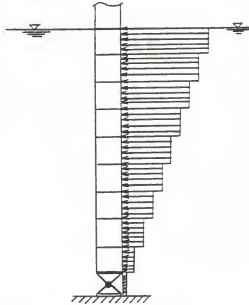


Figure 4.3: Definition sketch showing tower elements and idealized flow.

#### 4.2.5 Fixed Tower

Transverse force data measured during the first series of tests were reduced using the proposed model presented in section 4.2.4. Since the measured data was in terms of the moment of total transverse force about the bottom hinge ( $M_L(t)\frac{L}{\Delta r_t}$ ), the moment form of Eqn. 4.40 was used, i.e.

$$M_L(t)\frac{L}{\Delta r_t} = \frac{1}{2}\rho_w D \sum_{m=1}^M \sum_{n=1}^N C_{Lmn} U_{nmax}^2 r_n \Delta \ell \cos(2\pi m f t + \phi_{(m)}), \quad (4.41)$$

where  $r_n$  is the distance of element  $n$  from the bottom hinge. Substituting  $U_n = a_n \omega_d \sin \omega_d t$ , where  $a_n (= a r_n/L)$  is the amplitude of the tower oscillation at the element  $n$ , and  $\omega_d (= 2\pi f_d)$  the driving frequency, into Eqn. 4.41 results in

$$M_L(t)\frac{L}{\Delta r_t} = \frac{1}{2}\rho_w D \frac{a^2 \omega_d^2}{L^2} \sum_{m=1}^M \sum_{n=1}^N C_{Lmn} r_n^3 \Delta \ell \cos(2\pi m f t + \phi_{(m)}). \quad (4.42)$$

Equation 4.42 is analogous to the Fourier series expression

$$\begin{aligned} f(t) &= \sum_{m=1}^M C_m e^{jm\omega_d t} = \sum_{m=1}^M C_m \cos(m\omega_d t + \psi_{(m)}) \\ &= \sum_{m=1}^M (a_m \cos m\omega_d t + b_m \sin m\omega_d t), \end{aligned} \quad (4.43)$$

where

$M$  = is the number of harmonics,

$f(t) = M_L(t)L/\Delta r_t$ ,

$a_m = \frac{2}{M} \sum_{m=1}^M f(t) \cos m\omega_d t$ ,

$b_m = \frac{2}{M} \sum_{m=1}^M f(t) \sin m\omega_d t$ ,

$\psi_{(m)} = \phi_{(m)} = \tan^{-1} b_m/a_m$  and

$C_m = \sqrt{a_m^2 + b_m^2} = \frac{1}{2}\rho_w D (a^2 \omega_d^2/L^2) \sum_{n=1}^N C_{Lmn} r_n^3 \Delta \ell$ .

In Eqn. 4.43 the coefficients  $C_m$  were obtained by taking the FFT of the measured moment of transverse force  $M_L(t)L/\Delta r_t$ . Then knowing  $C_m$  (Fourier components), the minimum lift coefficients at each element along the tower ( $C_{Ln}$ ,  $n = 1, 2, 3, \dots, N$ .) were obtained by using the method of least squares:

$$\delta_m^2 = \sum_{n=1}^M [(\frac{1}{2}\rho_w D \frac{a^2 \omega_d^2}{L^2} \sum_{n=1}^N C_{Lmn} r_n^3 \Delta \ell) - C_m]^2, \quad (4.44)$$

where the minimum  $C_{Lmn}$  are the solutions of

$$\frac{\partial \delta_n^2}{\partial C_{Lmn}} = 0, \quad m = 1, 2, \dots, M \text{ and } n = 1, 2, \dots, N. \quad (4.45)$$

In other words, for each harmonic the minimum lift coefficients along the tower ( $C_{Ln}$ ) are the solutions of  $\partial \delta^2 / \partial C_{Ln} = 0$  where,  $n = 1, 2, \dots, N$ . This results in the following  $N$  simultaneous equations

$$AX = B, \quad (4.46)$$

where

$$A = \begin{bmatrix} r_1^6 & r_1^3 r_2^3 & r_1^3 r_3^3 & \dots & r_1^3 r_n^3 \\ r_2^3 r_1^3 & r_1^6 & r_2^3 r_3^3 & \dots & r_2^3 r_n^3 \\ \vdots & \vdots & \vdots & \ddots & \vdots \\ r_n^3 r_1^3 & r_n^3 r_2^3 & r_n^3 r_3^3 & \dots & r_n^6 \end{bmatrix},$$

$$X = \begin{Bmatrix} C_{L1} \\ C_{L2} \\ \vdots \\ C_{Ln} \end{Bmatrix} \text{ and}$$

$$B = \begin{Bmatrix} r_1^3 \\ r_2^3 \\ \vdots \\ r_n^3 \end{Bmatrix}.$$

The solution of Eqn. 4.46 at each harmonic is then given by

$$\{X\} = \{C_{Ln}\} = [A]^{-1} \{B\}. \quad (4.47)$$

#### 4.2.6 Complaint Tower

When the articulated tower was allowed to respond freely in the transverse direction, the transverse force was not measured. Instead the transverse motion was measured. Structure motion was found to significantly increase the transverse force (see McConnell and Park, 1982a). One way to quantify the effect of transverse motion is to compute the change in the transverse force due to motion. This force can be determined by computing the force needed to produce the measured response. This

method was used in this study. The measured data for the tower response in the transverse direction was reduced using the following equation of motion

$$I_m \ddot{\psi}(t) = \sum M_{total} = M_g + M_D + M_{fy}, \quad (4.48)$$

where  $I_m$ ,  $M_{total}$ ,  $M_g$  and  $M_D$  are defined in Eqn. 4.1, and  $\psi(t)$  and  $M_{fy}$  are the transverse deflection angle and applied transverse moment, respectively. For the tower shown in Fig. 4.4 the moments  $M_g$ ,  $M_D$  and  $M_{fy}$  were defined as

$$M_g = \left( \sum_{i=1}^k w_i r_i - \int_0^{d_1/\cos\psi(t)} \rho_w A_c g r dr \right) \sin\psi(t) \quad (4.49)$$

$$M_D = -\frac{1}{2} \rho_w D \sum_{n=1}^N C_{Dn} r_n^3 \Delta\ell \dot{\psi}^2(t) \operatorname{sgn}[\dot{\psi}(t)] \quad (4.50)$$

$$M_{fy} = \frac{1}{2} \rho_w D \sum_{m=1}^M \sum_{n=1}^N C_{Lmn} U_{nmax}^2 r_n \Delta\ell \cos(2\pi m f t + \phi_{(m)}) \quad (4.51)$$

where  $A_c = \pi D^2/4$  is the cross sectional area of the tower element. The added mass moment of inertia  $I'_a$  is given by

$$I'_a = \sum_{n=1}^N \frac{\pi}{4} \rho_w D^2 C_{mn} r_n^2 \Delta\ell. \quad (4.52)$$

Substituting these moments into Eqn. 4.48, making the assumption that the measured transverse response  $y_m(t) \simeq L\psi(t)$  and  $d_1/\cos\psi(t) \simeq d_1$  gives

$$\begin{aligned} & (I_o + \sum_{n=1}^N \frac{\pi}{4} \rho_w D^2 C_{mn} r_n^2 \Delta\ell) \ddot{y}_m(t) + \\ & \frac{1}{2L} \rho_w D \sum_{n=1}^N C_{Dn} r_n^3 \Delta\ell \dot{y}_m^2(t) \operatorname{sgn}[\dot{y}_m(t)] + \\ & (\frac{\pi}{8} \rho_w g D^2 d_1^2 - \sum_{i=1}^k w_i r_i) y_m(t) = \\ & -\frac{1}{2} \rho_w D \frac{a^2 \omega_d^2}{L} \sum_{m=1}^M \sum_{n=1}^N C_{Lmn} r_n^3 \Delta\ell \cos(2\pi m f t + \phi_{(m)}), \end{aligned} \quad (4.53)$$

where  $N$  is the number of elements comprising the tower's underwater portion,  $M$  the number of transverse force frequency harmonics and  $k$  the number of the different components making up the tower.





## CHAPTER 5 EXPERIMENTAL DATA ANALYSIS

This chapter contains the data, data analysis and results from 276 test runs for two types of experiments. The sources of uncertainty and inaccuracy associated with the data are also discussed. The results indicate significant effects of flow nonuniformity and structure transverse motion on the vortex-shedding process, loading and thus the structure response.

### 5.1 In-line Forces

The in-line force data were analyzed using Eqn. 4.8 from which the inertia and drag coefficients ( $C_m$  and  $C_D$ ) were obtained by the least squares curve fit technique. It was assumed that these coefficients are constant over one cycle. The mean values of  $C_m$  and  $C_D$  were then computed for 13 to 73 cycles depending on the driving frequency,  $f_d$ . The results show that  $C_m$  and  $C_D$  do not vary significantly from one cycle to the next. The average percentage error between the measured and predicted forces was also computed. For most of the results the error for  $C_m$  and  $C_D$  was less than 5%. A flow chart of the computer program (CDCM), written to analyze these in-line force data, is given in Appendix C.

For the range of Reynolds numbers,  $Re$ , and Keulegan-Carpenter numbers,  $KC$ , tested, the  $C_m$  and  $C_D$  data show a clear dependency on  $Re$  when  $KC$  is held constant. This is consistent with the results in the lower range of  $KC$  for a mechanically oscillated cylinder in still water, see Chakrabarti *et al.* (1983). The results for  $C_m$  and  $C_D$  versus  $Re$  for different values of  $KC$  are shown in Figs. 5.1 and 5.2. These figures show that, for the range of  $KC$  and  $Re$  tested,  $C_m$  and  $C_D$  are strongly dependent

on  $KC$  and  $R_e$  and are decreasing as  $R_e$  increases. This trend is also consistent with the trend reported by others for the range of the parameters tested (see Sarpkaya, 1976a). Figure 5.1 also suggests that the fluid added mass increases as the cylinder amplitude of oscillation increases, i.e., as  $KC$  increases.

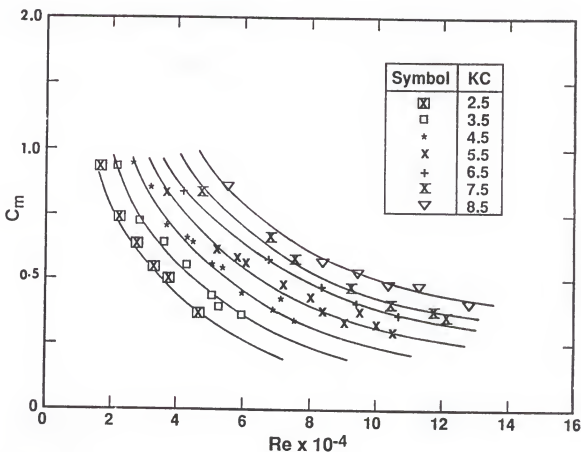


Figure 5.1:  $C_m$  versus  $R_e$  for harmonically oscillated articulated tower (transversely unconstrained).

It was observed by many investigators (e.g. Sarpkaya, 1976a) that, for lower range of  $KC$ , the in-line force is usually inertia dominated. The data from these tests were also more suitable for extracting  $C_m$  than  $C_D$ , since the maximum  $KC$  attained was 9.35. This was examined by calculating the "error surfaces" which are a minimum at  $C_{Dmin}$  and  $C_{min}$ . The method used is discussed in detail by Dean (1976). Figure 5.3 shows an example of these error surface contours for one of the test runs. Most of the other runs show the same shape which means that the data are well-conditioned

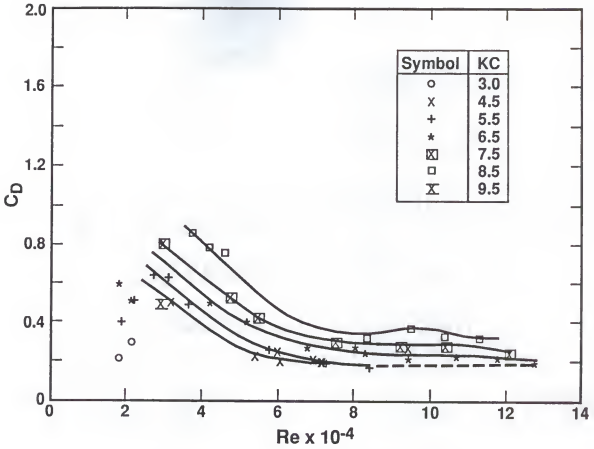


Figure 5.2:  $C_D$  versus  $Re$  for harmonically oscillated articulated tower (transversely unconstrained).

for determining  $C_m$ . The scatter in  $C_D$  could be caused by the errors from various sources as will be discussed later in this chapter. In summary, the number of useful data points for establishing the  $C_D - Re$  relationship is small compared to the number used for  $C_m$  especially in the lower range of  $KC$ . The phase relationship between the measured forces and the corresponding calculated forces was also examined. The phase differences were generally found to be small. This is illustrated in Fig. 5.4, which shows a few examples of the force time history.

In an effort to show the effect of flow nonuniformity on these data, a comparison of the present  $C_D$  and  $C_m$  data with those obtained by Sarpkaya (1976a) in uniform oscillatory flow and Bearman *et al.* (1985) in waves was made. The results are shown in Figs. 5.5 and 5.6. Although both  $C_m$  and  $C_D$  show the same trend for the range

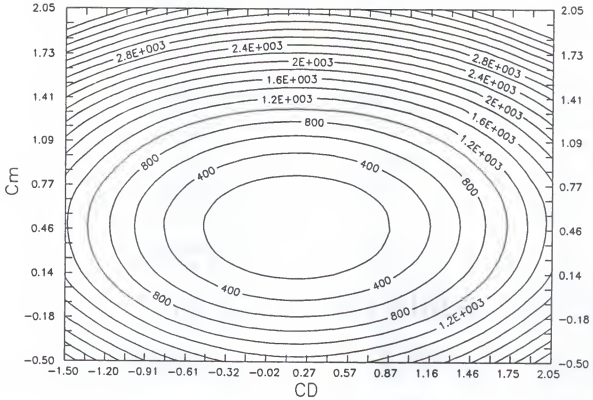


Figure 5.3: Contour lines defining error surfaces of the in-line force ( $KC = 8.4$  and  $R_e = 8.4 \times 10^4$ ).

of  $KC$  tested,  $C_m$  does not exhibit a dependency on the type of flow. On the other hand,  $C_D$  seems to be affected by the flow nonuniformity in that its magnitude is less for nonuniform and wave flows than for uniform oscillatory flow. The  $C_D$  values in waves and nonuniform oscillatory flows were found to fall within the same range. The differences between  $C_D$  values in uniform and nonuniform oscillatory flows could be attributed to the varying  $R_e$  along the cylinder in the nonuniform oscillatory and wave flow cases since  $R_e$  varies from a value close to zero at the bottom to a maximum value at the water surface. This in turn could cause the flow to change from subcritical to critical or even supercritical (depending on the water depth and the cylinder diameter) along the cylinder. It may also cause the vortices to separate from the surface at different moments in time along the cylinder leading to a phase difference between the vortices and consequently a smaller correlation length.

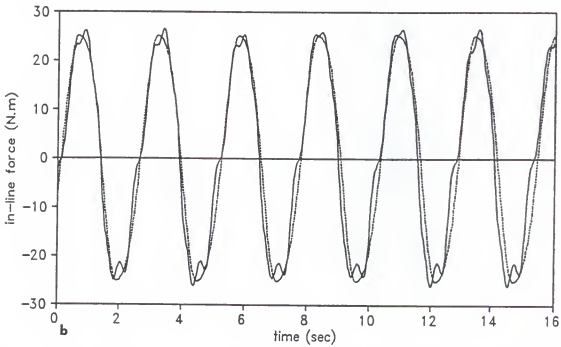
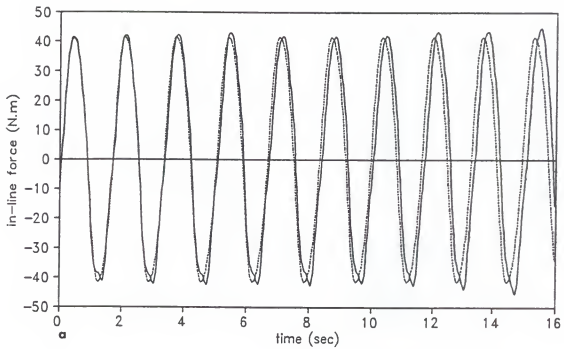


Figure 5.4: Phase comparison between measured and predicted in-line forces (a)  $KC = 6.6$  and  $R_e = 9.4 \times 10^4$  (b)  $KC = 8.4$  and  $R_e = 8.4 \times 10^4$  (— measured, .... predicted).

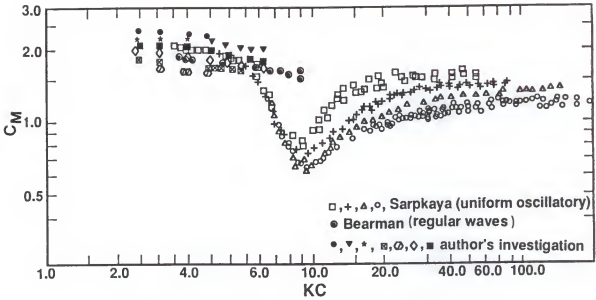


Figure 5.5: Comparison of  $C_m$  for different flow types.

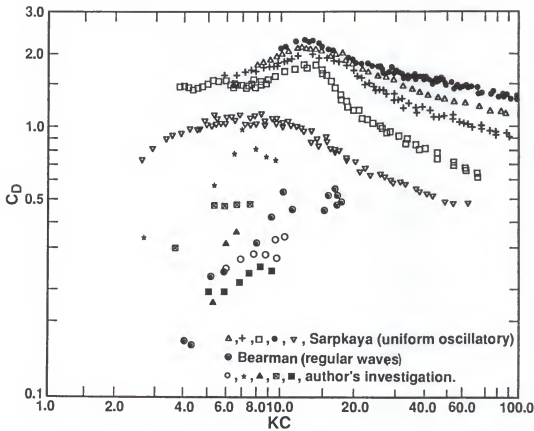


Figure 5.6: Comparison of  $C_D$  for different flow types.

Equation 4.25 was also used instead of Eqn. 4.8 to reduce the in-line force data and to examine the drag force-velocity relationship. A flow chart of the computer program (CDCMN) to compute  $C_m$ ,  $C_D$  and  $n$  is given in Appendix C. Examples were run to test the drag-velocity relationship. The results show that the power " $n$ " to which the velocity is raised is close to 2 for most of the cases tested; see Table 5.1 for samples of the results.

Table 5.1: Samples of test results on in-line force data

$R_e$	$KC$	$n$	$C_D$	$C_M$
$5.82 \times 10^4$	5.9	1.98	0.35	1.15
$8.35 \times 10^4$	8.4	1.81	0.19	1.16
$9.50 \times 10^4$	5.8	1.97	0.55	0.72
$8.30 \times 10^4$	6.7	1.86	0.23	0.90
$9.40 \times 10^4$	6.6	2.04	0.13	0.78
$1.20 \times 10^5$	6.6	1.96	0.15	0.69
$4.20 \times 10^4$	6.5	1.88	1.00	1.77
$3.32 \times 10^4$	6.5	2.05	0.88	2.30

## 5.2 Transverse Forces

In this section the analysis of the data pertaining to vortex-induced transverse forces is presented for both the transversely constrained and the unconstrained experiments. This includes the analysis of measured transverse forces, thermistor signals and transverse motion.

### 5.2.1 Constrained Transverse Motion

When the tower was constrained from motion in the transverse direction, the transverse forces were analyzed using the proposed transverse force model, Eqn. 4.42. The lift coefficients  $C_{L(n)}$  and their associated phase angles  $\phi_{(n)}$  for the first eight harmonics were evaluated using Eqns. 4.47. A flow chart of the computer program (CLEF) written to obtain  $C_{L(n)}$  and  $\phi_{(n)}$  from the measured transverse force data is given in Appendix C. The results obtained were plotted versus different parameters,

such as,  $KC$ ,  $R_e$  and  $\beta$ . The values of the lift coefficients,  $C_{L(n)}$  were found to be dependent on both  $KC$  and  $R_e$ . However, the  $C_{L(n)}$  values were found to correlate better when plotted versus  $KC$  for constant  $\beta$ , see Figs. 5.7 and 5.8. In general,  $C_{L(n)}$  decreases with increasing  $KC$  as shown in Figs. 5.7 and 5.8. For  $KC > 7.0$ ,  $C_{L(n)}$  values start to increase slightly indicating the possibility of a multi-peak relationship with  $KC$ . This behavior has also been observed by Bearman *et al.* (1981) and Ikeda and Yamamoto (1981).

The dependency of the  $C_{L(n)}$  values on  $\beta$  and  $R_e$  was also found to be strong, especially for the first four harmonics where the lift coefficients are the largest, see Fig. 5.7.  $C_{L(n)}$  were also plotted versus  $\beta$  for constant  $KC$  as shown in Figs. 5.9 and 5.10. The trend exhibited in Fig. 5.9 suggests that there is a critical value of  $\beta$  or  $R_e$  at which the lift coefficient is a maximum. Of all the different harmonics, the largest value of the lift coefficient occurs at the driving frequency. In general, the magnitudes of the different components of the lift coefficients were found to vary between 0.0 and 0.7 except at  $\beta = 2, 100$  where,  $C_{L(1)}$  reached a value of 1.4.

On the other hand, the associated phase angles show no orderly dependency on  $R_e$ ,  $KC$  or  $\beta$ . As can be seen in Figs. 5.11 and 5.12, the phase angle data associated with the lift coefficients ( $C_{L(n)}$ ) appear to be random. This random phase could be related to the shedding process that exhibits modes of behavior with vortex interaction between newly shed and earlier formed vortices. The variability in the modes and thus phasing of the vortices shed along the cylinder could also be a major factor. The phase relationship between the measured transverse forces and the corresponding predicted forces using the proposed model for computing transverse force show that while the maximum forces are reasonably correlated, the phase differences are often large. A few examples of the force profiles are shown in Figs. 5.13 and 5.14.



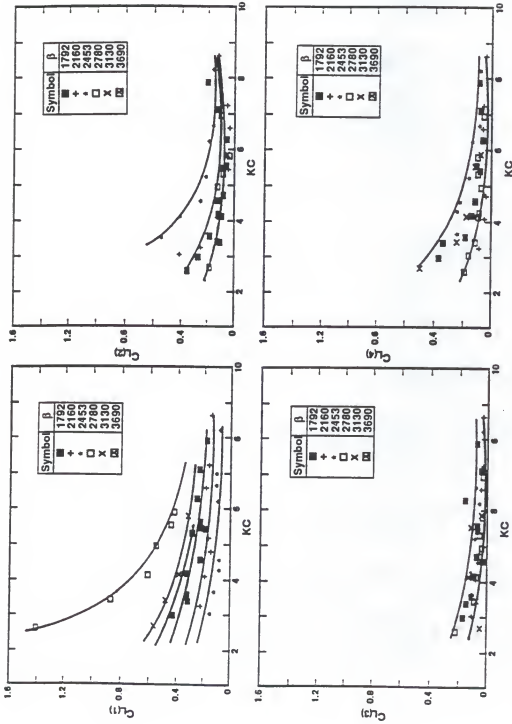


Figure 5.7: Lift coefficient harmonics for harmonically oscillated articulated tower (transversely constrained),  $C_{L(1)}$  to  $C_{L(4)}$ .

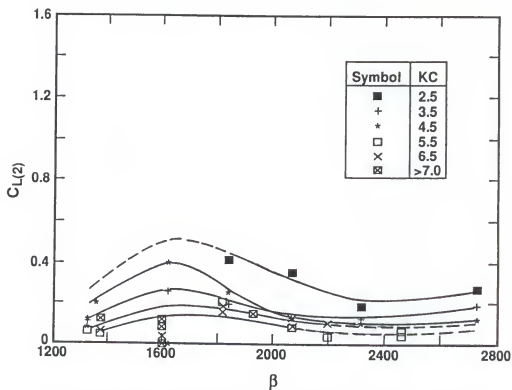
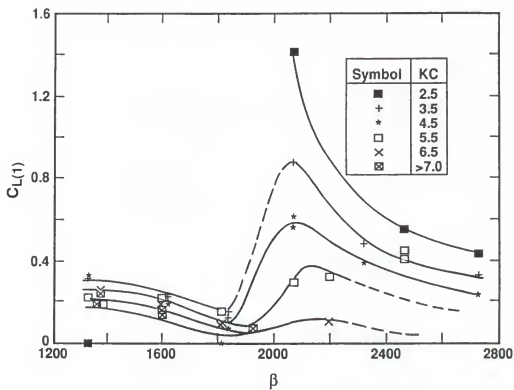


Figure 5.9: Lift coefficient harmonics versus beta,  $C_{L(1)}$  and  $C_{L(2)}$ .

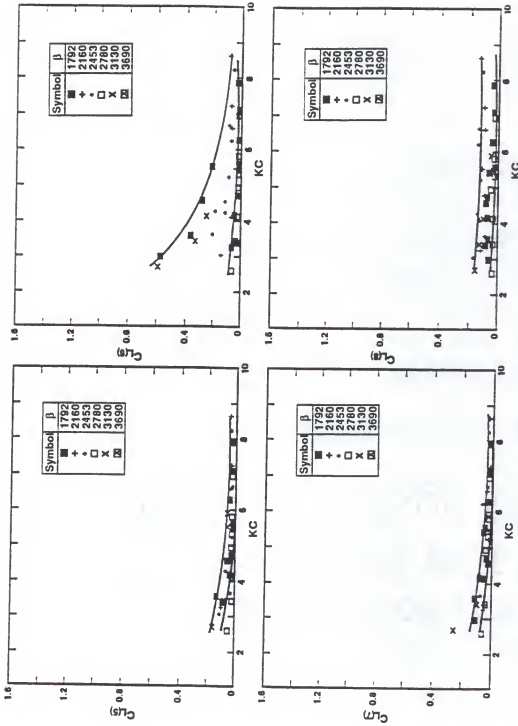


Figure 5.8: Lift coefficient harmonics for harmonically oscillated articulated tower (transversely constrained),  $C_{L(5)}$  to  $C_{L(e)}$ .

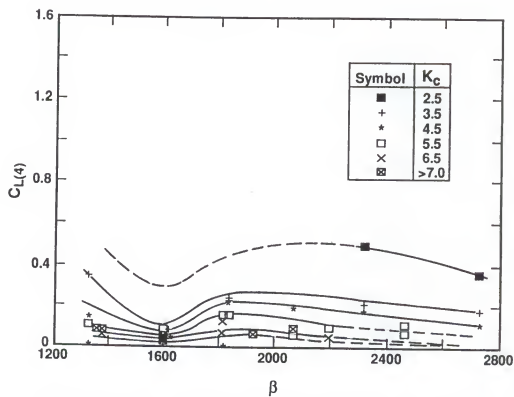
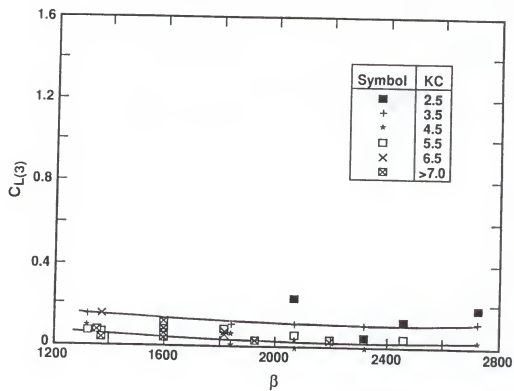


Figure 5.10: Lift coefficient harmonics versus beta,  $C_{L(3)}$  and  $C_{L(4)}$ .

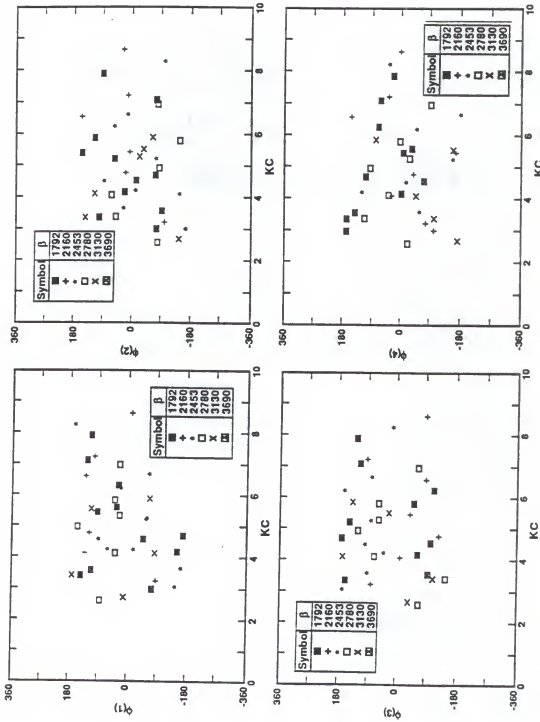


Figure 5.11: Phase angle associated with the lift coefficients harmonics,  $\phi(1)$  to  $\phi(4)$ .

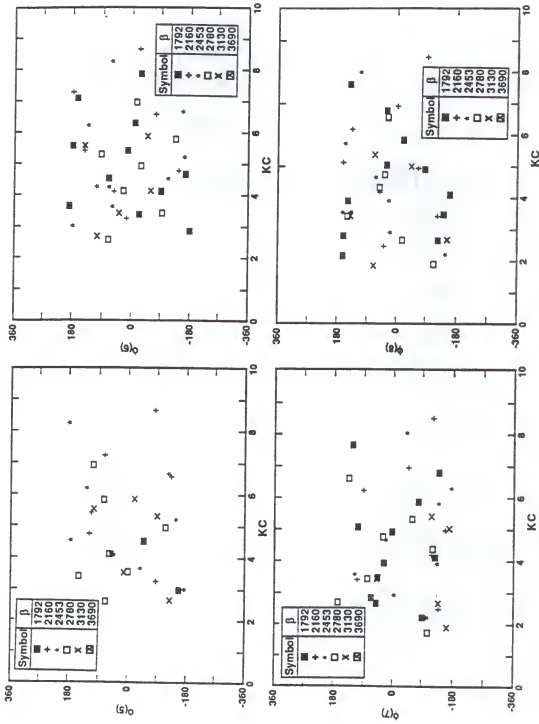


Figure 5.12: Phase angle associated with the lift coefficients harmonics,  $\phi_0$  to  $\phi_s$ .

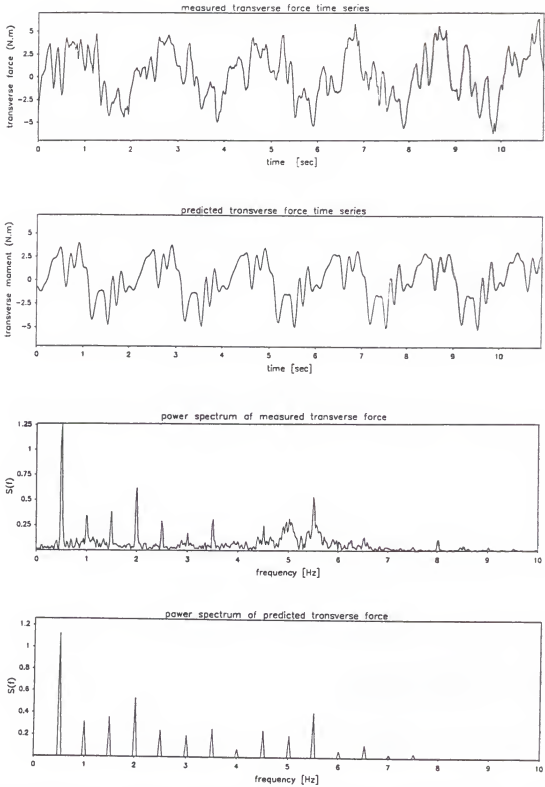


Figure 5.13: Comparison between measured and predicted transverse forces ( $R_* = 10^4$  and  $KC = 5.45$ ).

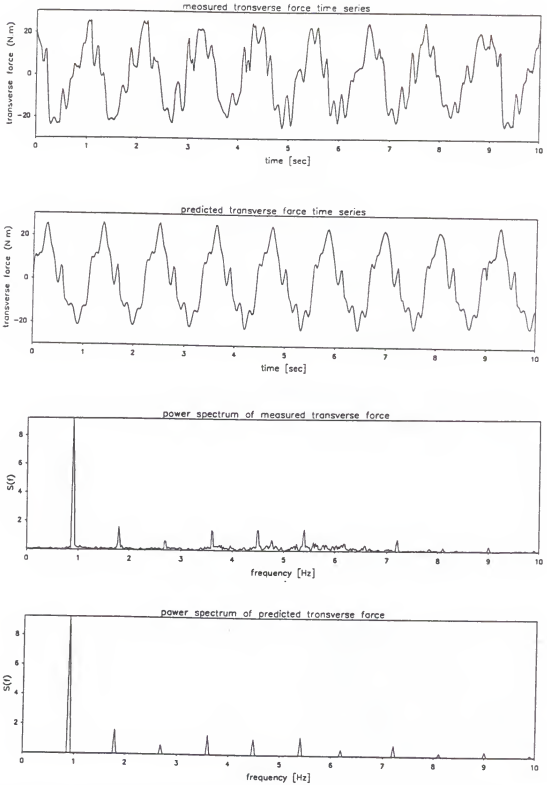


Figure 5.14: Comparison between measured and predicted transverse forces ( $R_e = 2 \times 10^4$  and  $KC = 5.9$ ).



For the purpose of comparison with other investigators' data the transverse force data were also analyzed in terms of  $C_{Lrms}$  which is defined as

$$C_{Lrms} = \frac{F_{rms}(t)}{\frac{1}{2} \rho_w D \ell U_{max}^2} \quad (5.1)$$

where  $F_{rms}(t)$  is the root-mean-square (*rms*) value of the measured transverse force. The results shown in Fig. 5.15 exhibit the same trend as the  $C_L$  harmonics and are found to correlate well with  $KC$  for constant  $\beta$  with magnitudes varying between 0.12 and 0.6. In this figure the results show that, for  $KC < 5$  (where almost no published data exist for nonuniform oscillatory flow)  $C_{Lrms}$  increases as  $KC$  decreases. However, as one would expect, according to other investigators data for  $5 < KC < 11$ ,  $C_{Lrms}$  increases as  $KC$  increases (see Fig. 2.14).

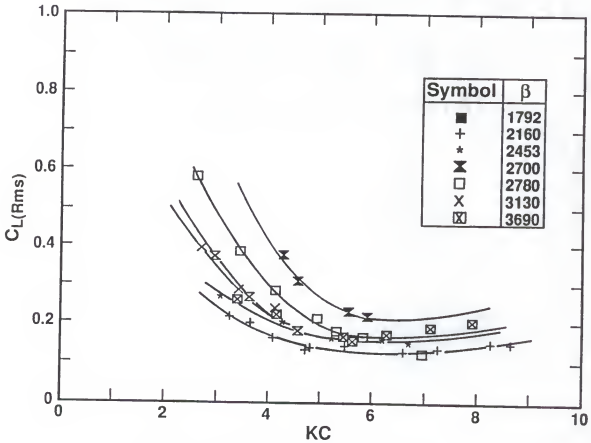


Figure 5.15: RMS lift coefficient versus  $KC$ .

The present  $C_{Lrms}$  data were also plotted with other investigators' data obtained for waves, see Fig. 5.16. As shown in this figure, where  $KC$  overlaps, the lift coefficients,  $C_{Lrms}$ , for the oscillating tower in still water agrees very well with  $C_{Lrms}$  data for waves. For the range of  $Re$  and  $KC$  tested, Fig. 5.16 confirms the possibility of a secondary peak for  $KC$  between 2.0 and 3.0. This would give a  $KC$  spacing of  $\simeq 8.5$  from the main peak which is at  $KC \simeq 11.0$ . This is approximately the interval of  $KC$  found by Ikeda and Yamamoto as reported by Williamson (1985). Intervals between the  $C_L$  peaks were found to be approximately 7.5 for  $KC \leq 70.0$ .

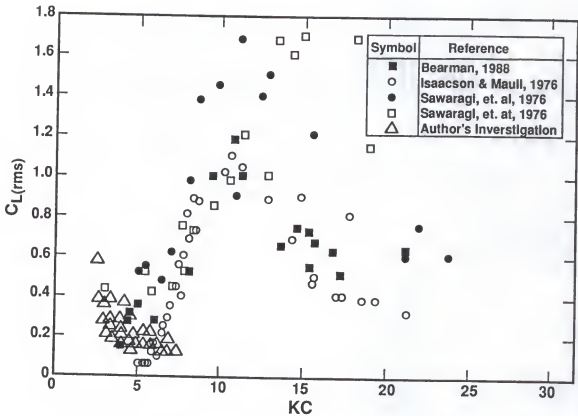


Figure 5.16: Comparison of  $C_{Lrms}$  data with those from waves.

Even though the data from proprietary studies are not available, the ranges of  $Re$  and  $KC$  covered by these data sets are generally known. To the author's knowledge  $C_L$  data does not exist for most of the range of the parameters covered in these experiments. As indicated earlier this is an important range for many structural elements



duration and 0.025 seconds time intervals (which gives a frequency resolution of approximately 0.078 Hz) were chosen. The final spectrum consisted of the average of 5 spectral estimates. Since the frequency of vortex-shedding in oscillatory flows is known (see literature review, Chapter 2) to be related to the in-line flow oscillation frequency, the frequencies in the power spectra were normalized by the driving frequency. Also to illustrate the dependency of the different harmonics in the transverse force on  $Re$  and  $KC$ , the power spectra were plotted, as groups, for a range of  $KC$  tested holding  $Re$  constant. They were also plotted holding  $\beta$  constant. Figure 5.18 and Fig 5.19 show examples of these spectra for constant  $Re$  and  $\beta$ , respectively.

On investigating the frequency of the peaks of these force spectra, it was observed that the frequency of the dominant peak was always a multiple of the driving frequency (i.e., frequency ratio  $f_v/f_d = N$ , where  $N$  is an integer). This agrees with the findings of other investigators in oscillatory flows and waves (e.g. Chakrabarti *et al.*, 1976, 1983; Bearman and Hall, 1987; Justesen, 1989; and others). The plots in Fig. 5.19, where  $\beta$  is the correlating parameter, exhibit the same trend as those of other investigators shown in Fig. 2.9. Because the frequency of vortex-shedding is known to be a very important parameter in this type of fluid-structure interaction problem, the measured signals from the thermistors mounted on the tower's surface were also analyzed using spectral analysis techniques. The spectra of the thermistor signals were found to have the same trend with  $KC$ , when  $\beta$  was held constant, as those for the transverse force data shown in Fig. 5.19. Examples of thermistor output spectra are shown in Figs. 5.20 and 5.21. Each figure comprises 5 spectra of signals from the top 5 thermistors (the only ones that worked for all of the tests) placed one diameter apart along the length of the cylinder, see Fig. 5.22.

Similar results were found to exist for all values of  $\beta$  tested. This supports the finding that  $\beta$  rather than  $Re$  is a better correlating parameter for the vortex-shedding frequency. In general these spectra show that the frequency of the dominant peak is

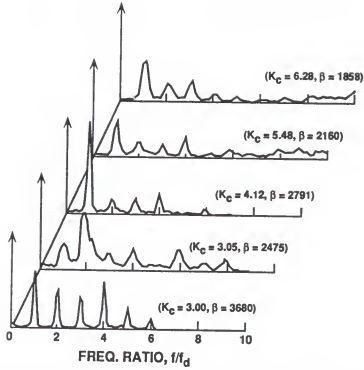


Figure 5.18: Transverse force power spectra for constant  $R_e$  ( $R_e = 1.15 \times 10^4$ ).

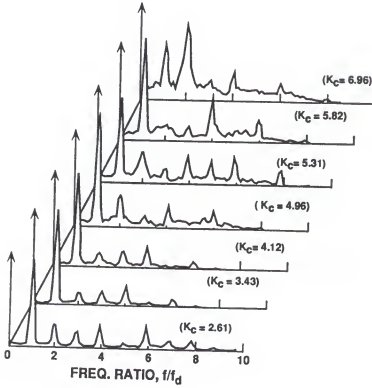


Figure 5.19: Transverse force power spectra for constant  $\beta$  ( $\beta = 2,800$ ).

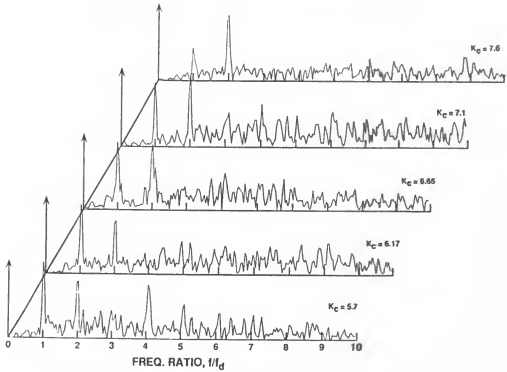


Figure 5.20: Thermistor power spectra for  $\beta = 1,834$ .

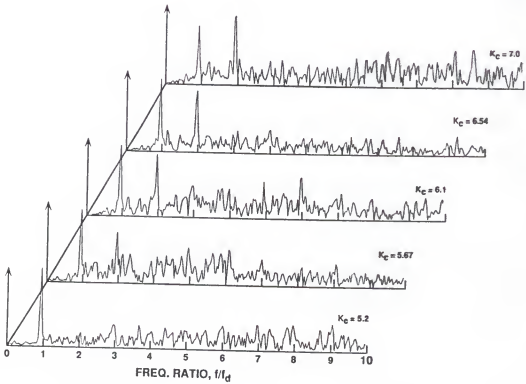


Figure 5.21: Thermistor power spectra for  $\beta = 2,161$ .

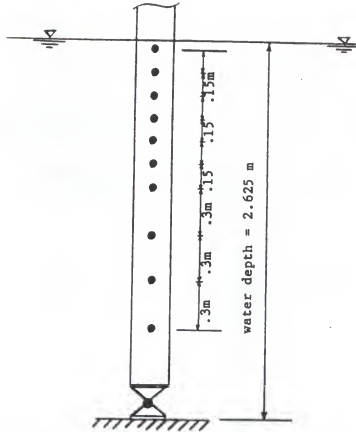


Figure 5.22: Schematic illustration of thermistors locations.

at the driving frequency for lower values of  $KC$ . At these values of  $KC$ , where two asymmetric vortices remain attached to the cylinder, the ratio  $f_v/f_d = N = 1$ . As  $KC$  increases to a certain value (depending on the value of  $\beta$ ) the ratio  $N$  shifts to 2, where two vortices with opposite signs are shed in one cycle. Figure 5.19 shows that the shift to  $N = 2$  happens for a value of  $KC$  between 7.1 and 7.9 for  $\beta = 1,800$ . When  $\beta$  is 2,800 this shift occurs at a lower value of  $KC$  ( $KC$  between 5.8 and 7). The vortex patterns shown in Fig. 5.23 were observed in these tests. This observation helps explain the behavior shown in Fig. 5.19.

Transverse forces are not always well correlated over the length of the cylinder. In nonuniform oscillatory and wave flows, forces at two cross-sections separated by a distance as little as two diameters may be in phase part of the time and out of phase

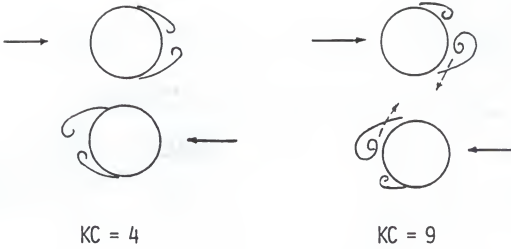


Figure 5.23: Schematic illustration of the visualization of the vortex-shedding process.

at other times. Accordingly, the total transverse force acting on a length of a few diameters or more is likely to be considerably smaller than that suggested by a lift coefficient derived from force measurements at one section. The vortex correlation length is, therefore, a very important parameter in interpreting the results of measured transverse forces.

In this study correlation lengths were computed from the thermistor signal data. The thermistors were mounted at 10 different locations along the tower model (the top 7 thermistors were one cylinder diameter apart and the bottom 3 thermistors were two cylinder diameters apart). The correlation was calculated between the top thermistor signal and each of the following thermistors using the correlation coefficient  $\gamma_{xy}(f)$ , defined by

$$\gamma_{xy}(f) = \frac{|S_{xy}(f)|^2}{S_{xx}(f) \cdot S_{yy}(f)}, \quad (5.2)$$

where  $S_{xy}(f)$  is the cross spectrum between the two signals  $x(t)$  and  $y(t)$ ,  $S_{xx}(f)$  and  $S_{yy}(f)$  are the auto spectrums of the signals  $x(t)$  and  $y(t)$ , respectively.

Out of the 10 thermistors on each side of the tower, only the top 5 thermistors were found to work during all tests. They are located up to 6 diameters from the water



surface. The computed correlation coefficients of these thermistor signals were plotted versus the span-wise coherence length,  $z/D$  (see Fig. 5.24 for definition) for all values  $KC$  and  $\beta$  tested. In this study, the thermistor signals were considered to be coherent if their correlation coefficient was greater 0.9. The data were found to correlate better with  $\beta$  than  $KC$ , see Fig. 5.25.  $KC$  has been found to correlate coherence length data for uniform oscillatory flows (see, Obasaju *et al.*, 1988 and Kozakiewicz *et al.*, 1991). Figure 5.25 indicates that the vorticies are strongly correlated at  $\beta = 2,161$  which is exactly the location at which the first harmonic lift coefficient peaks (see Fig. 5.9). This phenomenon, i.e., the dependence of  $z/D$  on  $\beta$ , is more apparent in a plot of  $z/D$  versus  $\beta$ , as shown in Fig 5.26. The general behavior exhibited by this figure is similar to that reported by Overvik (1982) for Scruton's (1967) work in steady flow. For  $\beta = 2,161$ ,  $\gamma_{xy}(f)$  is near unity for all values of  $z/D$  examined. On the other hand the correlation of the vortices at  $\beta = 3,690$  is particularly poor. In general the results presented in Fig. 5.26 suggest that the vortex correlation length decreases with increasing  $\beta$ .

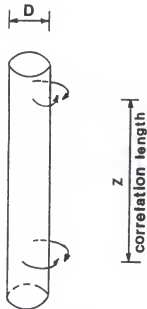


Figure 5.24: Definition sketch of span-wise coherence length.

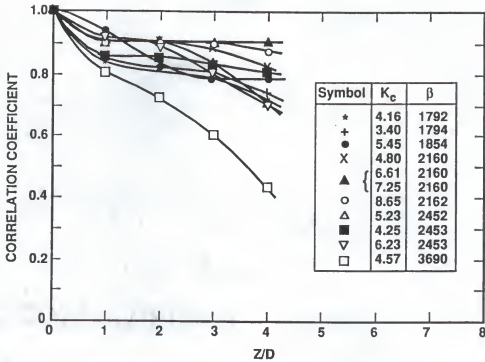


Figure 5.25: Span-wise coherence length for transversely constrained articulated tower.

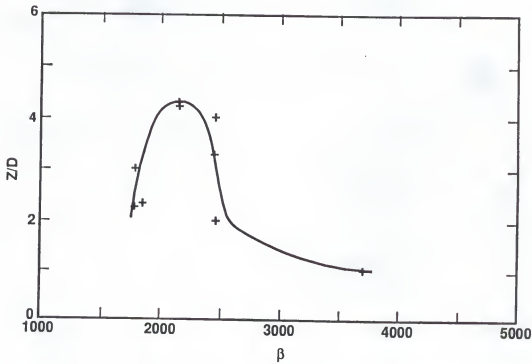


Figure 5.26: Span-wise coherence length for transversely constrained articulated tower.

### 5.2.2 Unconstrained Transverse Motion

When the tower was free to move in the transverse direction, the transverse forces were obtained indirectly by measuring the transverse response and computing the forces needed to produce the motion. The lift coefficients and the associated phase angles can then be determined in a manner similar to that used for the first type of experiment (transversely constrained tower). The problem with this approach is that reliable values for  $C_m$  and  $C_D$  for the range of  $KC$  and  $R_e$  (based on transverse motion) experienced are needed. Data for  $C_m$  and  $C_D$  for the relatively low values of  $KC$  and  $R_e$  in these experiments are limited or nonexistent. The values of  $KC$  and  $R_e$  (based on transverse motion) for the tests where substantial transverse motion existed are shown in Table 5.2.

To quantify the effect of transverse motion on lift coefficients, a computer program (CLEUF) using Eqn. 4.54 was written for computing  $C_{L(n)}$  and the associated phase angles  $\phi_{(n)}$  from the measured transverse motion. A flow chart of this program is given in Appendix C. A few cases from Table 5.2 were tested and the results presented in Table 5.3. For these cases the values of  $C_M$  and  $C_D$ , obtained from the measured in-line forces (Figs. 5.1 and 5.2), and values from other investigators were extrapolated to the transverse motion  $KC$  values. The results indicate that when transverse motion is allowed, the lift coefficients are increased significantly, at least by a factor of 2.5. McConnell and Park (1982a) oscillated an elastically-mounted cylinder uniformly in still water and found that response in the transverse direction increased the lift coefficient of the fixed cylinder by a factor of up to 2.0.

The  $C_L$  data contained in Table 5.3 were then used to evaluate the phase relationship between the measured and predicted transverse motion. This requires that Eqn. 4.53 be solved for the response of the tower,  $y_p(t)$ . Because the equation is nonlinear, it was solved numerically using the Runge-Kutta technique. Details of this technique are given in Appendix A and a flow chart for the computer program (ATVSR) used

to calculate the tower response is given in Appendix C. Results of the program, using the  $C_L$  data given in Table 5.3, show that fewer harmonics, than for the constrained case, are needed in the proposed transverse force model to get the best fit between the measured and predicted response. This means that when transverse motion is allowed the transverse forces due to vortex-shedding are more regular. Figure 5.27 shows a few examples in which only 2 harmonics were used. The lift coefficients were on the average 3 times larger than those corresponding to the case where transverse motion was not allowed.

Table 5.2: Test conditions for cases where large transverse motion were measured.

$\omega_d$ (Hz)	in-line $R_e$	in-line $KC$	in-line $\beta$	transverse $R_e$	transverse $KC$	transverse $\beta$
0.25	$2.72 \times 10^4$	5.0	5,432	$2.07 \times 10^3$	4.12	503
0.25	$3.14 \times 10^4$	5.8	5,404	$2.28 \times 10^3$	4.54	503
0.25	$2.07 \times 10^4$	4.0	5,170	$1.28 \times 10^3$	2.68	477
0.25	$2.54 \times 10^4$	4.9	5,132	$2.28 \times 10^3$	4.78	477
0.30	$3.19 \times 10^4$	4.9	6,501	$1.92 \times 10^3$	3.18	604
0.30	$3.68 \times 10^4$	5.7	6,501	$2.49 \times 10^3$	4.12	604
0.30	$4.21 \times 10^4$	6.5	6,500	$2.86 \times 10^3$	4.74	604
0.30	$4.75 \times 10^4$	7.3	6,504	$3.24 \times 10^3$	5.36	604
0.40	$5.20 \times 10^4$	5.3	9,890	$1.33 \times 10^3$	1.44	924
0.40	$5.82 \times 10^4$	5.9	9,862	$1.90 \times 10^3$	2.06	923
0.40	$6.75 \times 10^4$	6.8	9,923	$2.28 \times 10^3$	2.47	924
0.40	$7.55 \times 10^4$	7.6	9,918	$3.04 \times 10^3$	3.30	922
0.40	$8.35 \times 10^4$	8.4	9,926	$3.42 \times 10^3$	3.71	922
0.40	$9.42 \times 10^4$	9.3	10,069	$3.80 \times 10^3$	4.12	922
0.50	$7.22 \times 10^4$	5.8	12,424	$2.14 \times 10^3$	1.86	1,150
0.50	$8.32 \times 10^4$	6.7	12,413	$2.38 \times 10^3$	2.06	1,154
0.50	$9.23 \times 10^4$	7.5	12,396	$2.61 \times 10^3$	2.27	1,152
0.50	$1.04 \times 10^5$	8.4	12,398	$2.85 \times 10^3$	2.48	1,150
0.50	$1.13 \times 10^5$	9.1	12,416	$3.56 \times 10^3$	3.10	1,150
0.60	$8.04 \times 10^4$	5.7	14,159	$1.46 \times 10^3$	1.11	1,316
0.60	$9.42 \times 10^4$	6.6	14,265	$1.95 \times 10^3$	1.50	1,302
0.60	$1.04 \times 10^5$	7.3	14,217	$2.33 \times 10^3$	1.80	1,296
0.60	$1.18 \times 10^5$	8.2	14,265	$2.71 \times 10^3$	2.06	1,317
0.60	$1.28 \times 10^5$	9.0	14,178	$3.26 \times 10^3$	2.47	1,318
0.70	$1.07 \times 10^5$	6.6	16,278	$2.49 \times 10^3$	1.65	1,512

Table 5.3: Results of lift coefficients when transverse motion existed.

in-line $R_e$	in-line $KC$	$y_{rms}/D$ $\times 100$	in-line $V_r$	constrained $C_{L(1),(2),(3)}$	unconstrained $C_{L(1),(2),(3)}$
$2.7 \times 10^4$	5.0	49%	8.4	—	0.57, 0.05, 0.11
$3.1 \times 10^4$	5.8	57%	9.7	—	0.60, 0.05, 0.11
$4.7 \times 10^4$	7.3	60%	14.6	—	0.76, 0.06, 0.04
$5.2 \times 10^4$	5.3	16%	14.0	—	0.48, 0.024, 0.005
$5.8 \times 10^4$	5.9	28%	15.6	—	1.43, 0.053, 0.03
$6.8 \times 10^4$	6.8	35%	18.1	—	1.48, 0.05, 0.04
$7.2 \times 10^4$	5.8	21%	19.4	0.19, 0.05, 0.07	0.68, 0.03, 0.007
$8.3 \times 10^4$	6.7	25%	22.3	0.25, 0.06, 0.15	0.75, 0.03, 0.012
$9.2 \times 10^4$	7.5	28%	24.8	0.24, 0.12, 0.04	0.77, 0.07, 0.002
$1.0 \times 10^5$	6.2	9%	33.2	0.31, 0.04, 0.03	0.65, 0.03, 0.005
$1.0 \times 10^5$	8.4	33%	27.8	0.19, 0.20, 0.08	0.61, 0.06, 0.02
$1.1 \times 10^5$	6.6	20%	30.6	0.10, 0.15, 0.07	0.41, 0.01, 0.002
$1.3 \times 10^5$	9.0	34%	36.1	0.14, 0.12, 0.03	0.38, 0.02, 0.002

Other numerical tests were also performed to examine the effect of transverse motion on the magnitude of transverse forces. In these tests the transverse response was predicted using the measured transverse forces on the constrained tower for the same in-line conditions. The same computer program "ATVSR" was used to predict the tower response due to the measured transverse forces. This was carried out by replacing the expression on the right hand side of Eqn. 4.53 by the the measured transverse force. Many cases were tested and most show that the amplitude of the predicted response are less than that measured by at least 40%. Results also show that the predicted responses are more irregular than those measured. Some of the cases tested are shown in Figs. 5.28 to 5.31. The spectra of these measured and predicted responses (Figs. 5.29 and 5.31) show substantial differences in energy. These results further support the earlier findings that the transverse motion significantly increases the transverse forces. Therefore, transverse force or lift coefficient data obtained from measurements on stationary (fixed) structures cannot be used to predict the response of compliant structures.

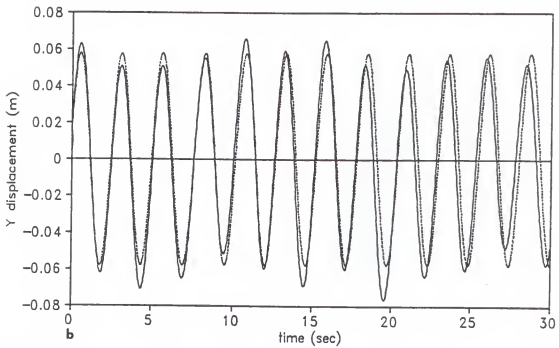
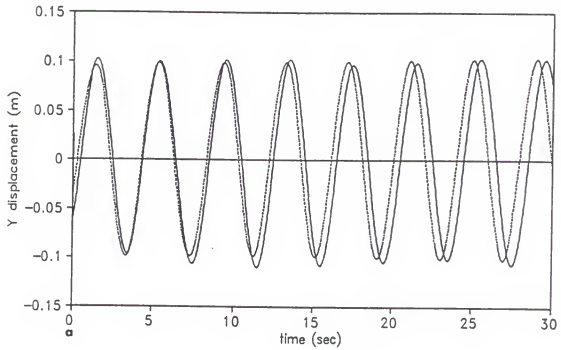


Figure 5.27: Comparison between measured and predicted transverse responses (a)  $R_e = 2.7 \times 10^4$  and  $KC = 5.0$  (b)  $R_e = 5.8 \times 10^4$  and  $KC = 5.9$  (— measured, .... predicted).

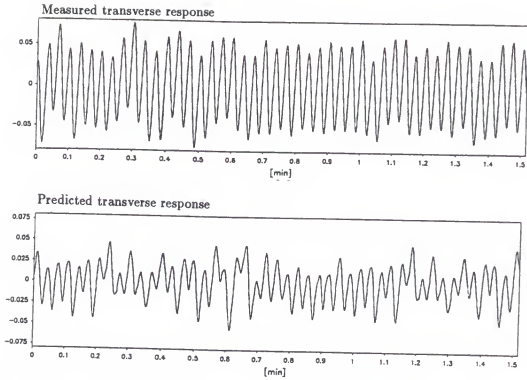


Figure 5.28: Comparison of measured and predicted transverse responses ( $R_e = 8.3 \times 10^4$  and  $KC = 6.7$ ).

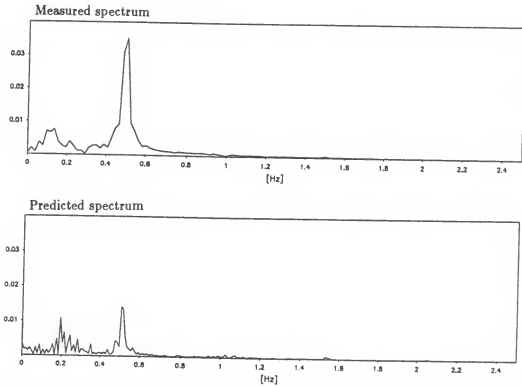


Figure 5.29: Comparison of measured and predicted spectra of transverse responses ( $R_e = 8.3 \times 10^4$  and  $KC = 6.7$ ).

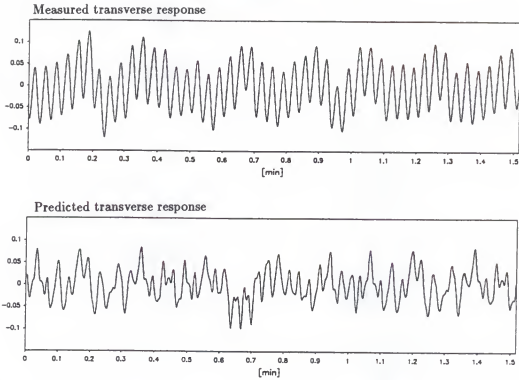


Figure 5.30: Comparison of measured and predicted transverse responses ( $R_e = 10^5$  and  $KC = 8.4$ ).

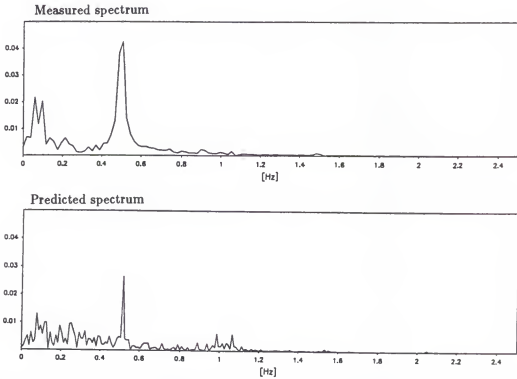


Figure 5.31: Comparison of measured and predicted spectra of transverse responses ( $R_e = 10^5$  and  $KC = 8.4$ ).



As the magnitude of the transverse force was found to be dependent on the transverse motion and in-line flow parameters, the frequency of this force is like-wise believed to depend on these quantities. It is known that introducing even a small transverse motion will cause vortex-shedding to be more regular. It was also found that when the tower was transversely constrained, the vortex-shedding frequency is related to the driving frequency and  $\beta$ . This finding is believed to be valid for the unconstrained case as well. The frequency of vortex-shedding was analyzed and presented with this in mind. In the unconstrained experiments the vortex-shedding frequency was obtained from spectral analyses of the measured signals from the thermistors mounted along the cylinder. These spectra show vortices being shed at frequencies that are multiple of the driving frequency. Out of the several peaks in the power spectrum, the largest peak was considered to be the dominant frequency of vortex-shedding.

In the analysis of the data of these tests,  $y_{rms}/D$  was used as a parameter to characterize the relative magnitude of transverse motion. To study the effect of transverse motion, the spectra of the thermistor signals have been examined in many ways i.e., for constant  $\beta$  and  $y_{rms}/D$ , but varying  $KC$  or  $R_e$  or  $V_r$ . It was found that these spectra become most meaningful when grouped together for constant  $\beta$  and  $y_{rms}/D$  but varying  $V_r$ . The test runs that exhibited transverse motion in this second set of experiments covered the range of  $\beta$  between 6,500 and 16,876. For  $14,265 < \beta < 16,876$ , (where the maximum  $y_{rms}/D$  was less than 34%) it was found that the dominant vortex-shedding frequencies exhibited the same trend as in the first set of experiments. That is, at small values of  $V_r$  the dominant frequencies of vortex-shedding clustered around the driving frequency. As  $V_r$  increased to a certain value (depending on the magnitude of  $y_{rms}/D$ ), the frequencies clustered around the second multiple of the driving frequency. Figures. 5.32 to 5.36 show a few examples of the computed spectra for the thermistor signals at different  $\beta$  and  $y_{rms}/D$  values.

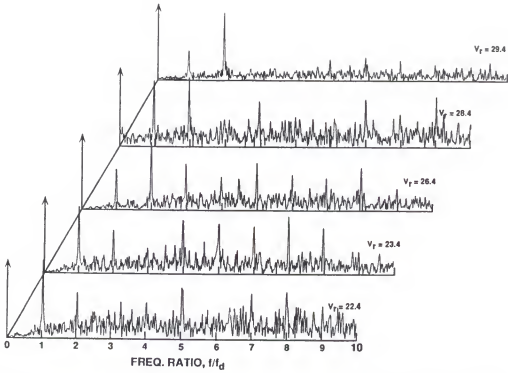


Figure 5.32: Thermistor power spectra at  $\beta = 14, 265$  and  $y_{rms}/D = 29.5\%$ .

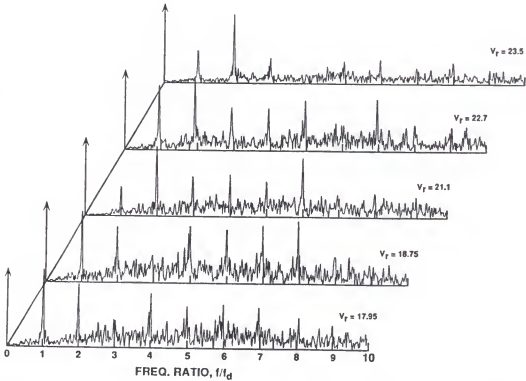


Figure 5.33: Thermistor power spectra at  $\beta = 14, 265$  and  $y_{rms}/D = 20.9\%$ .

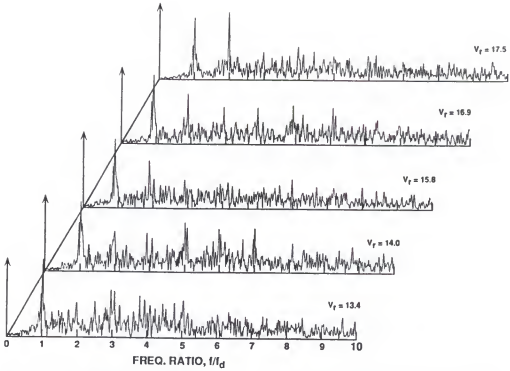


Figure 5.34: Thermistor power spectra at  $\beta = 14,265$  and  $y_{rms}/D = 8.2\%$ .

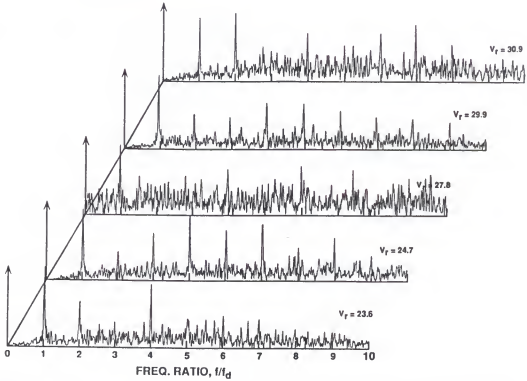


Figure 5.35: Thermistor power spectra at  $\beta = 16,260$  and  $y_{rms}/D = 16.8\%$ .

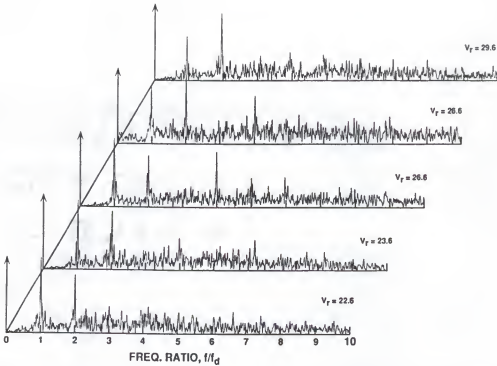


Figure 5.36: Thermistor power spectra at  $\beta = 16,260$  and  $y_{rms}/D = 8.8\%$ .

As shown in Figs. 5.32 to 5.36, the transverse motion ( $y_{rms}/D$ ) does affect the conditions under which the frequency of vortex-shedding shifts from the first multiple to the second multiple of the driving frequency.

To show the effect of transverse motion on the transition of vortex-shedding frequency, information from thermistor spectra was plotted (clustering ranges for different transverse motion amplitudes versus reduced velocity) as shown in Fig. 5.37. This figure shows that when  $y_{rms}/D = 8.2\%$ , and  $\beta = 14,265$ , the dominant frequencies cluster around the driving frequency, i.e.,  $N = f_v/f_d = 1$ . As  $V_r$  increases to 17.5,  $N$  shifts to 2. When  $y_{rms}/D = 20.9\%$ , the shift to  $N = 2$  occurred at  $V_r = 21.1$ . As  $y_{rms}/D$  increases further to 29.5% the shift to  $N = 2$  occurs at an even higher value of  $V_r$ , ( $V_r = 26.4$ ). The same trend was also observed for  $\beta = 16,260$  and for all other values of  $\beta$  tested. Consequently, for  $\beta > 14,265$ , the smaller the amplitude of the transverse motion ( $y_{rms}/D$ ) the smaller the value of  $V_r$  at which the shift occurs.

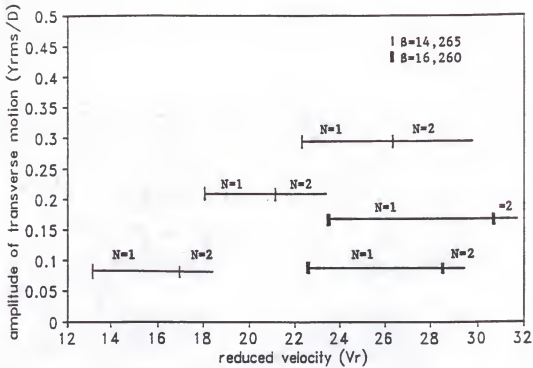


Figure 5.37: Schematic of the effect of transverse motion on the behavior of vortex-shedding frequency.

When  $6,500 < \beta < 14,265$ , the amplitudes of the transverse motion were larger than when  $\beta > 14,265$  for the same in-line  $KC$ . For this range of  $\beta$  it was found that the dominant frequencies of vortex-shedding did not cluster around the driving frequency at small values of  $V_r$  as they did for  $\beta > 14,265$ . Instead, they cluster around a higher multiple of the driving frequency, the value of which depends on the magnitudes of the transverse motion and  $\beta$ . For example, when  $y_{rms}/D$  was 56% and  $\beta = 5,400$ ,  $N$  was 3 at  $V_r = 4.6$  and remained at this value for the range of  $V_r$  tested, see Fig. 5.38. On the other hand when  $y_{rms}/D$  was 50% and  $\beta = 6,500$ ,  $N$  started at 3 at  $V_r = 6.6$ , then shifted to 4 as  $V_r$  increased to 7.7, see Fig. 5.39.

Examples of thermistor spectra for  $9,900 < \beta < 14,265$  are presented in Figs. 5.40 to 5.44. These figures show that  $N$  starts at 4 then shifts to higher values of  $N$  as  $V_r$  increases. This shift depends on the magnitude of the transverse motion and  $\beta$ . More data are needed before a complete explanation of this phenomenon can be given.

Preferably more than one type of instrumentation for measuring vortex-shedding frequency should be used. Perhaps pressure transducers along with thermistors could be employed. One possible explanation of the phenomenon described above might be as follows. An increase in  $V_r$  can be thought of as an increase in  $KC$  which for the articulated tower configuration represents an increase in the in-line motion amplitude. For a transversely constrained cylinder, the number of vortices shed during a cycle depends on the in-line motion amplitude. When the in-line motion is symmetric, as in the case for the experiments conducted in this study, the increase in the number of vortices shed would be expected to occur in steps of two. That is, as the in-line amplitude increases, one additional vortex would be shed per half cycle. When transverse motion is allowed, the vortex shedding process is altered by the transverse motion. In general, the transverse motion is not regular in the sense that many half cycles do not have the same amplitude as their adjacent half cycles. This could result in an uneven number of vortices being shed during a cycle of the in-line motion. This might explain the observed incrementing of vortices in steps of one.

Regardless of the value of  $N$  at which the dominant vortex-shedding frequencies cluster, the range of  $V_r$  over which these frequencies cluster at a particular value of  $N$  depends on the magnitude of transverse motion. This finding is similar in manner as for  $14,265 < \beta < 16,876$ . For example, as shown in Fig. 5.45 when  $y_{rms}/D$  was 16%,  $N$  shifted from 3 to 4 at  $V_r = 9.95$ . As  $y_{rms}/D$  increased to 28%,  $N$  shifted from 4 to 5 at  $V_r = 13.5$ , then to 6 at  $V_r = 14$ . As  $y_{rms}/D$  further increased to 35%, the shift from  $N = 4$  to 5 occurred at a higher value of  $V_r$ ,  $V_r = 15.6$ . The shift to  $N = 6$  then occurred at  $V_r = 16.15$ , which is higher than the corresponding  $V_r$  value when  $y_{rms}/D = 28\%$ . At  $y_{rms}/D = 40\%$  the range of clustering was even higher and so on. This general behavior was exhibited by the data for all the values of  $\beta$  tested. That is, for a constant  $\beta$  value, the smaller the transverse motion ( $y_{rms}/D$ ), the earlier the shift of vortex-shedding frequency to a higher multiple with respect to  $V_r$ .

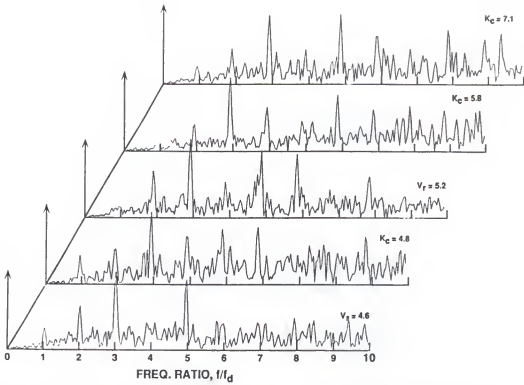


Figure 5.38: Thermistor power spectra at  $\beta = 5,400$  and  $y_{rms}/D = 56\%$ .

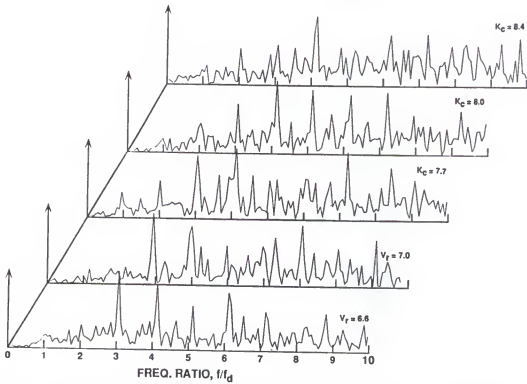


Figure 5.39: Thermistor power spectra at  $\beta = 6,500$  and  $y_{rms}/D = 50\%$ .

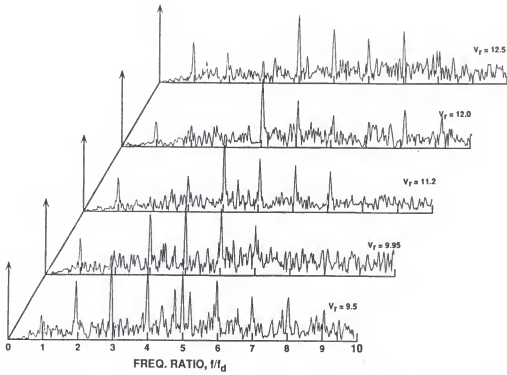


Figure 5.40: Thermistor power spectra at  $\beta = 9,900$  and  $y_{rms}/D = 16\%$ .

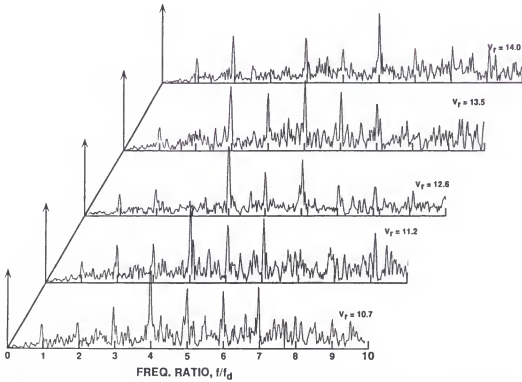


Figure 5.41: Thermistor power spectra at  $\beta = 9,900$  and  $y_{rms}/D = 28\%$ .



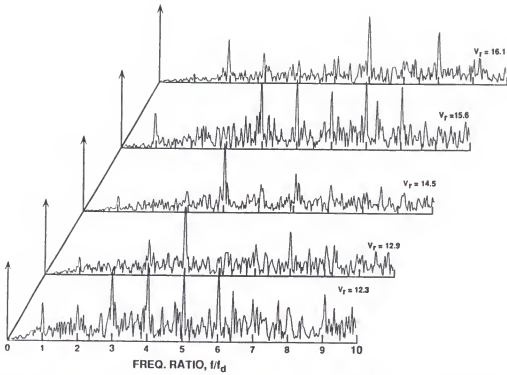


Figure 5.42: Thermistor power spectra at  $\beta = 9,900$  and  $y_{rms}/D = 35\%$ .

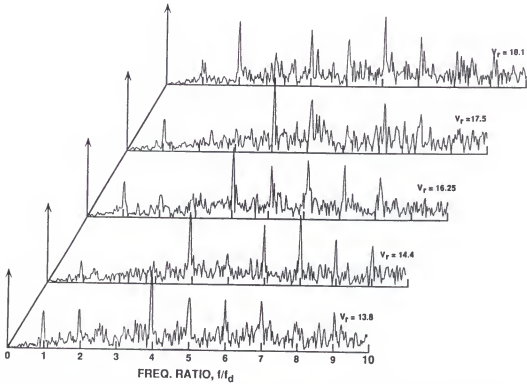


Figure 5.43: Thermistor power spectra at  $\beta = 9,900$  and  $y_{rms}/D = 40\%$ .

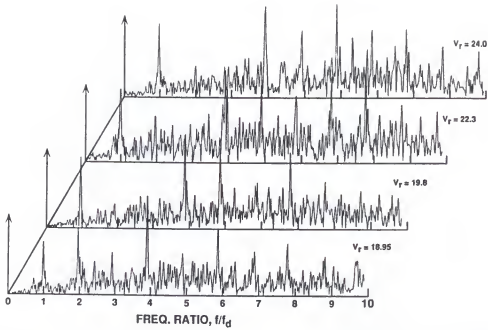


Figure 5.44: Thermistor power spectra at  $\beta = 12,500$  and  $y_{rms}/D = 33.5\%$ .

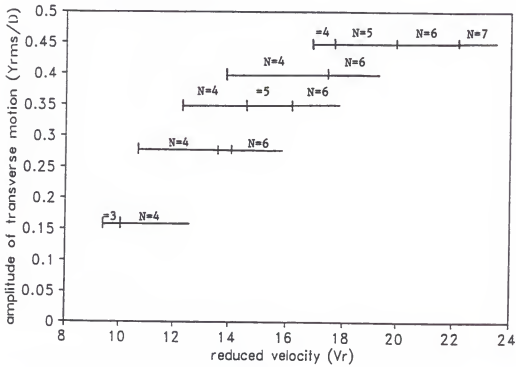


Figure 5.45: Schematic of vortex-shedding frequency behavior ( $\beta = 9,900$ ).

It must be pointed out that for  $6,500 < \beta < 14,265$ , when  $y_{rms}/D$  exceeded 35%, the dominant vortex-shedding frequencies were found to cluster at a value of  $N = 4$  for a larger range of  $V_r$ . This could reflect an improved correlation of the vortex-shedding along the cylinder due to the larger transverse motion which causes the vortices to be more regular. To gain more insight into this clustering behavior, the correlation coefficients  $\gamma_{xy}(f)$  (defined in Eqn. 5.2) between the top thermistor signal and each of the lower thermistors' signals were calculated. These correlation coefficients were then plotted against the vortex span-wise coherence length,  $z/D$ , as shown in Fig. 5.46 for all  $\beta$  values. As one can see from this figure, the vortices were highly correlated for all  $\beta$  values, but especially for  $\beta = 9,900$ , where the correlation coefficient was uniform over a longer length ( $z/D > 4$ ). This can explain why the frequency of vortex-shedding clustered at a value of  $N = 4$  for a larger range of  $V_r$  when  $\beta = 9,900$ . Compared to Fig. 5.25, where transverse motion was not allowed, Fig 5.46 shows that the vortices are strongly correlated over a wider range of  $\beta$  and the span-wise coherence length is larger when transverse motion is allowed.

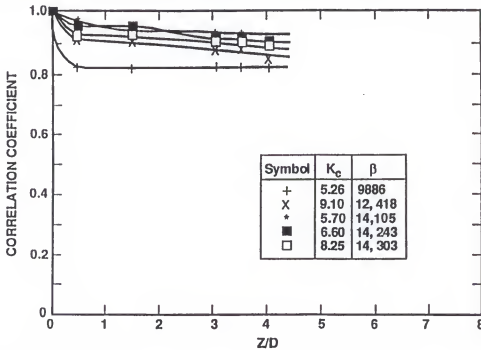


Figure 5.46: Span-wise coherence length for transversely unconstrained articulated tower.

The frequency of tower response,  $f_r$ , was obtained from the frequency analysis of the tower's transverse motion. This frequency ( $f_r$ ) was defined as the dominant peak in the response spectrum. The frequencies of these spectra were normalized by both the natural frequency of the system,  $f_n$ , and the driving frequency,  $f_d$ . The driving frequency was found to be the more meaningful frequency with which to normalize. These spectra were then plotted as groups with constant  $\beta$  but varying  $V_r$ . Figures. 5.47 to 5.51 show examples of these computed spectra for  $6,500 < \beta < 14,265$ . As shown in these figures, for the range of  $\beta$  values examined, the ratio  $f_r/f_d (\equiv M)$  always has a value of 1. The vortex-shedding frequency,  $f_v$ , was also higher than the tower's response frequency,  $f_r$ , and the natural frequency in still water,  $f_n$ . At the lower values of  $\beta$ , the tower response exhibited very little energy at its natural frequency. As  $\beta$  increased, the energy at the natural frequency increased until it reached its maximum value at  $\beta = 12,415$  and  $V_r = 30.3$  then decreased again. Under these conditions the energy at the natural frequency was about 75% of the energy at  $f_r/f_d = 1.0$ . Such behavior can be interpreted as follows. It is believed that very little energy is exhibited in the response spectra at the system's natural frequency for the following reason. At such a low value of  $f_n$  there was no vortex-shedding observed. It was also found from the first set of tests (constrained transverse motion) that as  $\beta$  increases, the transverse force increases until it becomes a maximum at a certain value of  $\beta$  called  $\beta_{cr}$  then decreases again, see Fig. 5.9. By analogy  $\beta = 12,415$  is  $\beta_{cr}$  for the case when transverse motion was allowed. Thus, this could explain the behavior of the energy exhibited in the response spectra at the natural frequency for  $\beta < 12,415$ , where the transverse force is very small. At  $\beta = 12,415$ , the transverse force is a maximum and therefore the energy in the response spectra is a maximum. Then, as  $\beta$  increases, the transverse force starts to decrease causing less energy in the response spectra.

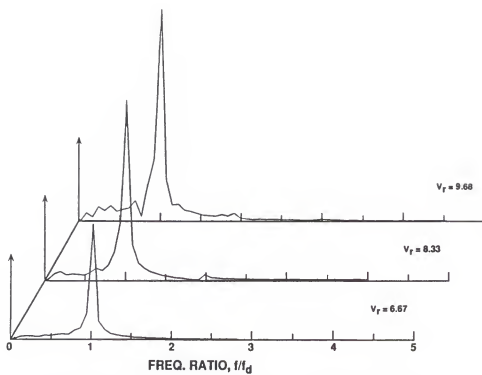


Figure 5.47: Transverse motion power spectra for  $\beta = 5,400$ .

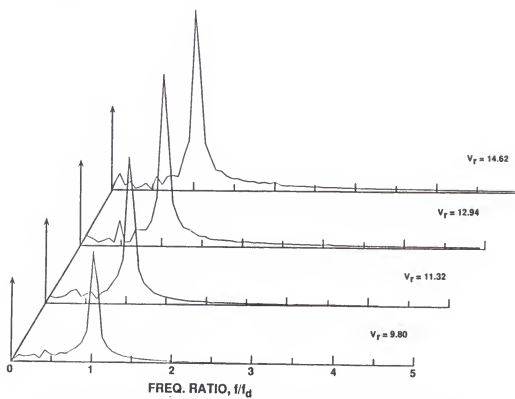


Figure 5.48: Transverse motion power spectra for  $\beta = 6,500$ .

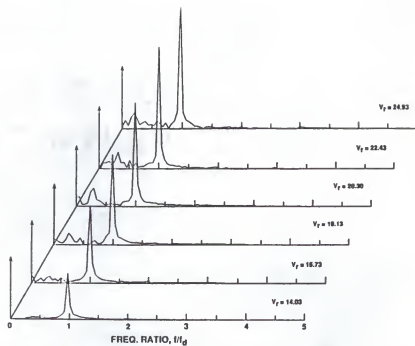


Figure 5.49: Transverse motion power spectra for  $\beta = 9,900$ .

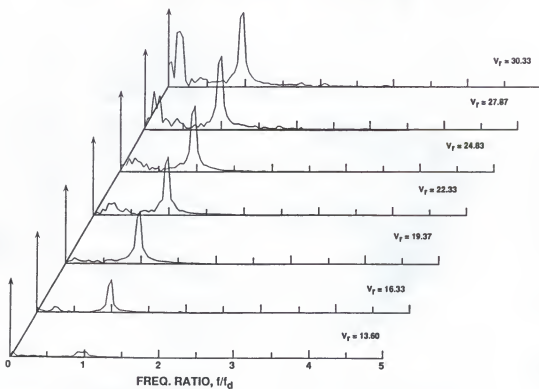


Figure 5.50: Transverse motion power spectra for  $\beta = 12,500$ .

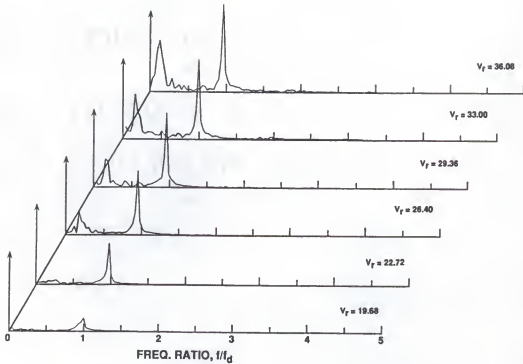


Figure 5.51: Transverse motion power spectra for  $\beta = 14, 265$ .

The response of a compliant structure is very much dependent on its natural frequency (i.e., the natural frequency of the fluid-structure system). Thus, at least indirectly, transverse forces are dependent on the natural frequency of the system. There was, however, no attempt made to examine these effects in this study, i.e., the system still water natural frequency (as defined below) remained unchanged during the course of experiments.

In this study, the system natural frequency was obtained by measuring the tower free oscillation in still water (see Fig. 5.52). The measured value compared well with the analytical expression given by

$$f_n = \frac{1}{2\pi} \sqrt{\frac{k_s}{(I_o + I'_a)}}, \quad (5.3)$$

where  $k_s$  is restoring moment coefficient due to weight and buoyancy of the tower,  $I_o$  and  $I'_a$  are the mass and added mass moment of inertia about the bottom hinge, respectively.

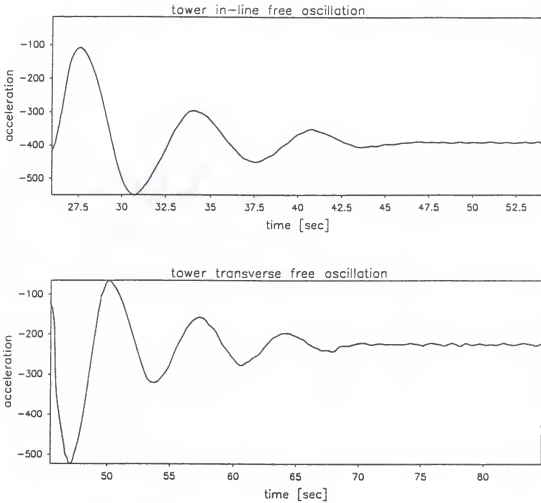


Figure 5.52: Tower measured free oscillation in still water.

The natural frequency of the system appeared to change with the operating conditions of the experiments. The reason for this apparent change was attributed to changes in the added mass. The “still water” natural frequency defined above was, however, used in analyzing the response and thermistor data.

It is believed that there should be a relationship between  $f_v$  and the other frequencies involved ( $f_r$ ,  $f_d$  and  $f_n$ ). The ratios of these frequencies were carefully examined using the information from the thermistor and response spectra at all values of  $\beta$  tested. It was found that at  $\beta = 5,400$  and  $y_{rms}/D = 56\%$  the ratios  $N$  and  $M$  are integers, more specifically  $N = 3$  and  $M = 1$ , see Figs. 5.38 and 5.47. Under these conditions the ratio  $f_v/f_n$  is also found to be an integer,  $f_v/f_n = 5$ .



Similar situations were also found to occur at  $\beta = 9,900$  and  $y_{rms}/D = 16\%$  and at  $\beta = 14,265$  and  $y_{rms}/D = 8.2\%$ . At  $\beta = 9,900$ , it was found that  $N = 4$ ,  $M = 1$  and  $f_v/f_n = 10$ , while at  $\beta = 14,265$ ,  $N = 1$ ,  $M = 1$  and  $f_v/f_n = 4$ .

It is known that in steady flow, when the natural frequency of the system is considerably greater than the frequency of vortex-shedding for a stationary cylinder, the cylinder has a very small response at the natural frequency. As the flow velocity is slowly increased, the frequency of vortex-shedding increases as does the cylinder amplitude at the natural frequency. This process continues until the amplitude takes control of the vortex-shedding frequency resulting in a maximum amplitude of oscillation. A further increase in the flow velocity causes the amplitude to decrease until eventually control of the shedding frequency by the transverse motion is lost. When the amplitude of the transverse motion is large enough to change the frequency of vortex-shedding to that of the response, "lock-in" occurs. This will happen when the flow speed is such that the stationary cylinder vortex-shedding frequency is in the neighborhood of the system natural frequency. In periodic flows the concept of lock-in also occurs. However, since there are usually more than a single stationary cylinder vortex-shedding frequency, the process is more complex. McConnell and Park (1982a,b) found that lock-in for uniform oscillatory flow occurs when the vortex-shedding frequency and the system's natural frequency are related to the fluid oscillating frequency in an integer manner. In their study this occurred when the  $f_r/f_n = f_v/f_n = 1$  and  $f_v/f_d = 6.22$  for  $4.4 < V_r < 6.6$ . This means that the natural frequency of their system was higher than the driving frequency. In the experiments conducted in this study, the natural frequency of the system was much lower than the driving frequency. This is usually the case for offshore structures.

To examine the lock-in condition for the experiments of this study, all combinations of the ratios of the frequencies involved were carefully evaluated for the cases where considerable transverse motion was excited at the natural frequency of the

system. In this study, this was found to occur at  $\beta = 14,265$  and lock-in was observed when  $f_r/f_n = f_v/f_n = 4$  and  $f_v/f_d = 1$ . This occurred over a wide range of  $V_r$  ( $22 < V_r < 36$ ), see Fig. 5.51 and Figs 5.32 to 5.34. In other words, the vortex-shedding frequency,  $f_v$ , changed to match the frequency of the tower response,  $f_r$ , which was one of the multiples of the system's natural frequency,  $f_n$ . Thus, in order to predict lock-in, one should know the stationary cylinder vortex-shedding frequency, system natural frequency, driving frequency, reduced velocity and the frequency parameter.

Transverse motion data obtained in this study were plotted as  $y_{rms}/D$  and  $y_{1/3}/D$  versus  $f_d/f_n$  for constant  $KC$ . The results presented in Fig. 5.53 show that the maximum transverse motion amplitude always occurs at a ratio of  $f_d/f_n = 1.67$  for all  $KC$  values. This means that the maximum transverse motion occurred at a driving frequency  $f_d = 0.25$  Hz. At this frequency, the ratios  $f_r/f_d$ ,  $f_v/f_n$ ,  $f_v/f_d$ , and  $f_v/f_r$  were always an integer for all  $KC$  values tested, in particular,  $f_r/f_d = 1$ ,  $f_v/f_n = 5$  and  $f_v/f_d = f_v/f_r = 3$ .

Knowing the range of the governing parameters at which transverse excitation is likely to occur is vital in both design and operation of offshore structures. The classification society's rules for the design and construction of offshore structures (such as Det Norske Veritas, DNV, 1982), recommend the use of  $V_r$  as a parameter to characterize this problem. For example, for steady flow, DNV rules recommend the consideration of vortex-shedding excitation when  $V_r > 3.5$ . For oscillatory flows and waves, the rules recommend that cross-flow excitations be considered when  $V_r \geq 1.0$ . The larger range of  $V_r$  designated for oscillatory flows indicates the uncertainties in this phenomenon and/or the lack of information for this type of flow. To gain more insight into this problem, the tower response due to vortex-shedding was examined with respect to the parameters controlling the excitation. The root-mean-square and the average of the highest 1/3 values of the transverse motion amplitudes ( $y_{rms}$  and

$y_{1/3}$ ), normalized by the tower's diameter  $D$ , were plotted in various ways such as  $y_{rms}/D$  and  $y_{1/3}/D$  versus  $KC$  while holding either  $R_e, \beta$ , or  $V_r$  constant. Plots of  $y_{rms}/D$  and  $y_{1/3}/D$  versus  $V_r, R_e$  and  $\beta$  while holding  $KC$  constant were also made. It was found that plots versus  $V_r$  with constant  $KC$ , as shown in Figs. 5.54 and 5.55, were the most meaningful. As noted from these figures, for any  $KC$  the amplitude of oscillation increases gradually as  $V_r$  increases and reaches a maximum when  $f_o/f_n$  approaches an integer then decreases again as  $V_r$  increases further. The maximum *rms* amplitude of oscillation ( $y_{rms}$ ) in the transverse direction due to vortex-shedding at the lowest  $KC$  ( $KC = 4.2$ ) was found to be about 30% of the cylinder's diameter. The corresponding  $y_{1/3}$  was about 50% $D$ . The results shown in Figs. 5.54 and 5.55 agree with the results of Sumer and Fredsøe (1988, 1989) for uniform oscillatory flow. The figures also demonstrate that, the larger the  $KC$ , the larger the value of  $V_r$  at which the maximum transverse motion occurs.

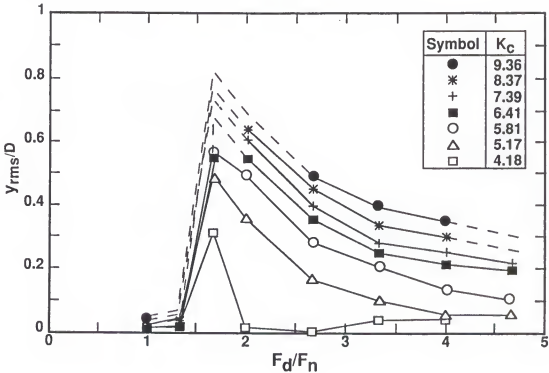


Figure 5.53: RMS transverse motion versus frequency ratio.

During the course of the experiments it was observed that, as  $KC$  increased, the amplitude of transverse oscillation increased until the cylinder hit the ends of the apparatus. This happened at  $KC = 5.8$ . At this point  $y_{rms}$  was about  $60\%D$  and the corresponding  $y_{1/3}$  was about  $90\%D$ . Beyond  $KC = 5.8$  and over a certain range of  $V_r$ , depending on the value of  $KC$ , the amplitude of transverse motion was larger than that allowed by the apparatus. The dotted lines in these figures, therefore, show extrapolated values of the response that would have occurred if a larger displacement had been allowed. Thus, the response amplitude, shown in Fig. 5.56, will reach a maximum then decrease displaying a peak similar to that obtained by Bearman and Hall (1987) for uniform oscillatory flow.

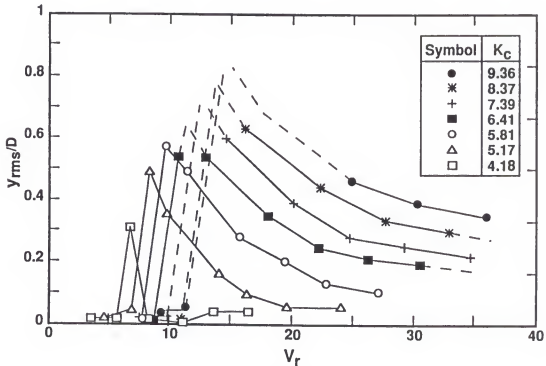


Figure 5.54: RMS transverse response versus reduced velocity.

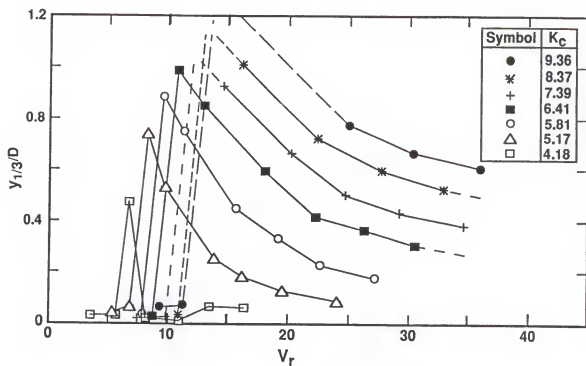


Figure 5.55: Average highest 1/3 transverse response versus reduced velocity.

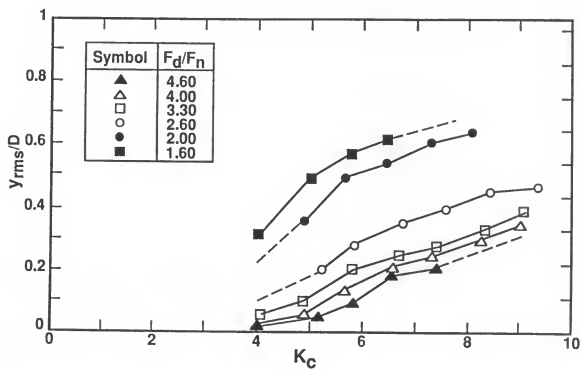


Figure 5.56: RMS transverse response versus Kuelegan-Carpenter number.

### 5.3 Sources of Uncertainty and Inaccuracy

The purpose of the experiments carried out in this study was to quantify the effect of flow nonuniformity and transverse motion on vortex-induced transverse loads and response. Although most of the data obtained from the experiments were well behaved, some displayed scatter. For example, the drag coefficient ( $C_D$ ) exhibits some scatter at lower  $R_e$  and  $KC$ , particularly for  $R_e$  around  $2 \times 10^4$  and  $KC < 6$ . There is also some scatter in the lift coefficient data for  $1,300 < \beta < 1,800$  and  $0.4 \times 10^4 < R_e < 1.6 \times 10^4$ .

From the physical insight gained from the results presented in this chapter, it is believed that, the variation of the velocity and thus  $R_e$  along the tower (that varies from zero at the bottom to some maximum at water surface) is the key to the scatter in some of the data. Some of the possible consequences of this nonuniformity are listed below:

1. The vortices can separate from the surface at different times along the tower. This results in phase differences between the vortices shed which would lead to a smaller correlation length.
2. Different flow regimes (subcritical, critical or even the postcritical) can exist along the tower at any given time. The transition from one regime to another is not only dependent on  $R_e$  but also on the conditions of the cylinder surface and motion as well. In these experiments, there were some changes in cylinder surface roughness over the duration of the experiments (due to the exposure of the aluminum cylinder to the chlorinated water for a period of approximately three months). Small vibrations were also present at the lower frequencies and amplitudes.

The scatter observed in some of the data can then be interpreted as resulting from any or all of these factors listed above.

Other possible sources of inaccuracies in the data include:

1. Errors introduced by the 12-bit A/D convertor which only had a resolution of 0.0025 volts. This results in a resolution of  $\pm 1.9$  mm for the in-line motion and  $\pm 1.0$  mm for the transverse motion measured. In terms of the moments measured, this is about  $\pm 0.004$  N.m for the in-line and  $\pm 0.005$  N.m for the transverse moment.
2. The input function for the in-line drive mechanism was  $x(t) = a \sin \omega_d t$ . This function rather than the measured motion was used in the analysis. Measurements of the actual motion were found to be slightly different than this function. These differences resulted from inaccuracies in the control system. The errors introduced by this procedure are estimated to be less than 2%.
3. In order to compute the tower's transverse velocity and acceleration, the results of measured transverse motion were numerically differentiated. After each differentiation the results had to be filtered to remove high frequency noise introduced by the numerical procedure. Errors were introduced in the results by the differentiation and filtering techniques. Higher order (4th to 10th) lowpass digital filters were used to minimize filter errors which are estimated to be less than 6%.

## CHAPTER 6 SUMMARY AND CONCLUSIONS

This chapter summarizes the most important observations made during the present investigation, draws conclusions from the findings and makes recommendations for future work.

### 6.1 Summary of the Results

This study revealed several interesting facts about the effect of flow nonuniformity on fluid-induced loading on fixed and compliant structures for  $6.1 \times 10^3 < R_e < 1.3 \times 10^5$ ,  $2.5 < KC < 9.5$  and  $3.1 < V_r < 46$ . Regarding in-line forces on compliant structures, flow nonuniformity was found to have a greater influence on the drag coefficient than on the added mass coefficients. The drag coefficient was less than that for the equivalent uniform oscillatory flow. Sarpkaya (1976a) and others showed that the vortex-induced forces in the in-line direction are a major factor influencing the drag force. The effect of flow nonuniformity on the vortex-shedding process probably accounts for the difference in the drag coefficients. However, both inertia and drag coefficients show clear dependency on  $R_e$  and  $KC$ . Inertia was the dominant component of the force for the range of  $R_e$  and  $KC$  attained in these experiments.

The transverse force data for the fixed tower identified a number of differences in the vortex-shedding behavior between uniform and nonuniform oscillatory flow. One difference is nonuniform oscillatory flow produces multiple frequencies of vortex-shedding. This is most likely due to the velocity variation along the tower which can cause the vortices to separate from the surface at different points in time. The dominant frequencies cluster around the driving frequency at lower values of  $KC$ . As  $KC$  increases to a certain value (depending on the value of  $\beta$ ) these frequencies shift



to a value twice the driving frequency. An explanation of this behavior was given in the previous chapter. Flow nonuniformity was also found to affect the magnitude of the lift coefficient and the span-wise coherence length. Both exhibited a maximum at a certain value of  $\beta$  referred to here as  $\beta$  critical or  $\beta_{cr}$ . In these experiments  $\beta_{cr}$  was found to be 2, 160. The magnitude of the lift coefficient was found to depend on both  $KC$  and  $R_e$  rather than just  $R_e$  as it is for steady flow, or just  $KC$  as it is for uniform oscillatory flow. For the range of  $KC$  tested, the lift coefficient data of these tests showed good agreement with data of other investigators for wave flows. The data suggest that the lift coefficient might exhibit a secondary peak around  $KC \simeq 2.5$ .

The model proposed for predicting the transverse force worked well for both the magnitude and frequency. When applied to the data from these experiments, this model showed that the magnitude of the transverse force ( $C_{L(n)}$ ) is deterministic and that the associated phase angle  $\phi_{(n)}$  is random in nature.

When the tower was allowed to respond freely in the transverse direction, interesting results on the effect of transverse motion were also found. The most pronounced effect was on the lift coefficient, frequency of vortex-shedding and vortex span-wise coherence length. The lift coefficients were increased by a factor of at least 2.5 due to the transverse motion. The transverse force was more regular than when transverse motion did not exist in that fewer harmonics (usually 2) were needed in the proposed model to produce the best fit to the measured data. This means that transverse motion reduces the irregularities in the transverse force by synchronizing the shedding along the length of the structure. Spectra for the thermistor data confirm this explanation. Regarding the frequency of vortex-shedding, the range over which the dominant frequencies cluster around the driving frequency (or one of its multiples) was found to depend on  $\beta$ ,  $V_r$ , and the amplitude of transverse motion rather than  $KC$  and  $\beta$  as for the cases when the tower is not allowed to have transverse motion. The vortex span-wise coherence length was found to be much larger for all values of

$\beta$  tested and its dependency on  $KC$  and  $\beta$  seems to not be influenced by the transverse motion. For the small values of  $\beta$  the energy of the response is much larger at the driving frequency than at the system's natural frequency. As  $\beta$  increased the energy at the natural frequency increased until it reached its maximum at a value of  $\beta = 12,415$ . At this value of  $\beta$ , lock-in occurred over a wide range of reduced velocity ( $22 < V_r < 36$ ) when the dominant frequency of vortex-shedding matched the response frequency and a multiple of the system natural frequency. As  $\beta$  increased further the amplitude started to decrease.

As explained before, the transverse motion increases the transverse force which in turn increases the transverse motion. This process continues until an equilibrium or ultimate state condition is reached for the given flow conditions. It is unfortunate that the apparatus used in these experiments did not allow the largest motion that could be induced due to vortex-shedding for the range of  $KC$  tested. The maximum  $y_{rms}$  measured was about  $0.6D$ , with a corresponding  $y_{1/3}$  of about  $0.95D$ . For the range of  $KC$  considered the results show that as  $KC$  increases, the maximum amplitude of transverse motion increases. Based on the results of other investigators, it is anticipated that these amplitudes will go through a maximum at approximately  $KC = 11$ .

## 6.2 Conclusions

This study started with an extensive literature review on the experimental investigations relevant to vortex-induced transverse loading on cylinders in water. The review revealed a lack of information and understanding of the effect of flow nonuniformity and three dimensionality on the vortex-shedding process, span-wise coherence length and the vortex-induced loading. Regardless of the type of flow there were almost no quantitative studies on the effect of structure transverse motion on the quantities mentioned above. The objectives of this study were thus 1) to gain insight into the effects of flow nonuniformity and transverse motion on vortex-induced

transverse loading through carefully planned laboratory experiments, 2) to formulate a better mathematical model for predicting transverse loads in oscillatory flows and 3) to produce lift coefficient data for a meaningful range of  $KC$  and  $R_e$ . A complete set of data on the lift coefficients when motion exists could not be obtained due to the lack of reliable values of  $C_m$  and  $C_D$  for the range of  $KC$  imposed by the transverse motion.

The study increased the data base for the hydrodynamic coefficients,  $C_D$  and  $C_m$  for ranges of  $KC$  and  $R_e$  where very little has been reported for either fixed or compliant structures. The results obtained in this study should be useful to the design of articulated mooring towers, risers, TLP tendons and other components of offshore structures.

During the course of this study, several facts emerged upon which the following conclusions may be drawn:

1. Oscillating an articulated cylinder in otherwise still water appears to be a reasonable technique for studying the effect of flow nonuniformity on flow-induced loadings.
2. The technique used for measuring frequency of vortex-shedding, i.e., miniature thermistors, was successful. The data obtained provided information on the vortex span-wise coherence length and the general vortex-shedding process for both transversely constrained and unconstrained cylinders.
3. The proposed model for predicting transverse forces is promising. The magnitude and frequency of the transverse force can be predicted to a reasonable degree of accuracy using this model.
4. Even though more data are needed before the effect of flow nonuniformity and transverse motion can be quantified for a wide range of  $KC$ ,  $R_e$  and  $V_r$ , progress on this problem has been made in this study. The results of this work cover

a range of  $KC$  from 2.5 to 9.5 and a range of  $R_e$  from  $6.1 \times 10^3$  to  $1.3 \times 10^5$  (ranges where very little data exists in the literature).

5. For the range of  $KC$  and  $R_e$  tested the in-line forces are inertia dominated.  $C_D$  is more dependent on flow nonuniformity than  $C_m$ . Both coefficients depend on  $R_e$  and  $KC$ .
6. The vortex-shedding process and the transverse forces for the two cases tested (transversely constrained and unconstrained) are remarkably different. For the constrained tower, the transverse force exhibits multiple frequencies. Its lift coefficients are deterministic and well behaved, while the associated phase angles appear to be random. The magnitude of the transverse force and the frequency of vortex-shedding depend on  $KC$  and  $\beta$ . The largest value of the lift coefficient (for the range of  $KC$  tested) occurs at the in-line driving frequency.
7. For the transversely constrained tower there appears to be a "critical" frequency parameter ( $\beta_{cr}$ ) where the transverse force peaks. Thermistor data show a maximum vortex span-wise coherence length at this value. In this study the critical value of  $\beta$  is 2,160.
8. Transverse motion reduces irregularities in the transverse force and provides a means of synchronizing the vortex-shedding along the length of the tower. Fewer harmonics in the proposed model are needed to predict the transverse force when motion is allowed.
9. Transverse motion significantly increases the value of the lift coefficients. In this study, the lift coefficient was at least 2.5 times larger than that for the constrained tower under the same environmental conditions. Lift coefficients obtained for constrained towers underpredict vortex-induced response by at least 40%. The calculated response using constrained tower lift coefficients is also more irregular than that measured.

10. Transverse motion influences the frequency of vortex-shedding and the vortex span-wise coherence length. The frequency of vortex-shedding and the range over which the dominant frequencies cluster about a particular frequency depends on  $V_r$ ,  $\beta$  and the amplitude of transverse motion. The vortex span-wise coherence length is much larger when transverse motion exists.
11. Lock-in occurs when the amplitude of the transverse response at the system natural frequency is large enough to control the shedding process. In this case the dominant frequencies of vortex-shedding are close to the natural frequency (or one of its multiples).
12. The amplitude of transverse motion depends on  $V_r$  and  $KC$ . Maximum transverse motion due to vortex-shedding occurs when  $KC > 4$  and  $V_r > 6.5$ . As  $KC$  increases the amplitude of maximum response increases and the value of  $V_r$  at which this maximum occurs also increases.
13. The force coefficients obtained from oscillating an articulated tower in still water agree well with the results of other investigators for waves on fixed cylinders.

### 6.3 Recommendations for Further Work

This study introduced a new method for measuring frequency of vortex-shedding; proposed an improved model for calculating vortex-induced transverse forces; and answered some of the questions concerning the effects of flow nonuniformity and structure transverse motion on the vortex-shedding process, the transverse loading and the vortex span-wise coherence length. The problem; however, is by no means solved and additional work is needed.

A major uncertainty is in the mechanism that determines the phase of the vortex-induced transverse force. This needs to be investigated further and a methodology developed for dealing with its seemingly random behavior. In addition, tests similar to those conducted here need to be performed for a wider range of  $KC$  and  $Re$ . More

specifically the range of  $KC$  between 1.5 and 20 and  $R_e$  between  $10^4$  and  $2 \times 10^6$ . The influence of in-line motion on transverse forces and vortex span-wise coherence length needs to be included for the same range of  $KC$  and  $R_e$ . Drag and inertia coefficients for the low values of  $KC$  and  $R_e$  existing for transverse motion need to be measured. The effect of different system natural frequencies on the lock-in phenomenon should also be examined. Finally, the effects of surface roughness on all of the above quantities is needed.

Fluid-structure interaction problems are complex and difficult to solve. In spite of the research conducted and progress made in recent years in vortex-induced loading, many questions remain unanswered. Problems associated with the phase of the transverse force are tied to flow instabilities which are very sensitive to even minor changes in the flow and in structure surface conditions. The phase angle may thus have to be treated as a random phenomenon for some time to come.

It is hoped that the results of this study will provide some insight into the complex mechanisms involved and that the data obtained will be useful to design engineers.

## APPENDIX A ANALYSIS TECHNIQUES

### A.1 Formulation of Dimensionless Parameters

When an articulated tower is allowed to have transverse motion, the transverse force and response are interdependent. To study the effect of this motion and other parameters on the vortex-induced transverse loading and response, the equation of motion is investigated. The general form of this equation can be written as

$$I_m \ddot{\theta}(t) + C_s \dot{\theta}(t) + \beta_h \dot{\theta}(t) |\dot{\theta}(t)| + k_s \theta(t) = M_L(t) \quad (\text{A.1})$$

where,

$$I_m = I_o + I'_a,$$

$$I_o = \text{mass moment of inertia about bottom hinge,}$$

$$I'_a = \text{added mass moment of inertia about bottom hinge,}$$

$$\theta(t) = \text{angle of transverse oscillation,}$$

$$C_s = \text{structural damping coefficient,}$$

$$\beta_h = \text{hydrodynamic damping coefficient,}$$

$$= \int_0^{\ell_s} \frac{1}{2} \rho_w C_D D r^3 dr = \frac{1}{8} \rho_w C_D D \ell_s^4, \quad (\text{A.2})$$

$$C_D = \text{drag coefficient,}$$

$$k_s = \text{restoring moment coefficient due to buoyancy and weight,}$$

$$M_L(t) = \text{moment due to lift force about bottom hinge,}$$

$$= \sum_{n=1}^N M_o C_{Ln} e^{i[\psi(n) - n\sigma t]}, \quad (\text{A.3})$$

$$M_o = \text{components of the moment at in-line flow frequencies } n\sigma \text{ and}$$

$$= \int_0^{\ell_s} \frac{1}{2} \rho_w D U^2 r dr = \frac{1}{4} \rho_w D U^2 \ell_s^2. \quad (\text{A.4})$$

If the nonlinear drag term is linearized with respect to time, a solution of the form

$$\theta(t) = \sum_{n=1}^N \theta_o(n) e^{i[\phi(n) - n\sigma t]}, \quad (\text{A.5})$$

can be assumed. Thus, substituting Eqn. A.5 into Eqn. A.1 and eliminating the time function,  $e^{-in\sigma t}$ , result in,

$$\theta_o(n) e^{i\phi(n)} = \frac{M_o e^{i\psi(n)}}{[k_s - I_t(n\sigma)^2] - i(n\sigma)[\lambda_e + C_s]}, \quad n = 1, 2, \dots, N. \quad (\text{A.6})$$

where,  $\lambda_e$  is the integral over the length  $\ell_s$  and is a function of  $\theta_o$  and  $\phi(n)$ . Further it can be assumed, without loss of any generality, that  $\lambda_e$  is negligibly small, then the magnitude of the transverse oscillation becomes:

$$\theta_o(n) = \frac{M_o/I_t}{\{[\omega^2 - (n\sigma)^2]^2 + [2\beta_h\omega(n\sigma)]^2\}^{\frac{1}{2}}}. \quad (\text{A.7})$$

The phase angle with reference to the in-line flow is

$$\phi(n) = \psi(n) + \tan^{-1} \left[ \frac{2\beta_h\omega(n\sigma)}{\omega^2 - (n\sigma)^2} \right] \quad (\text{A.8})$$

where  $\omega = 2\pi f_n = \sqrt{(k_s/I_t)}$ .

If  $I_t = I_o + I_a \simeq (m_s + m_a)\ell^2/3$ , then substituting this expression along with Eqn. A.4 into Eqn. A.7 gives

$$\theta_o(n) = \frac{\frac{1}{4} \rho_w \sum_{n=1}^N C_{Ln} D U^2 \ell_s^2 / m_s (1 + m_a/m_s) \ell^2 / 3}{\{[\omega^2 - (n\sigma)^2]^2 + [2\beta_h\omega(n\sigma)]^2\}^{\frac{1}{2}}}. \quad (\text{A.9})$$

Also, if  $\theta_o(n) \simeq y/\ell$ , then Eqn. A.9 reduces to

$$y/\ell = \frac{\frac{1}{4} \rho_w D (U/D f_n)^2 D^2 \ell_s^2 \sum_{n=1}^N C_{Ln}}{(4 \pi^2 \ell^2 / 3 \omega^2) m_s (1 + m_a/m_s) \{[\omega^2 - (n\sigma)^2]^2 + [2\beta_h\omega(n\sigma)]^2\}^{\frac{1}{2}}}. \quad (\text{A.10})$$

Since  $U/D f_n = V_r$ ,

$$y/D = \frac{3 \rho_w \ell V_r^2 D^2 \ell_s^2 \sum_{n=1}^N C_{Ln}}{16 \pi^2 m_s (1 + m_a/m_s) \ell^2 \{[1 - (n\sigma/\omega)^2]^2 + [2\beta_h(n\sigma/\omega)]^2\}^{\frac{1}{2}}}. \quad (\text{A.11})$$

Further, if  $\ell_s = d/\cos \theta$  is approximated by  $\ell$  then Eqn. A.11 reduces to

$$y/D \simeq \frac{3 \rho_w \ell V_r^2 D^2 \sum_{n=1}^N C_{Ln}}{16 \pi^2 m_s (1 + m_a/m_s) \{[1 - (n\sigma/\omega)^2]^2 + [2\beta_h(n\sigma/\omega)]^2\}^{\frac{1}{2}}}. \quad (\text{A.12})$$



Introducing the critical damping factor  $\xi$  in water:

$$\xi = \beta_h = \frac{C_s}{2I_t \omega} \quad (\text{A.13})$$

where  $\delta = 2\pi\xi$  is the logarithmic decrement of free oscillation in still water. Then, at the lock-in condition (where  $n\sigma = \omega$ ) Eqn. A.12 reduces to

$$y/D \simeq \frac{3\rho_w \ell V_r^2 D^2 \sum_{n=1}^N C_{Ln}}{16\pi \delta m_s (1 + m_a/m_s)}. \quad (\text{A.14})$$

The stability parameter is defined as

$$K_s = \frac{2m_s \delta / \ell}{\rho_w D^2}. \quad (\text{A.15})$$

Then with the dominant lift coefficient  $C_L \simeq C_{Ln}$ , Eqn. A.14 becomes

$$y/D \simeq \frac{3V_r^2 C_L}{8\pi K_s (1 + m_a/m_s)}. \quad (\text{A.16})$$

## A.2 Runge-Kutta Numerical Solution

In quantifying the effect of transverse motion on transverse forces, Runge-Kutta numerical technique was used to solve Eqn. 4.54. For this technique, the dynamic equations are transformed into two first order differential equations:

$$\frac{dY}{dt} = f(t, Y, \dot{Y}), \quad \text{and} \quad (\text{A.17})$$

$$\frac{d\dot{Y}}{dt} = g(t, Y, \dot{Y}), \quad (\text{A.18})$$

where  $\dot{Y} \equiv \frac{dY}{dt}$ . The function  $g \equiv \frac{1}{I_t} \sum M_{\text{applied}}$  where the applied moments have been described previously in Eqns. 4.50 to 4.52. The function  $f$  is simply  $f \equiv \dot{Y}$ . The two fundamental dependent variables  $Y$  and  $\dot{Y}$  are extrapolated from the  $j^{\text{th}}$  time step to the next step according to

$$Y_{j+1} = Y_j \left( \frac{d\bar{Y}}{dt} \right) \delta t, \quad \text{and} \quad (\text{A.19})$$

$$\dot{Y}_{j+1} = \dot{Y}_j + \left( \frac{d\bar{\dot{Y}}}{dt} \right) \delta t, \quad (\text{A.20})$$

where

$$\frac{d\bar{Y}}{dt} = \frac{1}{6} (K_0 + 2K_1 + 2K_2 + K_3), \quad \text{and} \quad (\text{A.21})$$

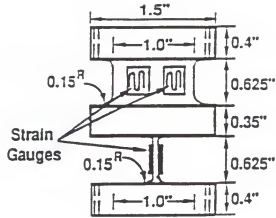
$$\frac{d\bar{Y}}{dt} = \frac{1}{6} (m_0 + 2m_1 + 2m_2 + m_3), \quad (\text{A.22})$$

where, according to the Runge-Kutta theory,

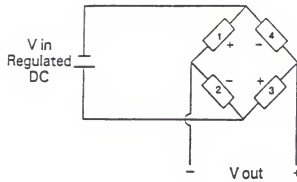
$$\begin{aligned} K_0 &= f(t_j, Y_j, \dot{Y}_j), \\ K_1 &= f\left(t_j + \frac{\delta t}{2}, Y_j + K_0 \frac{\delta t}{2}, \dot{Y}_j + m_0 \frac{\delta t}{2}\right), \\ K_2 &= f\left(t_j + \frac{\delta t}{2}, Y_j + K_1 \frac{\delta t}{2}, \dot{Y}_j + m_1 \frac{\delta t}{2}\right), \\ K_3 &= f(t_j + \delta t, Y_j + K_2 \delta t, \dot{Y}_j + m_2 \delta t), \\ m_0 &= g(t_j, Y_j, \dot{Y}_j), \\ m_1 &= g\left(t_j + \frac{\delta t}{2}, Y_j + K_0 \frac{\delta t}{2}, \dot{Y}_j + m_0 \frac{\delta t}{2}\right), \\ m_2 &= g\left(t_j + \frac{\delta t}{2}, Y_j + K_1 \frac{\delta t}{2}, \dot{Y}_j + m_1 \frac{\delta t}{2}\right), \quad \text{and} \\ m_3 &= g(t_j + \delta t, Y_j + K_2 \delta t, \dot{Y}_j + m_2 \delta t). \end{aligned}$$

## APPENDIX B INSTRUMENTATION AND CALIBRATION DATA

In this appendix, the instrumentations used in these experiments are presented along with pertinent calibration data.



**Force Transducer**



**Wheatstone Bridge**

Figure B.1: X-Y force transducer and wheatstone bridge circuit.

Table B.1: Specifications of strain gauge amplifier/signal conditioning module.

item	
gain range	10-200
gain range with external R	10-1000
gain temp. coefficient	3 ppm/°C
drift (RTI)	$2 \pm \frac{20}{G} \mu V/^\circ C$
input bias current	30 nA
input impedance:differential	3000
input noise (RTO) at gain = 100	1 – 100 Hz : 120 $\mu V_{RMS}$

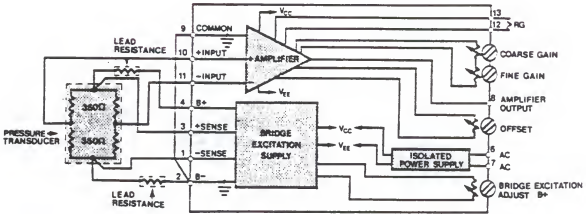


Figure B.2: Schematic of strain gauge amplifier/signal conditioning module.

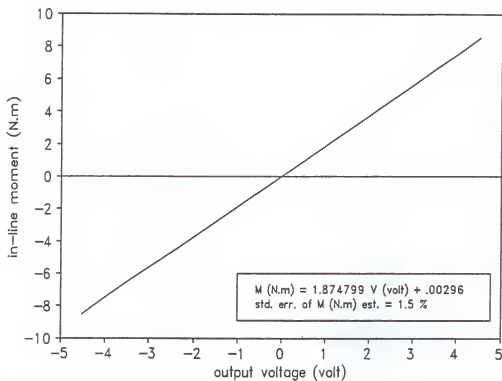


Figure B.3: Calibration curve for in-line force (for test runs at  $0.4 \geq f_d \leq 0.8 \text{ Hz.}$ ).

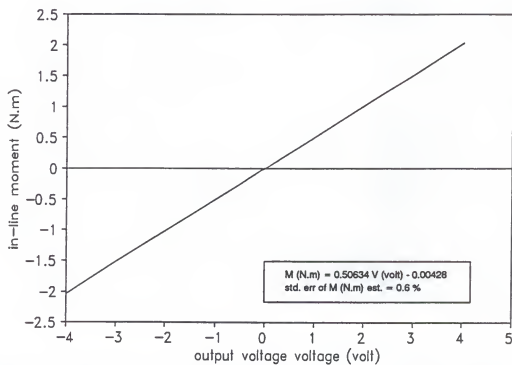


Figure B.4: Calibration curve for in-line force (for test runs at  $0.15 \geq f_d \leq 0.3 \text{ Hz.}$ ).

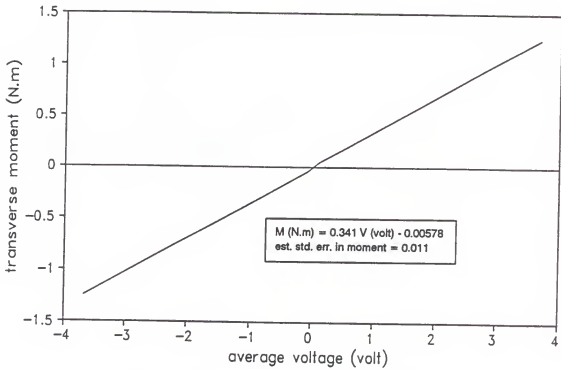


Figure B.5: Calibration curve for transverse force.

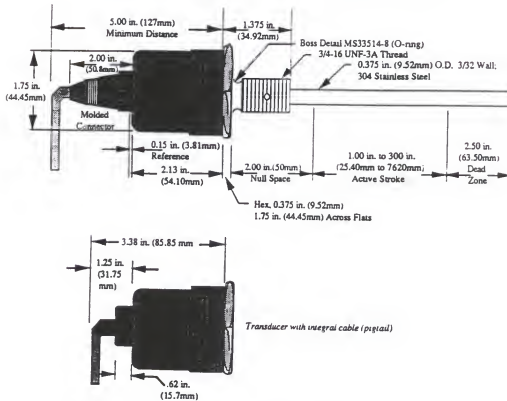


Figure B.6: Standard rigid linear displacement transducer.

Table B.2: Linear displacement transducer specifications.

<b>Input Voltage</b>	$\pm 12\text{Vdc}$ to $\pm 15\text{Vdc}$
<b>Current Draw</b>	$\pm 15\text{Vdc}$ @ 100mA maximum, 25mA minimum (current draw varies with magnet position, maximum draw occurs when magnet is 2 in. (50 mm) from the flange and minimum update time is being utilized).
<b>Null Space</b>	Null space will be 2 in. if the stroke length is stated in inches and 50 mm if the stroke length is stated in millimeters.
<b>Displacement</b>	Up to 25 ft. (7620 mm)
<b>Dead Space</b>	2.5 in. (63.5 mm)
<b>Head Enclosure</b>	2.13 in. (54.10 mm) high with 1.75 in. (44.45 mm) dia.; NEMA 6
<b>Nonlinearity</b>	< 0.05% of full stroke; minimum of $\pm 0.002$ in. ( $\pm 0.05$ mm)
<b>Repeatability</b>	< 0.001% of full stroke or $\pm 0.0001$ in. ( $\pm 0.0025$ mm), whichever is greater
<b>Hysteresis</b>	0.0008 in. (0.02 mm) maximum
<b>Frequency Response</b>	Stroke dependent, 200Hz to 50Hz is typical for lengths of 12 in. (304.8 mm) to 100 in. (2540 mm) respectively. Wider response is available.
<b>Temperature Coefficient</b>	less than 0.00011 in./°F + [3ppm/°F per in. of full stroke] (less than .005mm/°C + [0.21ppm/°C per mm of full stroke])
<b>Operating Temperature Transducer Rod Head Electronics</b>	-40 to 185°F (-40 to 85°C) -40 to 150°F (-40 to 66°C)
<b>Operating Pressure</b>	FM certified to 3000psi continuous; 8000psi static
<b>Output Impedance</b>	10 $\Omega$



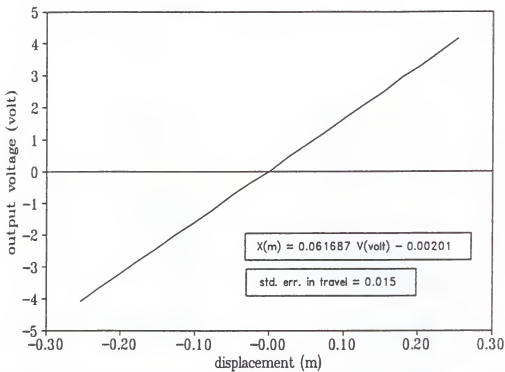


Figure B.7: Calibration curve of in-line linear displacement transducer.

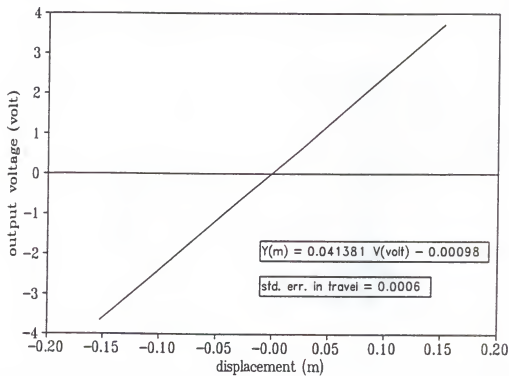


Figure B.8: Calibration curve of transverse linear displacement transducer.

Table B.3: Thermistor specifications.

item	FP07
maximum diameter (D)	2.15 mm
length (L)	12.5 mm
thermal time constant (in still air)	0.1 sec
thermal time constant (water plunge)	7 msec
dissipation constant (in still air)	0.05 mW/°C
dissipation constant (in still water)	0.25 mW/°C
maximum power rating	.006 watts
resistance range (ohms)	1 K – 10 M

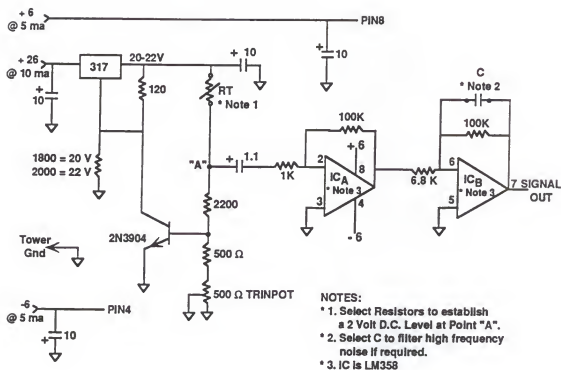


Figure B.9: Schematic of thermistor signal processing circuit.

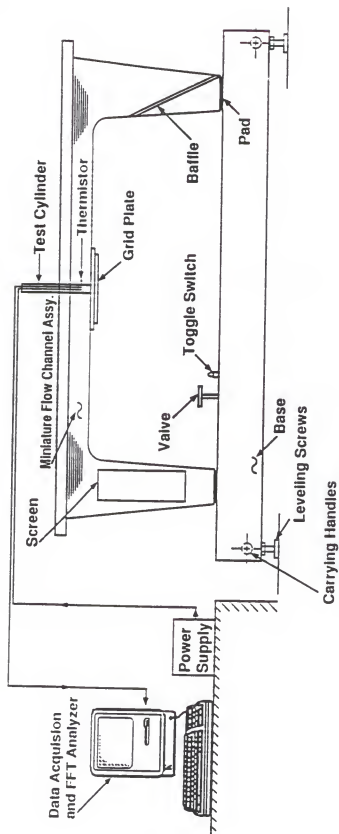


Figure B.10: Schematic of thermistor testing set-up using flow visualization table.

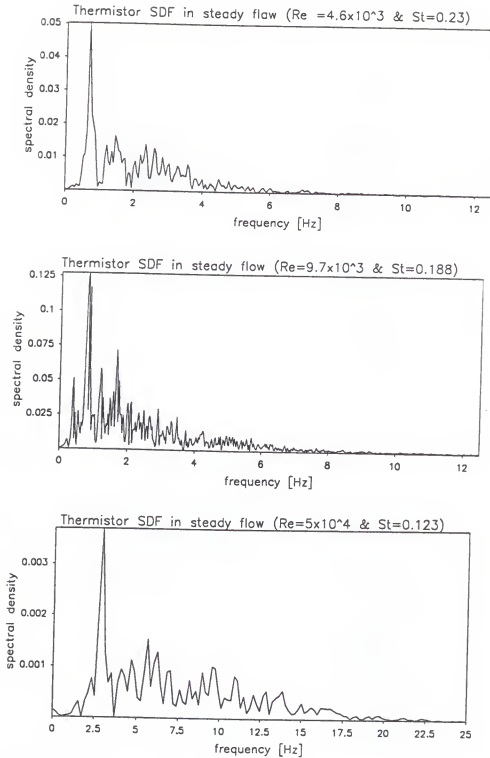


Figure B.11: Thermistor signal power spectra at various Reynolds numbers.

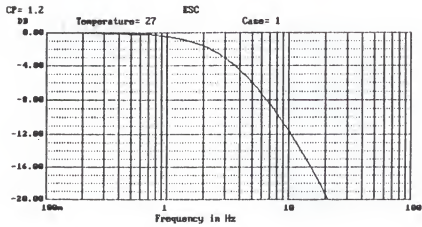
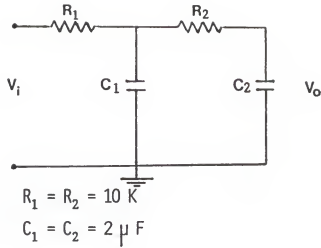


Figure B.12: Schematic diagram and frequency response for second order, passive, Butterworth lowpass filter circuit (designed for the feed back control signal).

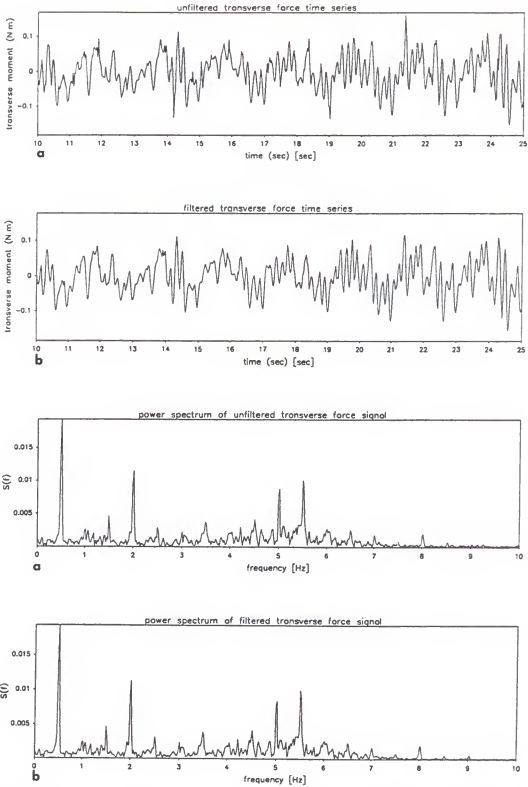


Figure B.13: Samples of transverse force signals and their corresponding power spectra (a) before filtering (b) after filtering.

Table B.4: Linear drive motor specifications.

motor width $XY$	units	45
force constant ( $K_p$ )	lbs/amp	5.2
continuous force ( $F_c$ )	lbs	26
force at 50% D.C. ( $F_m$ )	lbs	37
force at 10% D.C. ( $F_p$ )	lbs	82
continuous current ( $I_c$ )	amps	5.1
current at 50% D.C. ( $I_m$ )	amps	7.1
current at 10% D.C. ( $I_p$ )	amps	16
volts for $F_c$ at 10 <i>inch/sec</i>	VDC	28
volts for $F_c$ at 20 <i>inch/sec</i>	VDC	34
volts for $F_c$ at 30 <i>inch/sec</i>	VDC	40
volts for $F_p$ at 10 <i>inch/sec</i>	VDC	76
volts for $F_p$ at 20 <i>inch/sec</i>	VDC	81
volts for $F_p$ at 30 <i>inch/sec</i>	VDC	87
back EMF $K_e$	V/inch/sec	.59
resistance at 20 C $R_c$	ohms	2.7
resistance at 180 C $R_f$	ohms	4.4
inductance $L$	mhenry	7.1
time constant T at 20 C	msec	2.6
magnetic attraction	lbs	270

## APPENDIX C FLOW CHARTS OF THE VARIOUS COMPUTER PROGRAMS

In this appendix, the flow charts of the various computer programs written to analyze the experimental data are presented.



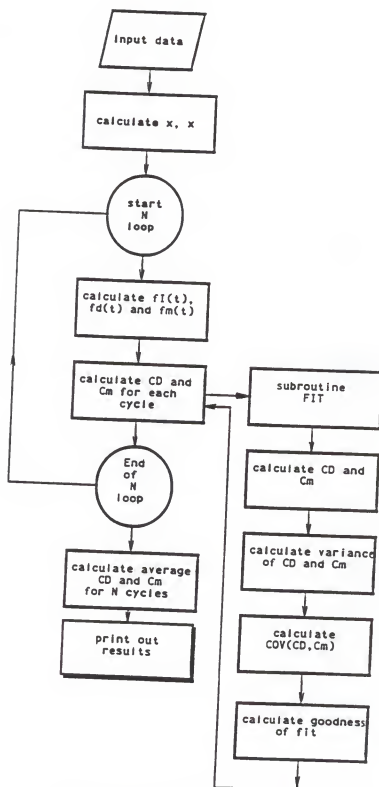


Figure C.1: Computer code flow chart for CD and Cm.

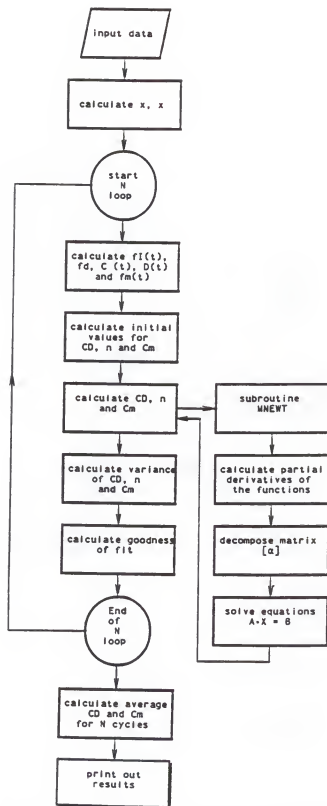


Figure C.2: Computer code flow chart for CDCMN.

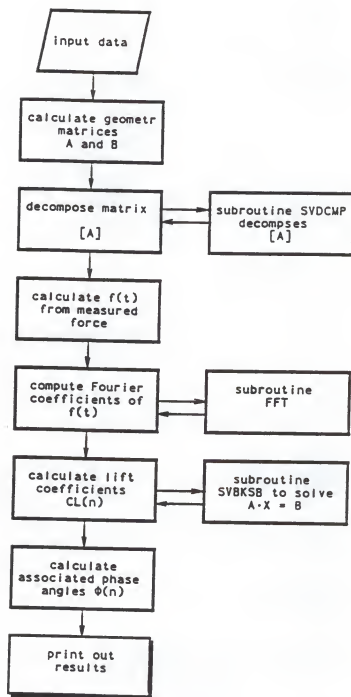


Figure C.3: Computer code flow chart for CLEF.

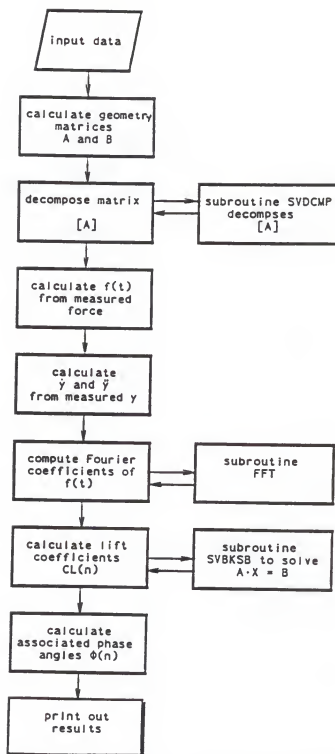


Figure C.4: Computer code flow chart for CLEUF.

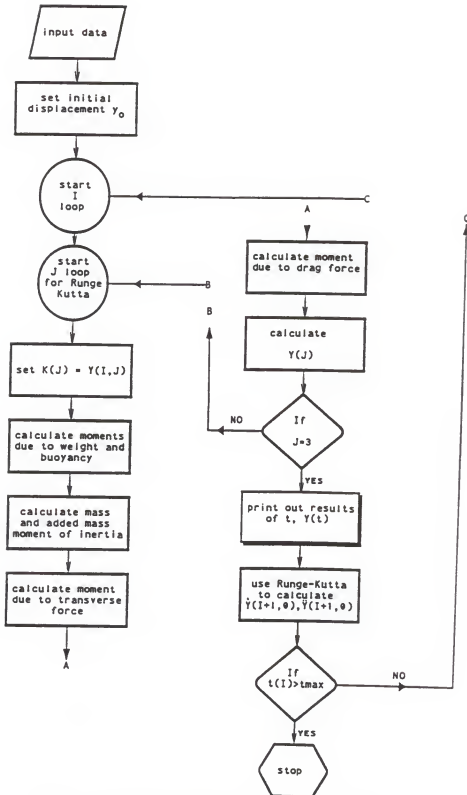


Figure C.5: Computer code flow chart for ATVSR.

## BIBLIOGRAPHY<sup>1</sup>

- [1] Achenbach, E. and E. Heinecke (1981), "On Vortex Shedding From Smooth and Rough Cylinders in the Range of Reynolds Numbers  $6 \times 10^3$  to  $5 \times 10^6$ ." *J. of Fluid Mech.*, V.109, 239-251.
- [2] Bearman, P.W. (1984), "Vortex Shedding from Oscillating Bluff Bodies." *Ann. Rev. Fluid Mech.*, V.16, 195-222.
- [3] Bearman, P.W. (1988a), "Flow Around Circular Cylinders at High Reynolds Numbers in Steady Flow and Waves." *Proc. of an Intern. Conf., Technology Common to Aero and Marine Engineering*, The Society of Underwater Technology, London, UK., 119-127.
- [4] Bearman, P.W. (1988b), "Wave Loading Experiments on Circular Cylinders at Large Scale." *Proc. of the Intern. Conf on Behaviour of Offshore Structures*, V.2, 471-487.
- [5] Bearman, P.W., J.R. Chaplin, J.M.R. Graham, J.K. Kostense, P.F. Hall and G. Klopman (1985), "The Loading on a Cylinder in Post-Critical Flow Beneath Periodic and Random Waves." *Proc. of the Intern. Conf. on Behavior of Offshore Structures*, 213-225.
- [6] Bearman, P.W., J.M.R. Graham, P. Naylor and E.D. Obasaju (1981), "The Role Of Vortices in Oscillatory Flow About Bluff Cylinders." *International Symposium On Hydrodynamics in Ocean Engineering*, Norwegian Inst. of Tech., 621-626.
- [7] Bearman, P.W., J.M.R. Graham and E.D. Obasaju (1984), "A Model Equation for the Transverse Forces on Cylinders in Oscillatory Flows." *Applied Ocean Research*, V.6, No.3, 166-172.
- [8] Bearman, P.W. and P.F. Hall (1987), "Dynamic Response of Circular Cylinders in Oscillatory Flow and Waves." *Intern. Conf. on Flow Induced Vibrations*, England, Paper No.D6, 183-190.
- [9] Bidde, D.D. (1971), "Laboratory Study of Lift Forces on Circular Piles." *Waterways, Harbors and Coastal Engineering Division*, *Proc. of the ASCE*, V.97, No.WW4, Paper No.8495, 595-614.
- [10] Blevins, R.D. (1990) *Flow Induced Vibration*, New York, N.Y., Van Nostrand Reinhold, Co.
- [11] Chakrabarti, S.K. and D.C. Cotter (1984), "Hydrodynamic Coefficients of a Mooring Tower." *J. of Energy Resources Tech.*, V.106, 183-190.

---

<sup>1</sup>Figures and tables in Chapter 2 refer to references by number

- [12] Chakrabarti, S.K., D.C. Cotter and A.R. Libby (1983), "Hydrodynamic Coefficients of a Harmonically Oscillated Tower." *Applied Ocean Research*, V.5, No.4, 226-233.
- [13] Chakrabarti, S.K., A.L. Wolbert and W.A. Tam (1976), "Wave Forces on Vertical Circular Cylinder." *J. of the Waterways, Harbors and Coastal Eng. Div.*, No.WW2, 203-221.
- [14] Chen, S.S. (1987) *Flow-Induced Vibration of Circular Cylindrical Structures*, New York, Hemisphere Publishing Corp., Springer-Verlag, Chap. 7.
- [15] Dean, R.G. (1976), "Methodology For Evaluating Suitability Of Wave and Wave Force Data For Determining Drag and Inertia Coefficients." *Proc. of the Intern. Conf. on Behaviour of Offshore Structures*, V.2, 40-64.
- [16] Det Norske Veritas (1982), "Rules for the Design, Construction and Inspection of Offshore Structures, Appendix-B."
- [17] Demirebilek, Z., and T. Halvorsen (1985), "Hydrodynamic Forces on Multitube Production Risers Exposed to Currents and Waves." *J. of Energy Resources Tech.*, V.107, 226-234.
- [18] Donazzi, F., G. Diana, M. Falco and P. Guoxun (1981), "Induced Oscillation on a Cylinder at High Reynolds Number Due to the Vortex Shedding." Intern. Symp. on Hydrodynamics in Ocean Engineering, The Norwegian Inst. of Tech., Trondheim, 307-325.
- [19] Dronkers, M.E.L. and W.W. Massie (1978), "Lift Forces on Circular Cylinders." The Symp. on Mech. of Wave Induced Forces on Cylinders, Bristol Univ., England, 510-520.
- [20] Fischer, F.J., W.T. Jones and R. King (1979), "Current-Induced Oscillations of Cognac Piles During Installation-Prediction and Measurements." *Proc. Symp. Practical Experiences with Flow-Induced Vibrations*, V.1, 216-228.
- [21] Fleischmann, S.T. and D.W. Sallet (1981), "Vortex Shedding from Cylinders and the Resulting Unsteady Forces and Flow Phenomenon." *Shock Vibration Dig.*, V.13, No.11, 9-22.
- [22] Graham, J.M.R. (1987), "The Forces on Sharp-edged Cylinders in Oscillatory Flow at Low Keulegan-Carpenter Number" *J. of Fluid Mech.*, V.97, 331-338.
- [23] Graham, J.M.R. (1987), "Transverse Forces on Cylinders in Random Waves." Intern. Conf. on Flow Induced Vibrations, Bowness-on-Windermere, England, Paper No.D7, 191-201.
- [24] Griffin, O.M. (1984), "Current-Induced Loads on Marine Structures due to Vortex Shedding." *Proc. of the Ocean Structural Dynamics*, Corvillas, OR., 457-471.
- [25] Griffin, O.M. and G.H. Koopmann (1977), "The Vortex-Excited Lift and Reaction Forces on Resonantly Vibrating Cylinders." *J. of Sound and Vibration*, V.54, 435-448.

- [26] Hansen, N.E.O., V. Jacobsen and H. Lundgren (1979), "Hydrodynamic Forces on Composite Risers and Individual Cylinders." 11th Annual Off-shore Tech. Conf., Houston, TX, Paper No.3541, 1607-1621.
- [27] Horton, T.E., H. Golestanian and M.J. Feifarek (1992), "A Correlation of Dynamic Force Coefficients Based on Wake Volume Scaling." ASME 3rd Intern. Symp. on Flow-induced Vibration and Noise, ASME Annual Meeting, Ana Heim, CA.
- [28] Ikeda, S. and Y. Yamamoto (1981), "Lift Force in Oscillatory Flows." Rep. Dept. Found. Engineering and Construction Engineering, Saitama University, V. 10, 1-16.
- [29] Isaacson, Q., de St. Michael and D.J. Maull (1977), "Discussion Transverse Forces on Vertical Cylinders in Waves." *J. of the Waterways Harbors and Coastal Eng. Div.*, No.WW2, 295-296.
- [30] Isaacson, Q., de St. Michael and D.J. Maull (1976), "Transverse Forces on Vertical Cylinders in Waves." *J. of the Waterways Harbors and Coastal Eng. Div.*, V. 102, No.WW1, Paper No.11934, 49-60.
- [31] Isaacson, Q., de St. Michael (1974), "The Forces on Circular Cylinders in Waves." Ph.D. Dissertation, University of Cambridge, U.K.
- [32] Justesen, P. (1989), "Hydrodynamic Forces on Large Cylinders in Oscillatory Flow." *J. of Waterway, Port, Coastal and Ocean Eng.*, V.114, No.4, 497-514.
- [33] King, R. (1974), "Vortex Excited Structural Oscillations of a Circular Cylinder in Steady Currents." Offshore Tech. Conf., Paper No.1948, 143-154.
- [34] King, R. (1977), "A Review of Vortex Shedding Research and Its Application." *Ocean Engineering*, Cambridge, Pergamon Press, V.4, 141-171.
- [35] King, R., M.J. Prosser and D.J. Johns (1973), "On Vortex Excitation of Model Piles in Water." *J. of Sound and Vibration*, V.29, No.2, 169-188.
- [36] Kirk, C.L. and R.K. Jain (1977), "Response of Articulated Towers to Waves and Current." 9th Annual Offshore Tech. Conf., Houston, TX, Paper No. 2798, 545-552.
- [37] Koch, S.P., J.W. Barker and J.A. Vermersch (1991), "The Gulf of Mexico Loop Current and Deep water Drilling." *J. of Petroleum Tech.*, V. 43, 1046-1050.
- [38] Koopman, G.H. (1967), "The Vortex Wakes of Vibrating Cylinders at Low Reynolds Numbers." *J. of Fluid Mech.*, V.28, 501-512.
- [39] Kozakiewicz, A., B.M. Sumer and J. Fredsøe (1991), "Correlation Measurements Along a Vibrating Cylinder near a Wall in Oscillatory Flows." 5th Intern. Conf., Flow Induced Vibrations, Proc. of the Inst. of Mech. Engineers, Brighton, U.K., 15-20.
- [40] Laird, D.K.A. (1962), "Water Forces on Flexible Oscillating Cylinders." *J. of the Waterways and Harbors Div.*, Proc. of the ASCE, V.88, No.WW3, 125-137.



- [41] Lewis, D.B., J.B. Adams, F.E. and D. Szabo (1991), "The Loop Current Experience Ewing Bank 871." *J. of Petroleum Tech.*, V. 43, 1038-1044.
- [42] Longoria, R.G., J.J. Beaman and R.W. Miksad (1991), "An Experimental Investigation of Forces Induced on Cylinders by Random Oscillatory Flow." *J. of Offshore Mech. and Arctic Eng.*, V.113, 275-285.
- [43] Matten, R.B., N. Hogben and R.M. Ashley (1978), "A Circular Cylinder Oscillating in Still Water, in Waves and in Currents." The Symp. on Mech. of Wave Induced Forces on Cylinders, Univ. of Bristol, England, 475-489.
- [44] Maull, D.J. and D. Kaye (1988), "Oscillations of a Flexible Cylinder in Waves." *Proc. of the Intern. Conf. on Behaviour of Offshore Structures*, V.2, 535-547.
- [45] Maull, D.J. and M.G. Milliner (1987), "Sinusoidal Flow Past a Circular Cylinder." *Coastal Engineering*, V.2, 149-168.
- [46] McConnell, K.G. and Y.S. Park (1982a), "The Response and the Lift-Force Analysis of an Elastically-Mounted Cylinder in Still Water." *Proc. of the Intern Conf. on Behaviour of Offshore Structures*, V.2, 671-680.
- [47] McConnell, K.G. and Y.S. Park (1982b), "The Frequency Components of Fluid-Lift Forces Acting on a Cylinder Oscillating in Still Water." *J. of Experimental Mech.*, V.22, 216-222.
- [48] Mercier, J.A. (1973), "Large Amplitude Oscillations of a Circular Cylinder in a Low-Speed Stream." Ph.D. Dissertation, Stevens Institute of Technology, Hoboken, New Jersey.
- [49] Morison, J.R., M.R. O'Brien, J.W. Johnson and S.A. Schaaf (1950), "The Forces Exerted by Surface Waves on Piles." *Petroleum Transactions*, V.189, 149-154.
- [50] Obasaju, E.D, P.W. Bearman and J.M.R. Graham (1988), "A Study of Forces, Circulation and Vortex Patterns Around a Circular Cylinder in Oscillating Flow." *J. of Fluid Mech.*, V.196, 467-494.
- [51] Omar, A.F. and D.M. Sheppard (1991), "Loading and Response of an Articulated Tower Subjected to Winds, Currents and Waves." Report for Contract No. DACW39-90-K-0020, U.S. Army Corps of Engineers, Coastal Engineering Research Center, Vicksburg, Mississippi.
- [52] Overvik, T. (1982), "Hydroelastic Motion of Multiple Risers in a Steady Current." Ph.D. Thesis Dissertation, Div. of Port and Ocean Eng., Trondheim, Norway, 173p.
- [53] Patal, M.H. (1989) *Dynamics of Offshore Structures*, London, U.K., Butterworths, Chap. 5.
- [54] Press, W.H., B.P. Flannery, S.A. Teukolsky and W.T. Vetterling (1988) *Numerical Recipes: The Art of Scientific Computing*; Cambridge, Cambridge University Press, Chap. 9.
- [55] Ramamurthy, A.S. and C.P. Ng (1973), "Effect of Blockage on Steady Force Coefficients." *Proc. ASCE*, V. 99, EM4, 755-772.

- [56] Sarpkaya, T. (1976a), "Vortex Shedding and Resistance in Harmonic Flow about Smooth and Rough Circular Cylinders at High Reynolds Numbers." Naval Postgraduate School, Report No. NPS-59SL-76021.
- [57] Sarpkaya, T. (1976b), "Forces on Rough-Walled Circular Cylinders in Harmonic Flow." 15th Coastal Eng. Conf., 2301-2320.
- [58] Sarpkaya, T. (1978), "Fluid Forces on Oscillating Cylinders." *J. of the Waterway, Port, Coastal and Ocean Div.*, V.104, No.WW4, Paper No.13941, 275-290.
- [59] Sarpkaya, T. (1979), "Vortex-Induced Oscillations - A Selective Review." *J. of Applied Mech.*, V.46, No.2.
- [60] Sarpkaya, T. (1990a), "Wave Forces on Cylindrical Piles." *The Sea; Ocean Engineering Science*, B. LeMehaute and D.M. Hanes, Editors, A Wiley-Interscience Publication, John Wiley and Sons Inc., New York, V.9, Part A, 169-195.
- [61] Sarpkaya, T. (1990b), "On the Effect of Roughness on Cylinders." *J. of Offshore Mech. and Arctic Eng.*, V.112, 334-340.
- [62] Sarpkaya, T. and M. Isaacson (1981) *Mechanics of Wave Forces on Offshore Structures*, New York, Van Nostrand Reinhold Company, 651p.
- [63] Sarpkaya, T. and F. Rajabi (1979), "Dynamic Response of Piles to Vortex Shedding in Oscillating Flows." 11th Annual Offshore Tech. Conf., Houston, TX, Paper No.3647, 2523-2528.
- [64] Sarpkaya, T. and R.L. Schoaff (1979), "Inviscid Model of Two- Dimensional Vortex Shedding by a Circular Cylinder." *AIAA Journal*, V.17, 1193-1200.
- [65] Sawaragi, T., T. Nakamura and H. Kita (1976), "Characteristics of Lift Forces on a Circular Pile in Waves." *Coastal Engineering in Japan*, V.19, 59-71.
- [66] Sawaragi, T., T. Nakamura and H. Miki (1977), "Dynamic Behavior of a Circular Pile Due to Eddy Shedding in Waves." *Coastal Engineering in Japan*, V.20, 109-120.
- [67] Schewe, G. (1983), "On the Force Fluctuations Acting on a Circular Cylinder in Cross-flow from Subcritical up to Transcritical Reynolds Numbers." *J. Fluid Mech.*, V.133, 265-285.
- [68] Scruton, C. (1967), "Aerodynamics of Structures." Theme Paper, Proc. Int. Research Seminar, National Research Council of Canada, Ottawa.
- [69] Skomedal, N.G., T. Vada and B. Sortland (1989), "Viscous Forces on One and Two Circular Cylinders in Planar Oscillatory Flow." *Applied Ocean Research*, V.11, No.3, 114-134.
- [70] Sumer, B.M. and J. Fredsøe (1988), "Transverse Vibrations of an Elastically Mounted Cylinder Exposed to an Oscillating Flow." *J. of Offshore Mech. and Arctic Eng.*, V.110, 387-394.

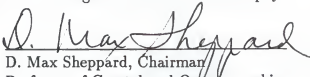
- [71] Sumer, B.M. and J. Fredsøe (1989), "Effect of Reynolds Number on Vibrations of Cylinders." *J. of Offshore Mech. and Arctic Eng.*, V.111, 131-137.
- [72] Toebes, G.H. (1969), "The Unsteady Flow and Wake Near an Oscillating Cylinder." *Trans. ASME, J. of Basic Engineering*, V.91, 493-505.
- [73] Tørum, A. and N.M. Anand (1985), "Free Span Vibrations of Submarine Pipelines in Steady Flows-Effect of Free-Stream Turbulence on Mean Drag Coefficients" *J. of Energy Resources Tech., Trans. of the ASME*, V.107, 415-420.
- [74] Tørum, A., and K. Reed (1982), "On the Span-wise Correlation of Wave Forces on Slender Structures." 14th. Annual Offshore Tech. Conf., Houston, TX, Paper No.4226, 721-729.
- [75] van der Vegt, J.J.W. and F. van Walree (1987), "Progress in the Prediction of Forces on Cylinders." *Proc. of a Workshop on Floating Structures and Offshore Operations*, Wageningen, The Netherlands, 251-266.
- [76] Verley, R.L.P. (1980), "Oscillations of Cylinders in Waves and Currents." Ph.D. Dissertation, Norwegian Institute of Technology, 415p.
- [77] West, G.S. and C.J. Apelt (1982), "The Effects of Tunnel Blockage and Aspect Ratio on the Mean Flow Past a Circular Cylinder with Reynolds Numbers between  $10^4$  and  $10^5$ ." *J. Fluid Mech.*, V.114, 361-377.
- [78] Williamson, C.H.K. (1985), "Sinusoidal Flow Relative to Circular Cylinder." *J. Fluid Mech.*, V.155, 141-174.
- [79] Wolfram, J., P. Javidan and A. Theophanatos (1989), "Vortex Shedding and Lift Forces on Heavily Roughened Cylinders of Various Aspect Ratios in Planar Oscillatory Flow." *Proc. of the Offshore Mech. and Arctic Eng. Conf.*, The Hague, 269-278.
- [80] Yamamoto, T. and J.H. Nath (1976), "High Reynolds Number Oscillating Flow by Cylinders." *Proc. 15th Coastal Eng. Conf.*, Honolulu, Hawaii, 2321-2340.

## BIOGRAPHICAL SKETCH

The author was born on June 2, 1959, and raised in Alexandria, Egypt, a popular mecca for swimmers and sunbathers on the Mediterranean sea. He graduated from high school in 1977 and entered the University of Alexandria. In July 1982, he graduated with a B.S. in Naval Architecture and Marine Engineering with grade "Distinction with the Degree of Honor." He started his military service in October 1982 in the Egyptian Navy and was appointed instructor in the Department of Naval Architecture and Marine Engineering at the University of Alexandria.

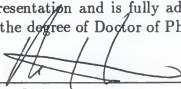
In January 1984, he finished his military service and started his career as an instructor. At the same time he started work on his Master degree on "Computer-Aided Structural Design of Bulk-Carriers." In February 1986 he was granted his M.Sc. in Naval Architecture degree and promoted to assistant lecturer in the department. In January 1987, the author was granted a Memorial University Fellowship to pursue his Ph.D. in the Ocean Engineering Department of Memorial University of Newfoundland, Canada. Unsatisfied with his topic on ice impact loads on ships and longing to learn more about offshore structures, he decided to transfer to the United States. In August 1988, he was admitted to the Graduate School at the University of Florida in Gainesville, Florida. He also received an appointment as a graduate research assistant in the Coastal and Oceanographic Engineering Department. Since August 1988, he has been working on his Ph.D. degree in the offshore structures program in this department.

I certify that I have read this study and that in my opinion it conforms to acceptable standards of scholarly presentation and is fully adequate, in scope and quality, as a dissertation for the degree of Doctor of Philosophy.



D. Max Sheppard, Chairman  
Professor of Coastal and Oceanographic  
Engineering

I certify that I have read this study and that in my opinion it conforms to acceptable standards of scholarly presentation and is fully adequate, in scope and quality, as a dissertation for the degree of Doctor of Philosophy.



Marc I. Hoit  
Associate Professor of Civil Engineering

I certify that I have read this study and that in my opinion it conforms to acceptable standards of scholarly presentation and is fully adequate, in scope and quality, as a dissertation for the degree of Doctor of Philosophy.



Hsiang Wang  
Professor of Coastal and Oceanographic  
Engineering

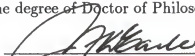
I certify that I have read this study and that in my opinion it conforms to acceptable standards of scholarly presentation and is fully adequate, in scope and quality, as a dissertation for the degree of Doctor of Philosophy.



David C. Zimmerman  
Assistant Professor of Aerospace  
Engineering, Mechanics, and  
Engineering Science

This dissertation was submitted to the Graduate Faculty of the College of Engineering and to the Graduate School and was accepted as partial fulfillment of the requirements for the degree of Doctor of Philosophy.

August 1992

*for*   
\_\_\_\_\_  
Winfred M. Phillips

Dean, College of Engineering

\_\_\_\_\_  
Madelyn M. Lockhart  
Dean, Graduate School